PhD Thesis

Violation of the fundamental symmetries and atomic structure of superheavy elements

Bryce G. C. Lackenby

July 23, 2019

Contents

Abstract

We introduce the weak quadrupole moment of nuclei, related to the quadrupole distribution of the weak charge in the nucleus. The weak quadrupole moment produces a tensor weak interaction between the nucleus and electrons and can be observed in atomic and molecular experiments measuring parity nonconservation. The dominating contribution to the weak quadrupole is given by the quadrupole moment of the neutr on distribution, therefore, corresponding experiments should allow one to measure the neutron quadrupoles. Using the deformed oscillator model and the Schmidt model we calculate the quadrupole distributions of neutrons, Q_n, the weak quadrupole moments, $Q_W^{(2)}$, and the Lorentz Invariance violating energy shifts in ^{9}Be, ^{21}Ne , ^{27}Al, ^{131}Xe, ^{133}Cs, ^{151}Eu, ^{153}Eu, ^{163}Dy, ^{167}Er, ^{173}Yb, ^{177}Hf, ^{179}Hf, ^{181}Ta, ^{201}Hg and ^{229}Th.

Atomic spectra and other properties of superheavy element dubnium (Db, Z=105) are calculated using recently developed method combining configuration interaction with perturbation theory (the CIPT method, Dzuba et al, Phys. Rev. A, **95**, 012503 (2017)). These include energy levels for low-lying states of Db and Db II, electric dipole transition amplitudes from the ground state of Db, isotope shift for these transitions and ionisation potential of Db. Similar calculations for Ta, which is lighter analog of Db, are performed to control the accuracy of the calculations.

Acknowledgements

Accepted papers

[1] B. G. C. Lackenby, V. A. Dzuba, and V. V. Flambaum. *Phys. Rev. A* 98, 022518 (2018)

[2] B. G. C. Lackenby and V. V. Flambaum. *Journal of Physics G* 45, 075105 (2018)

[3] B. G. C. Lackenby, V. A. Dzuba, and V. V. Flambaum. *Phys. Rev. A* 98, 042512 (2018)

[4] B. G. C. Lackenby and V. V. Flambaum. *Phys. Rev. D* 98, 115019 (2018)

[5] B. G. C. Lackenby, V. A. Dzuba, and V. V. Flambaum. *Phys. Rev. A* 99, 042509 (2019)

Part I

Violation of fundamental symmetries in nuclei

Chapter One

Introduction

Since its inception in the latter half of the of 20th century, the Standard Model (SM) has proven a robust phenomenological theory and remains the most holistic and accurate description of the interactions (with the exception of the gravitational force) of known fundamental particles and forces in nature. However despite the success of the SM there are physical phenomena which cannot be described without the SM being revised or extended. Similar to how classical physics is a large spatial approximation to quantum theory, it is suspected that the standard model is a low energy approximation to a more fundamental theory of the universe. Therefore, for the past several decades there has been a determined, concerted effort to detect, measure, and explain phenomena which lie outside the current standard model of physics, known as "beyond the standard model" (BSM) physics. On this frontier of modern physics, a possible avenue to study BSM physics is through the violation of fundamental symmetries of nature and how they manifest in physical systems. Many BSM theories have been proposed such as supersymmetric [16, 17, 10, 18], double Higgs [19] and Left-Right symmetric models [20]. Some of the observed phenomena which initiated this search for BSM are the existence of dark matter and energy, the non unified gravitational forces and the apparent matter and anti-matter assymetry in the universe. It is the last of these which is most appropriate to this thesis.

The observed matter-antimatter asymmetry in the universe is an important open question in modern physics. Three necessary conditions were postulated by Sakarhov[6] including the requirement that combined charge and parity (CP) symmetry is violated. While the current standard model (SM) includes a CP-violating mechanism through a CP- violating phase in the CKM matrix [7] this alone is insufficient to account for the observed matter anti-matter asymmetry by several orders of magnitude (see e.g. Refs. [6, 8, 9, 10, 11, 12]). Therefore,

other sources and mechanisms of CP- violation beyond the current SM must exist and investigating these will give insight into new physics.

The apparent matter anti-matter asymmetry of the universe remains an open question in modern physics and one of the primary reasons physics beyond the standard model exists and manifests in prominent ways. It is apparent that in our universe there is an unequal amount of matter and anti-matter. If an identical amount of matter and anti-matter was created at the big bang, they would have annhiliated each other resulting in only energy In 1967 A. D. Sakharov proposed three necessary conditions to account for the matter anti-matter in the universe [6]:

1. Baryon number B violation.

2. C-symmetry and CP-symmetry violation.

3. Interactions out of thermal equilibrium.

Since this work each of these conditions have been studied extensively. The second condition, violation of $CP-$ symmetries has been observed in the standard model in the decay of neutral kaons. The three discrete symmetries parity $(P-)$, time-reversal $(T-)$ and charge-congugation $(C-)$ are fundamental symmetries of nature. One avenue of interest is the detection of the violation of fundamental symmetries is an avenue which is suspected to overthrow the model by suggesting a deeper underlying theory. There are a number of discrete symmetries which form the basis of our current interpretation of the universe. They are time-reversal T parity and charge conjugation (get the paragraph from Honours thesis).
Bertolami (CPT violation and baryogenesis) Of these discrete symmetries only parity has been determined to be violated. This is a prediction of the standard model weak interaction and therefore the bubble has yet to burst on the standard model. In this thesis we will look at some processes which violate these symmetries.

There are two distinct approaches to measure BSM phenomena. As the SM is suspected to be a low energy approximation to a greater theory, the naive approach to detect BSM physics is through high energy experiments with direct detection of new phenomena. However, this presents a problem. The energy scale where the SM breaks down and quantum gravitational effects become appreciable is at the Plank scale $M_P \approx 2.4 \times 10^{18}$ GeV. With current high energy experimental probes only reaching into the low TeV (current experimental limits at the Large Hadron Collider reach 13 TeV), direct measurements at this scale

are currently impossible. To increase the accessible energy scale, great scientific and technological leaps need to be achieved along with great expense to build facilities. On a similar note, large scale astrophysical experiments which study the early universe such as BICEP3[13] and PLANK[14] telescopes present similar technological, scientific and economical problems and therefore other avenues of detection need to be explored. Though BSM physics are inherently high energy phenomena, it is suspected that signatures of these effects can be observed heavily suppressed in low energy experiments. Low energy, electroweak experiments occur on a mass scale $m_{ew} \approx 246$ GeV and it is suspected that BSM effects are expected to be a ratio of the electroweak and Plank scale $m_{ew}/M_P \approx \times 10^{-16}$ [15].

Atoms provide an optimal experimental and theoretical space to test the SM as they are governed by all the interactions present in the SM.

Part I of this thesis progresses as follows, in Chapter 2 I give an overview on the violation of fundamental symmetries and how they manifest in atomic and molecular systems.

In Chapter 3 I give a discussion on deformed nuclei including an overview of the Nilsson model and the quadrupole deformation of nuclei.

In Chapter 4 I present my results on the weak quadrupole moment and Lorentz violation in deformed nuclei of experimental interest.

In Chapter 5 I present my results on the magnetic quadrupole moment in deformed nuclei of experimental interest and the resultant energy shifts in molecular species.

In Chapter 6 I give a brief discussion and conclusion on the results presented in Part I.

Chapter Two

Fundamental symmetries and their violation

The study of the fundamental discrete symmetries, parity, time-reversal and charge conjugation, as well as the isotropy of space (Lorentz symmetry) are the foundation of modern physics including the Standard Model (SM) and theory of general relativity. Therefore, the search for violation of these symmetries has been at the forefront of the search for new physics for the last century. In this chapter I give a brief historical review of these symmetries and the searches for their violation in nuclear, atomic and molecular systems.

2.1   Violation of discrete symmetries

There are three key discrete symmetry transformations in nature; parity $(P-)$, charge conjugation $(C-)$ and time reversal $(T-)$. A parity transform is the inversion of all spatial coordinates of a system $(\mathbf{r} \overset{P}{\mapsto} -\mathbf{r})$ which is corresponds to the mirror reflection along with a π rotation in the plane of the mirror. A time-reversal transform reverses the instantaneous velocity of all the particles $(t \overset{T}{\mapsto} -t)$ and charge conjugation transforms all particles to their respective antiparticle $(m \overset{C}{\mapsto} \bar{m})$. The violation of any of these symmetries has profound consequences in both classical and quantum physics. Up until the middle of the 20th it was unknown whether these symmetries were violated and the strong and electromagnetic forces were well tested for violation of fundamental symmetries. For example, the conservation of parity in atomic electric dipole transitions (Laporte's rule) was well tested and parity was expected to be a good symmetry. This was until 1956 when T. D. Lee and C. N. Yang predicted the violation of $P-$ in the weak interaction[21]. This was experimentally confirmed a year

later by Wu *et al.* in 1957 [22] where it was found that the both $P-$ and $C-$ were violated in the beta decay of ^{60}Co. While this was a ground breaking discovery and resulted in a Nobel prize for T. D. Lee and C. N. Yang for the orginal prediction, the existence of parity violation was not forbidden in the electro-weak sector of the SM and therefore not confirmation of BSM physics. Since this discovery the search for violation of the discrete symmetries in other mechanisms has rapidly expanded and now spans many disciplines of physics including high energy particle physics, atomic physics and nuclear physics.

As it was found both $P-$ and $C-$ were violated it was proposed that the combined $CP-$ symmetry was the true fundamental, invariant symmetry. This suspicion did not last long however, as $CP-$ violation was experimentally detected in 1964 Christenson *et al.* [23] where it was found that $CP-$ symmetry was indirectly violated in the decay of kaons for which V. Fitch and J. Cronin were awarded the Nobel Prize in physics. Along with Lorentz invariance (see Section 2.2) the invariance of combined CPT symmetry is fundamental. The CPT theorem states that any Lorentz invariant Lagrangian is necessarily invariant under CPT transformations (see Refs. [24, 25, 26] for more details). Therefore the violation of combined $CP-$ symmetry directly implies violatio of $T-$ symmetry. Soon after the discovery of CP violation by Cronin *et al.* violation of combined $CP-$ symmetry was found to exist in the current SM in the strong sector in the complex phase of the Cabbibo-Kobayashi-Maskawa (CKM) matrix [27, 7]. This source of $CP-$ violation in the SM explained results of V. Fitch and J. Cronin and therefore the discovery, although significant, was not due to BSM physics. Also, the mangitude of $CP-$ violation measured by V. Fitch and J. Cronin does not account for the magnitude of matter anti-matter asymmetry present in the universe. Therefore, this necessitates the existence of other sources of $CP-$ violation not accounted for and therefore physics beyond the standard model. More recently direct $CP-$ violation in the Kaon systems [28, 29] along with both direct and indirect $CP-$ violation in the B meson sector [30, 31, 32] have been measured. These recent measurements in both kaons and B mesons agree with the CKM model and do not suggest BSM physics. As these particle decay experiments are not the focus of this thesis, we will not consider them further. For an in-depth review of $CP-$ violation in this field please refer the references [].

Along with these high energy particle decay processes, the existence of some permanent electromagnetic moments also violate fundamental symmetries. The possibility of permanent electromagnetic moments which violate discrete symmetries was was first proposed in 1950 by Purcell and Ramsey [33]. The exis-

tence of a permanent electric dipole moment (EDM) violates both $T-$ and $P-$ symmetries (and therefore $CP-$ symmetry)[34]. This can be seen through the following simple argument. This electric dipole moment, $\mathbf{d}$ is by definition given by,

$$\mathbf{d} = e \int \mathbf{r}\rho(\mathbf{r})d^3r \tag{2.1}$$

where $\rho(\mathbf{r})$ is the density of the particle. However, the electric dipole moment of a particle must be parallel (or anti-parallel) to the angular momentum vector as it is the only vector which characterizes the direction of the system. Therefore it necessarily must be equal to,

$$\mathbf{d} = d_z \frac{\mathbf{I}}{I}. \tag{2.2}$$

Where $I = I_z$ is the particle's angular momentum. This presents a contradiction, under a $P-$ transformation, equations (2.1) and (2.2) are $P-$odd and $P-$even respectively and therefore parity symmetry is violated by the existence of a permanent EDM. A similar argument can be made to demonstrate the violation of $T-$ symmetry. Both of these are demonstrated in Figure 2.1. The $CP-$ violating phase in the CKM matrix of the SM does facilitate a permanent EDM of the electron, neutron. The CKM predicts an electron EDM[?] and neutron (proton) EDM [165] as,

$$d_e^{SM} \approx 10^{-38} \ e \cdot \text{cm} \tag{2.3}$$

$$|d_{n,p}^{SM}| \approx (1-6) \times 10^{-32} \ e \cdot \text{cm}. \tag{2.4}$$

Other than the EDM, other orders of permanent electromagnetic moments violate $T-$ symmetry, for the electrical moments specifically, the next violating moment is the electric octupole moment (EOM). In terms of magnetic moments, the lowest order $T-, P-$ violating magnetic moment is the magnetic quadrupole moment (MQM) which has the form of a second order tensor. To demonstrate the $T-, P-$ violation of the MQM a similar argument to the EDM can be made when considering the two forms of the MQM tensor [69],

$$M_{kn} = - \int \left(r_k \epsilon_{npq} + r_n \epsilon_{kpq} \right) j_p r_q d^3r \tag{2.5}$$

$$M_{kn} = \frac{3}{2} \frac{M_{zz}}{I(2I-1)} \left[I_k I_n + I_n I_k - \frac{2}{3} I(I+1)\delta_{mk} \right]. \tag{2.6}$$

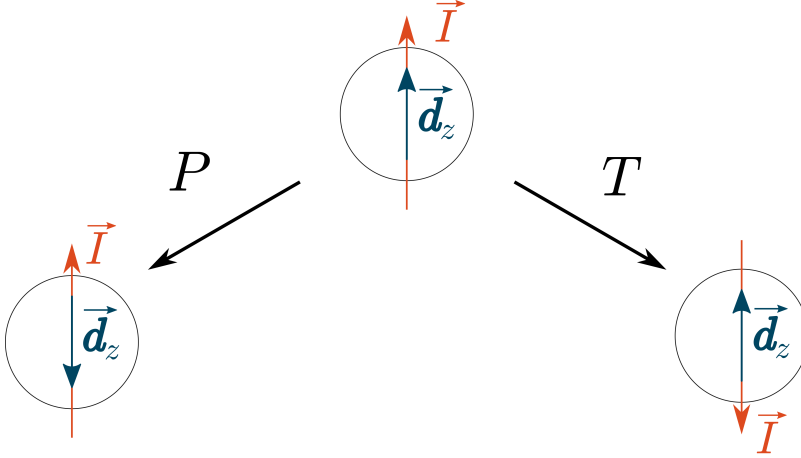Here $M_z z$ is the maximum value of the MQM on the z axis, δ_{ij} and ϵ_{ijk} and

Figure 2.1: This diagram show the P and T transforms of a particle with angular momentum I and a finite EDM **d**. The spatial EDM defined in is P-odd and T-even. However as the EDM must be in the direction of the angular momentum of the particle which is P-even and T-odd there is a contradiction and the EDM violates P and T.

the standard symmetric delta function and anti-symmetric tensor respectively. Equation 2.5 is both $T-$ and $P-$odd whereas equation 5.1 is $T-$ and $P-$even, and therefore a permanent MQM violates both $T-$ and $P-$ symmetries. The MQM has more restrictive properties than the EDM as only systems with $I > 1/2$ can have an MQM.

Along with the proposal of a permanent EDM, Ramsey and Purcell along with Smith performed the first experiment to try and measure the EDM of a neutron [35] where they set the first constraint on the neutron EDM. $d_n < 5 \times 10^{-20}$ cm.

2.2 Lorentz symmetry violation

Tests of Lorentz violation also span both high-energy, cosmological scales down to low energy precision tests. γ ray bursts are a potential test of quantum gravity [36]. A superluminal charged particle will rapidly radiate photons until it no longer exceeds the speed of light [37]. A review on potential high energy Lorentz violating tests can be found in Ref. [38].

Like the discrete symmetries, Lorentz symmetry is one of the most fundamental symmetries in nature. It forms the basis of modern physics as the cornerstone to special relativity. Local Lorentz invariance (LLI) states that there is no preferred reference frame of the universe and the laws of physics are unchanged when the orientation of the system (rotation) or speed of the system (boosts) is

changed. Due to its importance, considerable effort has been made over the last century to test and quantify its validity through experiments [39, 40, 41, 42, 43].

In the current SM Lorentz invariance, along with combined CPT, is always conserved. However, there are many proposals for new physics BSM such as GUT and String theories that require LLI to be violated [44, 45, 46, 47, 15, 48, 49]. Like the discrete symmetries above, LLI is suspected to be a low-energy effective property which is spontaneously broken at higher energies due to an underlying theory. Unlike violation of the discrete symmetries however, there are no sources of LLIV in the SM and any measurement of some anisotropy will be the result of some unknown greater underlying theory. Therefore an extension to the SM in Refs. [50, 51, 52, 53] has been proposed which contains LLIV terms in the SM Lagrangian while preserving other desirable properties of the SM such as renormalizability and gauge invariance. This extension to the SM provides a framework to represent and quantify particular LLIV mechanisms in experiments.

The possiblility of these new physics has led to a renewed concerted effort in detecting LLIV using modern experimental methods using more sophisticated techniques. These include resonance cavity experiments [54, 55, 56], Doppler shift experiments [57, 58] and clock comparison experiments [59, 60, 61, 62]. These experiments rely on measuring slight variations in results when the orientation or speed of the system is changed and therefore require extremely precise measurements. Currently, these experiments have only resulted in null measurements, however they have constrained the LLIV parameters in the SM extension extensively. A yearly review on the current status of LLIV can be found in [?] which provides an exhaustive list of the constraints on LLIV parameters in the SM extension.

The SME proposed by D. Colladay and V. A. Kostelecký is an exhaustive model containing all the Lorentz and CPT violating terms. In this thesis we only consider the CPT-even, Lorentz violating term associated with the momentum tensor. The LLIV Lagrangian for a spin-$\frac{1}{2}$ term associated with this parameter is [52],

$$\mathcal{L} = \frac{1}{2}i\bar{\psi}c_{\mu\nu}\gamma^{\mu}\overleftrightarrow{\partial^{\nu}}\psi. \tag{2.7}$$

where $c_{\mu\nu}$ is the traceless parameter which scales the momentum tensor. Where γ^{ν} are the standard Dirac matrices. This corresponds to an energy shift due to

LLIV as,

$$\delta H = -mc_{00} + m\left(c_{0j} + c_{j0}\right)\frac{p_j}{m} + m\left(-c_{jk} - \frac{1}{2}c_{00}\delta_{jk}\right)\frac{p_i p_k}{m^2}. \qquad (2.8)$$

In this thesis we only consider the last term which relates to the momentum tensor $p_i p_j$. We discuss the [potential measurement of this term in Section 2.3

2.3 Violation in nuclear, atomic and molecular systems

As mentioned previously, while violation of the LLI and $CP-$ symmetries are spontaneously broken at extremely high energies, signatures of these violations may manifest at low energies. The realm of atomic and nuclear physics is a perfect domain to search for these signatures as they offer high sensitivity at relatively low cost. The concept of using atomic interactions to detect LLIV has long been considered [63, 64, 59, 65, 66]

Atoms, molecules and nuclei provide an optimal space to test the Standard Model as all SM interactions are found in atomic theory and can be probed.

CP- violating permanent electrodynamic moments are expected to be observed in composite particles and systems such as atoms, nuclei and baryons and interpreted as parameters of CP- violating interactions in the lepton and quark-gluon sectors. In this paper we focus on the magnetic quadrupole moment (MQM) of the nucleus in particular, which is the lowest order magnetic moment that is forbidden in quantum systems by the time reversal invariance (T) and parity (P). For an in-depth review on symmetry violating electromagnetic moments including the MQM see Ref. [67, 68, 69, 70, 25, 10]. The MQM of composite systems such as the deuteron [71] have previously been investigated. The search for MQM in comparison with the electrostatic T, P-violating moments (EDM, Schiff and octupole moments) may have the following advantages:

The nuclear EDM in neutral atoms and molecules are completely screened [72]. The Schiff and octupole moments have an additional second power of a very small nuclear radius. The magnetic interaction is not screened. The MQM contribution to atomic EDM typically is an order of magnitude larger than the contribution of the Schiff moment and several orders of magnitude larger than the octupole contribution [69, 73].

In quadrupole deformed nuclei MQM is enhanced by an order of magnitude [74], therefore, the MQM contribution to atomic EDM may be two orders of magnitude larger than the Schiff moment contribution.

In the expression for the Schiff moment there is a partial cancellation between the first term and the second (screening) term. There is also a screening correction to the octupole moment [75, 69, 76].

In the Hg and Xe atoms where the most accurate measurements of atomic EDM have been performed, the valence nucleon is a neutron. Therefore, the electrostatic moments (EDM, Schiff and octupole) moments do not appear directly, they exist due to the nuclear polarization effects [75]. Due to the screening effect and the indirect polarization origin of the Schiff moment the nuclear calculations are rather unstable. In the case of the MQM moment both valence protons and neutrons contribute directly, and the result is expected to be more accurate[77].

A promising method of measuring CP- violating moments is in diatomic molecular experiments where the effective electric field is significantly larger than those directly accessible in laboratory experiments. There is a considerable body of work for calculating the effective electric field in diatomic molecular systems which may be experimentally viable. Both theoretical and experimental progress has been made in measuring the $T, P-$ odd effects in YbF[78, 79, 80, 81, 82, 83, 84, 85], HfF$^+$ [86, 87, 88, 89, 90, 91, 92, 93, 94], ThO [95, 96, 97, 98, 99, 100, 101, 102], ThF$^+$[87, 103, 104], TaN [105, 106] and TaO$^+$ [107] particularly in relation to the nuclear Schiff moment and electron EDM. In section 5.2 we present the molecular energy shift due to the nuclear MQM for these molecules.

The PNC effects appear due to mixing of opposite parity states in atoms and molecules by the weak interaction between the nucleus and electrons. The field of PNC in atoms and molecules has been thoroughly reviewed in Refs. [68, 108, 109]. It was noted in Ref. [110] that the nuclear quadrupole moment induces a tensor PNC weak interaction between the nucleus and electrons (see also [68, 111]). In Ref. [112] it was argued that these tensor effects of the weak quadrupole moments are strongly enhanced for deformed nuclei and may get a significant additional enhancement due to mixing of close atomic and molecular levels of opposite parity with a difference of the electron angular momenta $|J_1 - J_2| \leq 2$. These selection rules are similar to that for the effects of the time reversal (T) and parity (P) violating nuclear magnetic quadrupole moment (MQM). Therefore, nuclei, molecules and molecular levels suggested for the MQM search in Ref. [77], for example, $|\Omega| = 1$ doublets in the molecules ^{177}HfF+, ^{229}ThO, ^{181}TaN will also have enhanced effects of the weak quadrupole (see section 4.5). Following our proposal, there has been recent experimental interest in using the weak quadrupole moment to study PNC effects in HfF$^+$ molecules (used to measure electron electric dipole moment [94]) and parity violation in ^{173}Yb [113] and ^{163}Dy [114] atoms.

However, the best current laboratory limits are from clock comparison ex-

periments [59, 60, 61, 62] in particular the tensor LLIV parameters c_{ij} for the neutron in [137] using a ^{21}Ne clock and for the proton in [138] using ^{133}Cs clocks which was further constrained by 4 orders of magnitude in [112].

The best laboratory limits on the Michelson-Morley type LLIV tensor in the photon sector has been obtained in Ref. [139] using the ^{21}Ne clock data from [137]. The limits on the LLIV parameters obtained using astrophysical measurements and laboratory experiments can be found in [52, 53].

Violation of LLIV in nuclear systems using the tensor interaction does not require study of nuclear transitions like other LLIV parameters as the angular momentum projections are different. The $C_0^{(2)} = c_{xx} + c_{yy} - 2c_{zz}$ is the LLIV tensor interaction in the laboratory frame where the quantization axis (same as the deformation axis deformed nuclei, see next chapter) lies along the z axis.

Chapter Three

Properties of deformed nuclei

In this chapter I give a brief overview of the Nilsson model for deformed nuclei and the quadrupole properties of nuclei. The independent particle model will only describe how a single nucleon will behave in the mean field. In the case of an atom this is a relatively simple and stable approach. This is because in an atom, to a first approximation, the electrons experience a potential from the much larger point like nucleus. It is only in lower approximations that you take into account the inter electron potential by using methods such as Hartree Fock. However in the nucleus there is no centre source of potential, it all comes from the inter-nucleon interactions which is not completely understood. Therefore any mean field potential ascribed to the nucleus is going to be inherently unstable, especially when considering larger nuclei. This results in a anisotropy of the nucleus which has interesting properties when trying to understand nuclear physics.

3.1   The Nilsson Model

While collective effects of the nucleus have been considered for a significantly long time with the liquid drop model, they were not considered in the context of the microscopic prospect of the nucleus. The isometric shell model is an independent single particle model where the nucleons are modeled in a mean field approximated by the interaction of the other nucleons which was very successful in predicting the closed shells in spherical nuclei[121, 122]. While the spherical shell model was successful in predicting closed shell of spherical nuclei, it had limitations when considering highly deformed nuclei. Collective

(a) Prolate deformation of a nucleus. Here the z axis is the symmetry axis.

(b) Oblate deformation of a nucleus. Here the z axis is the symmetry axis.
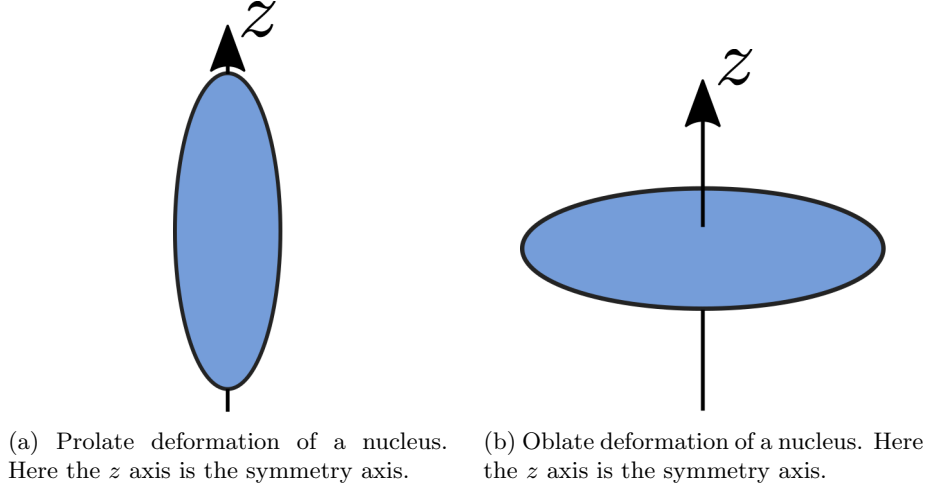
Figure 3.1

properties of the nucleus include large quadrupole moments and nuclear fission. Non-spherical nuclei were first explored in depth by Rainwater in 1950 [123]. A single-particle model which accounts for the asymmetry of the nucleus was developed by S. G. Nilsson in 1955 [124]. This model, known as the Nilsson model, uses an anisiotropic harmonic oscillator potential to describe the nuclear potential the nucleons move in. The complete Hamiltonian of the Nilsson model is given by [124, 125],

$$H = \frac{\mathbf{p}^2}{2m} + \frac{1}{2}m\left[\omega_\perp\left(\mathbf{x}^2 + \mathbf{y}^2\right) + \omega_z\mathbf{z}^2\right] + C\mathbf{l}\cdot\mathbf{s} + D\left(\mathbf{l}^2 - \left\langle I^2\right\rangle\right) \qquad (3.1)$$

which has the form of an asymmetric three dimensional harmonic oscillator model where we have chosen the $z-$axis as the axis of deformation. Here m is the nucleon mass, ω_z and $\omega_\perp = \omega_x = \omega_y$ (as we are considering quadrupole deformations only) are the nucleon oscillation frequencies along the $z-$axis and the perpendicular plane respectively. Both the spin-orbit term $(\mathbf{l}\cdot\mathbf{s})$ and the $\mathbf{l}^2 - \left\langle I^2\right\rangle$ terms were included to reproduce the magic numbers in the spherical limit. To relate this Hamiltonian to the the collective deformation of the nucleus, δ, the angular frequencies and deformation parameter are related by,

$$\omega_{\perp^2} = \omega_0^2\left(1 + \frac{2}{3}\delta\right)$$

$$\omega_z^2 = \omega_0^2\left(1 - \frac{4}{3}\delta\right)$$

In the spherical shell model the orbit with angular momentum I has degener-
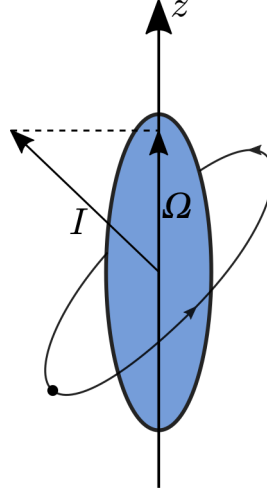
Figure 3.2: Projection of angular momentum of a prolate deformed nucleus onto the symmetry axis in the intrinsic frame. Here I is the angular momentum of the nucleon and Ω is its projection on the axis of deformation.

acy $2I+1$ nucleons. This degeneracy is broken in the Nilsson model for deformed nuclei where the projection of the angular momentum onto the symmetry axis, Ω, is the good quantum number (see Figure 3.2). Each of these Ω states are doubly degenerate. The consequences of a deformed nucleus on the quantum states of the constituent nucleons can be deduced from two simple physical arguments. Consider the non-rotating, intrinsic (body) frame of the nucleus. Where Ω is the projection of the nucleons angular momentum I on the deformation axis. By definition the projection of total angular momentum on the symmetry axis Ω is the sum of the projection of the orbital angular momentum, Λ and the projection of the spin angular moment$\Sigma = \pm 1/2$. $\Omega = \pm\frac{1}{2}, \pm\frac{3}{2}, \pm\frac{5}{2}, ..., \pm\frac{I}{2}$

The deformation of the nuclear field implies important modifications of the nucleonic motion. Each orbit may be occupied twice, corresponding to the two possible signs of Ω. The absence of degeneracies implies a very simply coupling scheme for the particle motion. Thus, in an odd-A nucleus the ground-state spin is equal to the value of Ω for the orbit occupied by the last nucleon except for $\Omega = 1/2$ [124]. In the regions of closed major shells (N) the equilibrium shape of the nucleus is spherical. The only oblate candidates are those where the protons or neutrons are near the end of a major shell. Therefore the vast majority of nuclei are prolate deformed, however the Nilsson model is also applicable for oblate nuclei.

To classify each constituent nucleon in the deformed nucleus we use the notation proposed by Nilsson[124, 126]. Each nucleon can be characterised by the set of quantum numbers $[Nn_z\Lambda \pm \Omega]$ [126] where $N = n_z + n_x + n_y$

and each n_i $(i = x, y, z)$ is the principal quantum number in the direction of i, Λ and Ω are the nucleon's orbital and total angular momentum projection on the deformation axis respectivly. Each energy level is doubly degenerate for $\pm\Omega$. The average oscillator frequency is given by $\hbar\bar{\omega} = \hbar/3 \left(2\omega_\perp + \omega_z\right) \approx 45A^{-1/3} - 25A^{-2/3}$ MeV[127].

3.2 Second order tensor properties of nuclei

Second order tensor properties in deformed nuclei exhibit a collective enhancement compared to vector properties. Consider the magnetic dipole moment which is proportional to the projection of the total angular momentum Ω to the nuclear axis. In an even-even nucleus all the nucleons are paired and therefore the magnetic dipole moment of the $+\Omega$ state cancels with the $-\Omega$ state resulting in no net magnetic dipole moment of the nucleus. For an odd A nucleus the magnetic dipole moment of the entire nucleus is simply the dipole moment of the odd nucleon. This is the well known Schmidt model of the nucleus. The cases for second order tensor properties of the nucleus are different. For nucleons in the $+\Omega$ and the $-\Omega$ states tensor properties are additive. Therefore there is a collective effect and many nucleons contribute to the tensor properties of the nucleus.

In the Nilsson model we consider the nucleus in the intrinsic frame which rotates with the nucleus. However the nucleus itself rotates with respect to the fixed laboratory frame [126]. Due to this rotation the tensor properties transform between the intrinsic and laboratory frame. The relationship between these two frames is [126]

$$A^{Lab} = \frac{I\left(2I - 1\right)}{\left(I + 1\right)\left(2I + 3\right)} A^{Intrinsic}, \tag{3.2}$$

where $I = I_z = |\Omega|$ is the projection of total nuclear angular momentum (nuclear spin) on the symmetry axis. This expression shows that only in nuclei with spin $I > 1/2$ can we detect these second order tensor properties.

To illustrate why the MQM tensor should be enhanced in quadrupole deformed nuclei let us compare it with the EDM vector property of nuclei. The direction of the EDM of a nucleon is characterised by its angular momentum projection on the deformed nucleus axis Ω. In the case of the vector properties such as EDM and magnetic moment the contributions of Ω and $-\Omega$ cancel each other and there is no enhancement in the quadrupole deformed nuclei. For the second rank tensors such as MQM and nuclear electric quadrupole moment the contributions of Ω and $-\Omega$ double the effect. There are many nucleons in the open shells of deformed nuclei and this leads to a collective enhancement of

second rank tensor properties.

The existence of non-spherical nuclei has been suspected since the 1930s where anomalous behaviour was observed in the hyperfine structure in isotopes of Eu ($Z = 63$) and Lu ($Z = 71$) by H. Schuler and Th. Schmidt [115, 116]. Soon after this discovery, H. B. G. Casimir published an explanation of these results and posited the anomaly could be explained by the existence of an permanent electric quadrupole moment of the nucleus which interacts with the atomic electrons [117, 118]. The origin of this nuclear quadrupole moment was orginally ascribed to the existence of an unpaired valence proton with nuclear spin I_t which induces and electric quadrupole moment $Q_{p,\mathrm{val}}$ of the nucleus by the equation [119],

$$Q_{p,\mathrm{val}} = -\frac{I_t - 1/2}{I_t + 1} 0.009 A^{2/3} \text{ barn.} \tag{3.3}$$

This single particle description is incomplete for several reasons. Firstly, it does not account for the quadrupole moments of nuclei with unpaired neutrons which also have significant quadrupole moments, for example $^{163}_{66}$Dy has an unpaired neutron with an experimental quadrupole moment $Q_p = +2.318(2)$ barn [120]. Secondly, the magnitude of a quadrupole moment from a single proton is significantly less than those observed in experiment. For example consider $^{181}_{73}$Ta, which has total nuclear spin $I_t = 7/2^+$, using eqn (**??**) results in a quadrupole moment of $Q_{p,\mathrm{val}} = -0.192$ barn. This is significant less (along with opposite sign) than the experimental $Q_p = +3.17(2)$ barn. Therefore the quadrupole moment of a nucleus must be a collective effect of the nucleus involving a large amount of the nuclear matter and cannot be accounted for by a single nucleon.

Measuring the NQMN, Q_n, is a very difficult task as neutrons are electrically neutral particles unlike the electric quadrupole moment of the nucleus which was first observed and measured nearly a century ago by H. Schuler and Th. Schmidt [115, 116, 117] by studying the hyperfine structure of rare earth elements. The NQMN is an important property which will give insight not only into the structure of atomic nuclei but also other dense collections of neutrons such as neutron stars [129, 130, 131, 132] and also the theory of atomic parity nonconservation. For the last two decades there has been increasing interest in understanding the distribution of neutrons compared to protons in atomic nuclei known as the neutron skin. This focus has largely been on the spherical distribution of neutrons (measurement of the root mean square radius of neutrons) and there has been a large amount of experimental effort in measuring the spherical distribution [133, 134, 135, 136].

Rewriting equations (4.13), (4.6) and, the relation between the longitudinal and perpendicular frequencies in dimentionless quantities $\eta = \bar{\omega}/\omega_z$ and $\xi =$

$\bar{\omega}/\omega_\perp$ we have the equations,

$$3 = \frac{1}{\eta} + \frac{2}{\xi} \qquad (3.4)$$

The nucleon angular momentum dependence shows up in the order of the split energy branches in the Nilsson plots [124, 126]. The parameters η and ξ can be viewed as deformation parameters of the nuclei. For positive deformation $\eta > 1$ (prolate) and for negative deformation $\eta < 1$ (oblate). As there is a predominance on nuclear prolate deformations in nature most of the nuclei we consider will be prolate.

We indirectly include spin-orbit and angular momentum terms of the Nilsson Hamiltonian through the split level Nilsson energy plots in ref. [126]. The collective enhancement of MQM for some heavy deformed nuclei were estimated in [74, 77] where they considered the contribution using a spherical wave function basis. In this work we will use the Nilsson model of the the nucleus which is an empirically successful single particle model which accounts for the quadrupole deformation of a nucleus by using an anisotropic oscillator potential [124, 128, 126]. In the Nilsson model the deformation breaks the degeneracy of the isotropic shell model which results in several overlapping partially filled nuclear shells containing a large number of nucleons. Each nucleon in the Nilsson model is defined in the Nilsson basis $[Nn_z\Lambda\Omega]$ where N is the principle shell number ($N = n_x + n_y + n_z$), Λ is the projection of the orbital angular momentum on the deformation axis (chosen to be the z-axis) and $\Omega = \Lambda + \Sigma$ is the projection of the total angular momentum of the nucleon on the deformation axis.

Chapter Four

The weak quadrupole moment and Lorentz violation in nuclei

Non-spherical nuclei present a lucrative avenue for studying the existence and magnitude of second order tensor properties due to the collective properties of deformed nuclei. In this chapter we focus on the quadrupole moment of the nonspherical distribution of neutrons in the nucleus, Q_n, the weak quadrupole moment (WQM), $Q_W^{(2)}$, and the violation of Local Lorentz invariance (LLI) in the nucleon sector. The results of this chapter have been published in reference [2]

In reference [127] the $s-d$ shell model calculations of the tensor LLIV effects have been performed in ^{21}Ne, ^{131}Xe and ^{201}Hg nuclei. It was demonstrated that virtual excitations from the nuclear core enhance the nuclear quadrupole moment and suppress the LLIV tensor. The results of the $s-d$ shell model calculations have been supported by the calculations in the Hartree-Fock-Bogoliubov model published in the same paper [127].

4.1 Lorentz invariance violation in deformed nuclei

The LLIV momentum tensor Hamiltonian δH [52]

$$\delta H = \left[-c_{ij} - \frac{1}{2} c_{00} \delta_{ij} \right] \frac{p_i p_j}{m^2}, \tag{4.1}$$

where m is the nucleon mass, to describe the tensor parameter c_{ij} for the LLIV interaction [52] in the laboratory frame. Taking the expectation value of equation (4.1), we find that the LLIV energy shift for a nucleus with N_ν nucleons with angular momentum projection I_ν is given by

$$< \delta H >_\nu = \frac{1}{6m} C_{0,\nu}^{(2)} \sum_{N=1}^{N_\nu} \left\langle I_\nu, I_\nu \left| \hat{M} \right| I_\nu, I_\nu \right\rangle \tag{4.2}$$

where the $\hat{M} = 2\hat{p}_z^2 - \hat{p}_x^2 - \hat{p}_y^2$ is the momentum tensor operator for $p_i p_j$ in the SME in cartesian coordinates. We use the standard notion $C_{0,\nu}^{(2)} = c_{xx} + c_{yy} - 2c_{zz}$ [52]. We define the single nucleon LLIV momentum tensor as,

$$\bar{m}_{i,\nu} = \left\langle I, I \left| 2\hat{p}_z^2 - \hat{p}_x^2 - \hat{p}_y^2 \right| I, I \right\rangle. \tag{4.3}$$

Using the virial theorem for a harmonic oscillator ($\langle T \rangle = \langle U \rangle$) and energy spectrum again we have the average square of the momentum given by

$$\frac{\left\langle p_z^2 \right\rangle}{2m} = \frac{\hbar \omega_z \left(n_z + 1/2 \right)}{2} \tag{4.4}$$

with similar expressions for x and y coordinates.

Using equations (4.3) and (4.4) we write the contribution to the LLIV tensor of a nucleon as,

$$\bar{m}_{i,\nu} = \hbar m \left[(2n_z + 1)_{i,\nu} \, \omega_z - (N - n_z + 1)_{i,\nu} \, \omega_\perp \right]. \tag{4.5}$$

The total LLIV tensor, M_ν, for the nucleus is the sum of all respective nucleons

$$M_\nu = \sum_{i,\nu} \bar{m}_{i,\nu}$$

$$= \hbar m \left[\omega_z \sum_i (2n_z + 1)_{i,\nu} - \omega_\perp \sum_i (N - n_z + 1)_{i,\nu} \right]. \tag{4.6}$$

23

This will result in a quadrupole energy shift given by

$$\langle \delta H \rangle_\nu = \frac{M_\nu}{6m} C_{0,\nu}^{(2)}. \tag{4.7}$$

$$Q_\nu = \frac{41.5 \text{ MeVfm}^2}{\hbar\bar{\omega}} \left[\eta \sum_i (2n_z + 1)_{i,\nu} - \xi \sum_i (N - n_z + 1)_{i,\nu} \right] \tag{4.8}$$

$$M_\nu = \hbar\bar{\omega}m \left[\frac{1}{\eta} \sum_i (2n_z + 1)_{i,\nu} - \frac{1}{\xi} \sum_i (N - n_z + 1)_{i,\nu} \right]. \tag{4.9}$$

4.2 Quadrupole moment of neutron distribution in deformed nuclei

The quadrupole moment tensor along the symmetry axis of the nucleus in cartesian coordinates is given by

$$Q_{zz} = Q = 2 \langle z^2 \rangle - \langle x^2 \rangle - \langle y^2 \rangle . \tag{4.10}$$

From the virial theorem for bound particle in a harmonic oscillator potential the average kinetic energy $\langle T \rangle$ and average potential energy $\langle U \rangle$ are equal. Using the well known energy spectrum for the harmonic oscillator $E_n = \hbar\omega(n + 1/2)$ the average of the square of the position in the z direction is,

$$m\omega_z^2 \langle z^2 \rangle = \hbar\omega_z (n_z + 1/2) \tag{4.11}$$

with similar relations for $\langle x^2 \rangle$ and $\langle y^2 \rangle$. Using equations (4.10), (4.11) and $n_x + n_y = N - n_z$ the contribution to the quadrupole moment from a single nucleon in the quantum state $[Nn_z\Lambda\Omega]$ is given by

$$q_{i,\nu} = \frac{\hbar}{m} \left[\frac{(2n_z + 1)_{i,\nu}}{\omega_z} - \frac{(N - n_z + 1)_{i,\nu}}{\omega_\perp} \right], \tag{4.12}$$

where $\nu = p, n$ for the ith proton or neutron respectively. The total quadrupole moment is the sum of all the respective nucleon quadrupole moment contribu-

tions

$$Q_\nu = \sum_i q_{i,\nu}$$

$$= \frac{\hbar}{m} \left[\frac{1}{\omega_z} \sum_i (2n_z + 1)_{i,\nu} - \frac{1}{\omega_\perp} \sum_i (N - n_z + 1)_{i,\nu} \right]. \qquad (4.13)$$

4.3 Example calculation of Q_ν and M_ν for the ^{173}Yb nucleus

To illustrate the process of calculating NQMN and LLIV values we will present the calculation of ^{173}Yb as an example. To begin we find the nuclear configuration of protons and neutrons in the deformed field using the energy level plots presented in [124, 126] by filling each non-degenerate Ω energy branch with two nucleons until all the nucleons have been distributed. To find the correct deformation, δ, from which to fill we use the experimental value of the nuclear spin (which is solely due to the unpaired nucleon). The filling must be done such that the unpaired nucleon is in the correct spin state. The nuclear spin of ^{173}Yb is $5/2^-$ due to an unpaired neutron. Using the method described above we find that this is possible with a minimum deformation of $\delta \approx 0.3$. Here we will only present the configuration of the partially filled N shells. The numbers for each full shell is given in Table A.1. The incomplete neutron and proton shells in ^{173}Yb are $N = 5, 6$ and $N = 4, 5$ respectively. The nucleon configuration of the incomplete shells are given in Table 4.1.

Table 4.1: Nilsson configuration of ^{173}Yb nucleons: This table shows the nuclear configuration of nucleons in the Nilsson model for ^{173}Yb generated from the Nilsson plots in Ref. [126]. This table shows only partially filled N shells. All preceding shells are completely filled.

Neutrons in incomplete shells		$\sum (2n_z + 1)_n$	$\sum (N - n_z + 1)_n$	Protons in incomplete shells		$\sum (2n_z + 1)_p$	$\sum (N - n_z + 1)_p$
$2f_{7/2}$:	$\pm 1/2[530]$, $\pm 3/2[521]$, $\pm 5/2[512]$	30	24	$1g_{7/2}$:	$\pm 1/2[431]$, $\pm 3/2[422]$, $\pm 5/2[413]$	30	18
$1h_{9/2}$:	$\pm 1/2[541]$, $\pm 3/2[532]$, $5/2[523]$	37	14	$2d_{5/2}$:	$\pm 1/2[420]$, $\pm 3/2[411]$	16	14
$3p_{3/2}$:	$\pm 1/2[521]$	10	8	$2d_{3/2}$:	$\pm 1/2[521]$	6	8
$1h_{11/2}$:	$\pm 1/2[550]$, $\pm 3/2[541]$, $\pm 5/2[532]$, $\pm 7/2[523]$, $\pm 9/2[514]$, $\pm 11/2[505]$	72	42	$1g_{9/2}$:	$\pm 1/2[440]$, $\pm 3/2[431]$, $\pm 5/2[422]$, $\pm 7/2[413]$, $\pm 9/2[404]$	50	30
$1i_{13/2}$:	$\pm 1/2[660]$, $\pm 3/2[651]$, $\pm 5/2[642]$, $\pm 7/2[633]$	80	20	$1h_{11/2}$:	$\pm 1/2[550]$, $\pm 3/2[541]$, $\pm 5/2[532]$, $\pm 7/2[523]$	64	20
Total		229	108	Total		166	90

Summing up the contribution for all the ^{173}Yb filled shells from Table A.1 and the partially filled shells from Table 4.1 the total values for neutrons are $\sum(2n_z + 1)_n = 439$, $\sum(N - n_z + 1)_n = 318$ and protons $\sum(2n_z + 1)_p = 266$, $\sum(N - n_z + 1)_p = 190$. Using equation (3.2) to transform the measured value of the quadrupole moment in the lab frame $Q_p^{Lab} = 4.39$ barn (where 1 barn = 100 fm^2 = 10^{-24} cm^2) to the internal (rotating) frame we have $Q_p^{int} = 12.66$ barn. Using equation (4.8), the values for $\sum(2n_z + 1)_p$, $\sum(N - n_z + 1)_p$ and Q_p^{int} we find the dimensionless deformation parameters $\eta = 1.18$ and $\xi = 0.93$ for ^{173}Yb. We can find the NQMN and the proton and neutron LLIV tensors using (4.8) and (4.9). Finally in the lab frame using (3.2) we have, Using equations (4.8) and (4.9) to calculate the total NQMN and LLIV momentum tensors in the intrinsic frame, and equation (3.2) to transform back to the laboratory frame we find,

$$Q_n^{\text{Lab}} = 4.53 \text{ barn}$$
$$M_p^{\text{Lab}} = 54.30 \quad m \text{ MeV}$$
$$M_n^{\text{Lab}} = 77.25 \quad m \text{ MeV}$$

for the ^{173}Yb. From (4.7) we find that the LLIV energy shift of the nucleus is,

$$\langle \delta H \rangle_p = 9.05 \quad C_{0,p}^{(2)} \text{ MeV}$$
$$\langle \delta H \rangle_n = 12.875 \quad C_{0,n}^{(2)} \text{ MeV}$$

Considering only the contribution of the unpaired neutron in the Schmidt model (see Section 4.4 or Refs. [52, 112]) gives energy shifts $\langle \delta H \rangle_p = 0$ $C_{0,p}^{(2)}$MeV and $\langle \delta H \rangle_n = 0.8$ $C_{0,n}^{(2)}$MeV. The collective contribution of paired nucleons in the core gives non zero LLIV energy shifts for both protons and neutrons (in the Schmidt model either the proton or neutron LLIV shift will always be zero) and enhances the LLIV energy shifts by an order of magnitude. This method can be completed with all the other deformed nuclei, the Nilsson quantum numbers can be found in Table 4.2 and the quadrupole moment values are presented in Table 4.3.

To understand the propagation of error in the calculations consider an error of 5% in Q_p (experimental value is $Q_p = 2.80(4)$ barn). Using equations (4.13), (4.6) along with the Nilsson numbers for ^{173}Yb results in an error of $\approx 5\%$ for Q_n and an error of $\approx 25\%$ for M_ν. This large error is not unique to our calculation of M_ν since it involves the subtraction of large numbers. Consider the results from [127] where a sophisticated numerical $s - d$ model resulted in similar uncertainty for slight variations of an effective charge for the quadrupole

Table 4.2: Sum of proton and neutron Nilsson quantum numbers and deformation parameters for deformed nuclei: This table shows the sum of $2n_z + 1$ and $N - n_z + 1$ for all nucleons in the nuclei.

	Proton (Σ_p)		Neutron (Σ_n)		$\bar{\omega}/\omega_z$
	$2n_z + 1$	$N - n_z + 1$	$2n_z + 1$	$N - n_z + 1$	
^{9}Be	8	4	9	6	1.68
^{21}Ne	22	14	25	16	1.30
^{27}Al	29	21	30	24	1.12
^{151}Eu	199	177	312	276	1.08
^{153}Eu	241	162	350	272	1.11
^{163}Dy	250	174	389	287	1.12
^{167}Er	260	182	417	302	1.17
^{173}Yb	266	190	439	318	1.18
^{177}Hf	264	202	439	331	1.18
^{179}Hf	264	202	447	341	1.16
^{181}Ta	285	199	468	338	1.08
^{229}Th	362	268	625	502	1.22

moment operator.

4.4   Nuclei with a small deformation

For nuclei with very small deformations the splitting of energy levels with different angular momentum projections is small. In these circumstances the effect of nuclear pairing becomes significant resulting in mixing of the nucleon configurations. Therefore the Nilsson model approach is no longer applicable as it assumes that there is no mixing when counting the nucleon occupation numbers. For these near-spherical nuclei we need to approach the second order tensor properties differently. It is well known that the Schmidt model (valence, $Q_{\nu,\text{val}}$) value of nuclear quadrupole is smaller than the true quadrupole value. Therefore we assume that this discrepancy is explained by the quadrupole moment due to a small deformation (deformed, $Q_{\nu,\text{def}}$), i.e. the true quadrupole moment is the sum of these two contributions, $Q_\nu = Q_{\nu,\text{val}} + Q_{\nu,\text{def}}$. We also assume that $Q_{\nu,\text{def}}$ for protons and neutrons is related to the total number of protons and neutrons,

$$\frac{1}{Z} Q_{p,\text{def}} = \frac{1}{N} Q_{n,\text{def}}. \tag{4.14}$$

Then using measured Q_p values from [120] we can find an estimate for the neutron quadrupole moment of slightly deformed nuclei. As an example consider the ^{201}Hg nucleus which has a small electric quadrupole moment $Q_p = 0.35$ barn

with a valence neutron. There is no proton Schmidt contribution to Q_p meaning the quadrupole moment due to the deformation is

$$Q_{p,\text{def}} = Q_p = 0.35 \text{ barn}$$

From Eq. (4.14) the contribution to Q_n due to deformation is $Q_{n,\text{def}} = 0.53$ barn. The Schmidt model contribution of a valence nucleon is given by [119, 112]

$$Q_n^{\text{Lab}} = -\frac{I - 1/2}{I + 1} \left\langle r^2 \right\rangle \tag{4.15}$$

$$= -\frac{I - 1/2}{I + 1} 0.009 A^{2/3} \text{ barn.} \tag{4.16}$$

The ^{201}Hg nucleus has a valence neutron in the $f_{5/2}$ state with angular projection $I = 3/2$. Using equation (4.15) the valence contribution is $Q_{n,\text{val}} = -0.15$ barn. Therefore the total NQMN for ^{201}Hg is $Q_n = 0.38$ barn where all values are in the labratory frame. As expected this value is larger than Q_p. For the LLIV tensor we use the method outlined in [112] which relates the LLIV energy shift to the quadrupole moment of the nucleus,

$$\langle \delta H \rangle_\nu = \frac{M_\nu}{6m} C_{0,\nu}^{(2)} = 1100 A^{-2/3} Q_\nu C_{0,\nu}^{(2)} \text{ MeV.} \tag{4.17}$$

In this work we use the total quadrupole moment including the valence and deformed contribution discussed above. Similar to the NQMN this will give non zero values for both nucleons unlike the Schmidt model. Using equation (4.17) for ^{201}Hg nucleus we have $\langle \delta H \rangle_n = 17\ C_{0,n}^{(2)}$ MeV and $\langle \delta H \rangle_p = 11.2\ C_{0,p}^{(2)}$ MeV. Similar calculations can be performed for Q_n and M_ν in other slightly deformed nuclei such as ^{131}Xe, ^{133}Cs which are presented in Table 4.3. In [127] the LLIV and quadrupole moments were calculated for ^{21}Ne, ^{131}Xe and ^{201}Hg numerically using a self-consistent mean field theory. Our results for ^{21}Ne, where we use the large deformation method, are in a reasonable agreement with the results of Ref. [127] results for both Q_n and M_ν ($Q_n = 0.097$ barn, $M_p = 2.8\ m$ MeV and $M_n = 4.2\ m$ MeV). For nuclei ^{201}Hg and ^{131}Xe, where we use the small deformation method, there is a reasonable agreement for Q_n and significant differences for M_ν. In Ref. [127] they obtained for ^{201}Hg $Q_n = 0.584$ barn, $M_p = -20.5\ m$ MeV and $M_n = 1.5\ m$ MeV, and for ^{131}Xe their results are $Q_n = -0.136$ barn, $M_p = -4.7\ m$ MeV and $M_n = 5.17\ m$ MeV.

Table 4.3: Results for LLIV and quadrupole tensors for different deformed nuclei: (All used Q_p values have been compiled in [120].) This table shows the proton (Q_p) and neutron (Q_n) electric quadrupole moments, energy shifts due to Lorentz violation ($\langle \delta H \rangle_\nu$) and the weak quadrupole moments ($Q_W^{(2)}$) in ^{9}Be, ^{21}Ne, ^{27}Al, ^{131}Xe, ^{133}Cs, ^{163}Dy, ^{173}Yb, ^{177}Hf, ^{179}Hf, ^{181}Ta, ^{201}Hg and ^{229}Th. All quantities are in the lab frame. Nuclei marked with an asterix (*) are near spherical nuclei.

Nuclei	I_t	Q_p (barn)	Q_n (barn)	M_p (m MeV)	M_n (m MeV)	$\dfrac{<\delta H>_p}{C_{0,p}^{(2)}}$ (MeV)	$\dfrac{<\delta H>_n}{C_{0,n}^{(2)}}$ (MeV)	$Q_W^{(2)}$ (barn)
^{9}Be	$\frac{3}{2}-$	+0.0529(4)	+0.053	-0.14	-5.88	-0.024	-1	-0.05
^{21}Ne	$\frac{3}{2}+$	+0.103(8)	0.12	3.19	3.36	0.53	0.56	-0.11
^{27}Al	$\frac{5}{2}+$	+0.150(6)	0.129	17.12	7.26	2.85	1.21	-0.12
^{131}Xe*	$\frac{3}{2}+$	-0.114	-0.070	-29.4	-18	-4.9	-3	-0.009
^{133}Cs*	$\frac{7}{2}+$	-0.00355	0.2	-0.9	53	-0.15	9	-0.20
^{151}Eu	$\frac{5}{2}+$	+0.87(2)	1.4	2.45	8	0.41	1.3	-1.33
^{153}Eu	$\frac{5}{2}+$	+2.28(9)	2.53	127	81	21	13.5	-2.35
^{163}Dy	$\frac{5}{2}-$	+2.318(2)	3.3	103.4	115.5	17	19	-3.10
^{167}Er	$\frac{7}{2}+$	3.57(3)	5.47	90	107	15	18	-5.17
^{173}Yb	$\frac{5}{2}-$	+2.8(4)	4.5	54	77	9	13	-4.26
^{177}Hf	$\frac{7}{2}-$	+3.37(3)	5.73	16.35	45	2.7	7.5	-5.44
^{179}Hf	$\frac{9}{2}+$	+3.79(3)	6.5	35.33	64	6	10.5	-6.17
^{181}Ta	$\frac{7}{2}+$	+3.17(2)	5.33	188	269.5	31	45	-5.05
^{201}Hg*	$\frac{3}{2}+$	+0.35	0.53	67.2	102	11.2	17	-0.50
^{229}Th	$\frac{5}{2}+$	+4.3(9)	6.62	14	-78	2	-13	-6.25

4.5 Weak quadrupole moments and parity non-conservation in atomic and molecular systems

As mentioned in Section **??** previously mentioned above a consequence of studying the NQMN will be further insight into parity nonconservation (PNC) effects in atomic and molecular systems. PNC has been intensively studied in atomic systems (see e.g. book [68] and reviews [109, 108]). The P-odd weak nucleon-electron interaction is given by,

$$H_W = -\frac{G_F}{2\sqrt{2}}\gamma_5\left[Zq_{w,p}\rho_p(r) + Nq_{w,n}\rho_n(r)\right] \tag{4.18}$$

Here G_F is the Fermi weak constant, $q_{w,\nu}$ and $\rho_\nu(r)$ are the nucleon weak charge and density of protons or neutrons normalised to 1. It is well known that the magnitude of the neutron weak charge is significantly larger than that of the proton. Not including radiative corrections the weak charges are given by

$$q_{w,p} = 1 - 4\sin^2\theta_W \approx 0.08,$$
$$q_{w,n} = -1,$$

where θ_W is the Weinberg angle. Previously the interaction given by equation (4.18) treated either the shapes of the proton and neutron densities the same or included a correction due to some neutron skin (see e.g. review [109]). The quadrupole moment in the nuclear density produces the tensor weak interaction which is proportional to the weak quadrupole moment (WQM) defined as [140]

$$Q_W^{(2)} = q_{w,p}Q_p + q_{w,n}Q_n.$$

Similar to the weak charge of a nucleus the WQM is dominated by the neutron contribution, $Q_W^{(2)} \approx q_{w,n}Q_n$, with a small correction due to the proton contribution.

The nuclear WQM induces PNC effects in atomic and molecular systems where the effective single electron PNC Hamiltonian for the nuclear WQM in atomic systems is presented in Ref. [140] and is given by,

$$H_{WQM} = -\frac{G_F}{2\sqrt{2}}\gamma_5 Y_{20}\rho_0\frac{\sqrt{5\pi}Q_W^{(2)}}{\langle r^2 \rangle}$$

where G_F is the Fermi weak constant, γ_5 is the standard Dirac matrix, Y_{20} is

the spherical harmonic, ρ_0 is the spherical nucleon density and $\langle r^2 \rangle$ is the mean squared nuclear radius. While calculations of these PNC effects is outside the scope of this work they can be observed in atomic and molecular systems in many ways (see refs. [140, 109, 68, 108]) using interference of forbidden electric dipole transition amplitude with M1 (or E2) amplitude between the states of equal parity [140].

Also the PNC effects of the tensor weak interaction which has different selection rules are strongly enhanced and can be measured in atoms and molecules having close opposite parity energy levels with the difference of the electron angular momenta equal to 2. Corresponding states can be mixed by the tensor weak interaction but not the scalar (proportional to the weak charge) and vector (proportional to the nuclear anapole moment) components. If the difference of the electron angular momenta is 1 the effects of the anapole and the weak quadrupole may be separated due the difference in their contributions to the different hyperfine components of the electromagnetic transitions. Corresponding atomic calculations have been performed in Ref. [140]. Measurements of the tensor PNC effects in atoms and molecules will allow one to extract the neutron quadrupole moment of the nuclei.

Chapter Five

The magnetic quadrupole moment of the nucleus

The results of this chapter have been published in reference [4]

In this chapter I present the calcuation of the nuclear MQM in specific deformed nuclei along with the induced energy shifts in polar diatomic molecules. The results are presented in terms of fundamental $T-$ and $P-$ violating parameters in the neutron EDM, d_n , the quark chromo-EDMs and the $CP-$ violating QCD $\bar{\theta}$ term.

5.1 MQM Calculation

The magnetic quadrupole moment of a nucleus due to the electromagnetic current of a single nucleon with mass m is defined by the second order tensor operator [69],

$$\hat{M}_{kn}^{\nu} = \frac{e}{2m} \left[3\mu_{\nu} \left(r_k \sigma_n + \sigma_k r_n - \frac{2}{3} \delta_{kn} \hat{\boldsymbol{\sigma}} \mathbf{r} \right) \right.$$
$$\left. + 2q_{\nu} \left(r_k l_n + l_k r_n \right) \right] \tag{5.1}$$

where $\nu = p, n$ for protons and neutrons respectively and, μ_{ν} and q_{ν} are the magnetic moment and charge of the nucleon respectively. The nuclear MQM is T-,P- odd and therefore it is forbidden in the absence of nucleon EDMs and T-, P- odd nuclear forces. It is understood the shell nucleons interact with the core of the nucleus through a $P-$ and $T-$ odd potential [74, 69, 68]. This results in

a perturbed "spin hedgehog" wavefunction of a nucleon given by [69, 74],

$$|\psi'\rangle = \left(1 + \frac{\xi_\nu}{e}\hat{\boldsymbol{\sigma}}\hat{\boldsymbol{\nabla}}\right)|\psi_0\rangle \tag{5.2}$$

$$\xi_\nu \approx -2 \times 10^{-21}\eta_\nu \ e \cdot \text{cm}$$

where $\nu = p, n$ for protons and nucleons respectively. Here η_ν represent T-,P- odd nuclear strength constants from the T-,P- violating nuclear potential $H_{T,P} = \eta_\nu G_F/(2^{3/2}m_\nu)(\boldsymbol{\sigma}\cdot\nabla\rho)$ and $|\psi_0\rangle$ is the unperturbed nucleon wavefunction. Here ρ is the total nuclear number density and G_F is the Fermi weak constant. It should be noted that we used T-,P- odd interaction in the contact limit while the actual interaction has a finite range due to the pion exchange contribution. Another approximation used in the derivation of the Eq. (5.2) is that the strong potential and nuclear density have similar profiles (not necessarily the spherical one). These approximations introduce a sizeable theoretical uncertainty. Using (5.1) and (5.2) the MQM for a single nucleon due to the P-, T- odd valence-core interaction is given by,

$$M^{TP} = M_{zz}^{TP} = \xi\frac{2}{m}\left(\mu\left\langle\sigma\cdot l\right\rangle - q\left\langle\sigma_z l_z\right\rangle\right). \tag{5.3}$$

In the Nilsson basis [124] the nucleon's total angular momentum projection onto the symmetry axis is given by $\Omega_N = \Lambda_N + \Sigma_N$, where $\Sigma_N = \pm 1/2$ is the spin projection and Λ is the orbital angular momentum projection of the nucleon. In this basis the MQM generated by the spin-hedgehog Eq. (5.2) is given by,

$$M_\nu^{TP} = 4\Sigma_N\Lambda_N\xi\left(\mu_\nu - q_\nu\right)\frac{\hbar}{m_p c}. \tag{5.4}$$

The orbit of a permanent electric dipole moment (EDM) also generates a contribution to the nuclear MQM, $M_\nu^{EDM} \propto d_\nu$ [141]. As both the proton and neutron are expected to have an EDM both will contribute to the MQM. From [77] using a valence nucleon approach the ratio of the two contributions M_ν^{TP}/M_ν^{EDM} is independent of the total angular momentum, I, of the nucleon. Therefore up to non diagonal elements of definite I the ratio is the same in the Nilsson model. That is,

$$M_\nu^{EDM} \approx 4\Sigma_N\Lambda_N d_\nu \frac{\hbar}{m_p c}. \tag{5.5}$$

Table 5.1: Total nuclear MQM for each quadrupole deformed nucleus calculated using the Nilsson model. This table presents both the proton and neutron contributions to the total nuclear MQM in the laboratory frame.

Nuclei	I_t^π	M	Nuclei	I_t^π	M
^9Be	$\frac{3}{2}^-$	$0M_0^p + 0.4M_0^n$	^{167}Er	$\frac{7}{2}^+$	$21M_0^p + 36M_0^n$
^{21}Ne	$\frac{3}{2}^+$	$0M_0^p + 0.4M_0^n$	^{173}Yb	$\frac{5}{2}^-$	$14M_0^p + 26M_0^n$
^{27}Al	$\frac{5}{2}^+$	$3M_0^p + 4.5M_0^n$	^{177}Hf	$\frac{7}{2}^-$	$17M_0^p + 42M_0^n$
^{151}Eu	$\frac{5}{2}^+$	$12M_0^p + 23M_0^n$	^{179}Hf	$\frac{9}{2}^+$	$20M_0^p + 50M_0^n$
^{153}Eu	$\frac{5}{2}^+$	$12M_0^p + 20M_0^n$	^{181}Ta	$\frac{7}{2}^+$	$19M_0^p + 45M_0^n$
^{163}Dy	$\frac{5}{2}^-$	$11M_0^p + 21M_0^n$	^{229}Th	$\frac{5}{2}^+$	$13M_0^p + 27M_0^n$

Therefore, the MQM generated by a single nucleon is given by,

$$M_\nu = 4\Sigma_N \Lambda_N M_\nu^0$$
$$M_\nu^0 = [\xi (\mu_\nu - q_\nu) + d_\nu] \frac{\hbar}{m_p c}. \tag{5.6}$$

Using the Nilsson model we can find the total MQM of the nucleus by summing up every nucleon in the open and closed shells. To find the nuclear configuration of each species we have to first identify the quadrupole deformation of the nucleus. In odd-A nuclei there is one unpaired nucleon which defines the nucleus' spin and parity (I_t^π). Therefore we find the correct deformation factor δ of the nucleus by filling up each energy level in the Nilsson energy diagrams [126] such that the final configuration results in the correct nuclear spin and parity (see Ref. [142]). For any odd-A isotope the nuclear MQM in laboratory frame can be found using (3.2) and (5.6) if the condition $I_t \geq 3/2$ is satisfied. The nuclear MQM for nuclei of experimental interest are presented in Table ??. We do not consider configuration mixing in our MQM calculations. Configuration mixing has been shown to suppress the nuclear EDM and spin matrix elements with partially filled nuclear shells [143, 144, 145]. A similar effect may appear for MQM.

Comparing these nuclear MQMs to those presented in [77] we see that the use of the deformed Nilsson orbitals instead of the spherical orbitals leads to a significant increase of the results. For example, in the Hafnium isotopes ^{177}Hf and ^{179}Hf the neutron contribution is enhanced by a factor of 3. Similarly, for ^{179}Yb the neutron contribution has doubled. Note also that MQMs in these heavy quadrupole deformed nuclei are an order of magnitude larger than MQM

due to a valence proton ($\sim M_0^p$) or neutron ($\sim M_0^n$) in spherical nuclei.

The T-,P- odd nuclear potential which generated the MQM is dominated primarily by the neutral π_0 exchange. We can express the strength constants η_ν in the T-,P- violating nuclear potential $H_{T,P}$ in terms of the strong πNN coupling constant g and three T-,P-odd coupling constants, corresponding to the different isotopic channels, g_i where $i = 0, 1, 2$. For heavy nuclei the results are the following [146, 69]:

$$\eta_n = -\eta_p \approx 5 \times 10^6 g \left(\bar{g}_1 + 0.4\bar{g}_2 - 0.2\bar{g}_0 \right). \tag{5.7}$$

We can rewrite the contribution of both the proton and nucleon MQMs in terms of these coupling constants [74, 147],

$$
\begin{aligned}
M_p^0(g) = \Bigg[&g \left(\bar{g}_1 + 0.4\bar{g}_2 - 0.2\bar{g}_0 \right) \\
&+ \frac{d_p}{1.2 \times 10^{-14}\ e \cdot \mathrm{cm}} \Bigg] 3.0 \times 10^{-28}\ e \cdot \mathrm{cm}^2
\end{aligned} \tag{5.8}
$$

$$
\begin{aligned}
M_n^0(g) = \Bigg[&g \left(\bar{g}_1 + 0.4\bar{g}_2 - 0.2\bar{g}_0 \right) \\
&+ \frac{d_p}{1.3 \times 10^{-14}\ e \cdot \mathrm{cm}} \Bigg] 3.2 \times 10^{-28}\ e \cdot \mathrm{cm}^2.
\end{aligned} \tag{5.9}
$$

We can write the contributions of the T-,P-odd πNN interaction and nucleon EDMs in terms of more fundamental T-,P- violating parameters such as the QCD CP- violating parameter $\bar{\theta}$ which is the heart of the strong CP problem, or in terms of the EDMs d and chromo-EDMs $\tilde{d}$ of u and d quarks. They are [148, 149, 10, 150, 151, 152]:

$$g\bar{g}_0(\bar{\theta}) = -0.37\bar{\theta} \tag{5.10}$$

$$
\begin{aligned}
g\bar{g}_0(\tilde{d}_u, \tilde{d}_d) &= 0.8 \times 10^{15} \left(\tilde{d}_u - \tilde{d}_d \right)\ \mathrm{cm}^{-1} \\
g\bar{g}_1(\tilde{d}_u, \tilde{d}_d) &= 4 \times 10^{15} \left(\tilde{d}_u + \tilde{d}_d \right)\ \mathrm{cm}^{-1}
\end{aligned} \tag{5.11}
$$

$$
\begin{aligned}
d_p(d_u, d_d, \tilde{d}_u, \tilde{d}_d) &= 1.1e \left(\tilde{d}_u + 0.5\tilde{d}_d \right) + 0.8d_u - 0.2d_d \\
d_n(d_u, d_d, \tilde{d}_u, \tilde{d}_d) &= 1.1e \left(\tilde{d}_d + 0.5\tilde{d}_u \right) - 0.8d_d + 0.2d_u
\end{aligned} \tag{5.12}
$$

where the chromo-EDM contributions in eqs. (5.11) and (5.12) arise from the Peccei-Quinn mechanism [153, 10]. The corresponding substitutions give the following results for the dependence on $\tilde{\theta}$ of proton and neutron MQM contri-

butions:

$$M_p^0(\bar{\theta}) = 1.9 \times 10^{-29}\bar{\theta}\ e \cdot \text{cm}^2$$
$$M_n^0(\bar{\theta}) = 2.5 \times 10^{-29}\bar{\theta}\ e \cdot \text{cm}^2.$$
(5.13)

The dependence on the up and down quark EDMs is

$$M_p^0(\tilde{d}_u - \tilde{d}_d) = 1.2 \times 10^{-12}(\tilde{d}_u - \tilde{d}_d)\ e \cdot \text{cm}$$
$$M_n^0(\tilde{d}_u - \tilde{d}_d) = 1.3 \times 10^{-12}(\tilde{d}_u - \tilde{d}_d)\ e \cdot \text{cm}.$$
(5.14)

While there have been more sophisticated treatments of the πNN interaction with respect to $\bar{\theta}$[154, 155, 145, 156] and the quark chromo-EDMs [157, 158, 155, 145, 156] the values used above are within the accuracy of our model.

5.2 MQM energy shift in diatomic molecules

Direct measurement of the nuclear MQM is unfeasible and a more indirect method is required. As mentioned above the use of neutral molecular systems is promising as the nuclear MQM will interact with the internal electromagnetic field. Molecules in particular present a lucrative option due to existence of very close paired levels of opposite parity, the Ω-doublet - see e.g. [77]. For highly polar molecules consisting of a heavy and light nucleus (for example, Th and O) the effect of MQM is $\sim Z^2$, therefore it is calculated for the heavier nucleus. The Hamiltonian of diatomic paramagnetic molecule including the $T, P-$ odd nuclear moment effects is given by [69, 159]:

$$H = W_d d_e \mathbf{S} \cdot \mathbf{n} + W_Q \frac{Q}{I}\mathbf{I} \cdot \mathbf{n} - \frac{W_M M}{2I(2I-1)}\mathbf{S}\hat{\mathbf{T}}\mathbf{n},$$
(5.15)

where d_e is the electron EDM, Q is the nuclear Schiff moment, M is the nuclear MQM, $\mathbf{S}$ is the electron spin, $\mathbf{n}$ is the symmetry axis of the molecule, $\hat{\mathbf{T}}$ is the second rank tensor operator characterised by the nuclear spins $T_{ij} = I_i I_j + I_j I_i - \frac{2}{3}\delta_{ij}I(I+1)$ and W_d, W_Q and W_M are fundamental parameters for each interaction which are dependent on the particular molecule. We have omitted the P-,T- odd electron-nucleon interaction terms which are presented e.g. in reviews [160, 67]. These parameters W_d, W_Q and W_M are related to the electronic molecular structure of the state. For each molecule there is an effective field for each fundamental parameter, these effective fields are calculated using many-body methods for electrons close to the heavy nucleus [77]. For the nuclear MQM we are interested only in W_M which has been calculated for molecules YbF [159], HfF$^+$[161], TaN [105, 106], TaO$^+$[107], ThO [98] and ThF$^+$[103]. Using these vales we present the results for the energy shifts in

Table 5.2: Frequency shifts due to the MQM interaction with the electron magnetic field of the molecules. We present the energy shifts in terms of the $CP-$ violating parameters of interest. These are the strong $CP-$ term in QCD $\bar\theta$, the permanent EDM of the proton d_p and the difference of quark chromo-EDMs $(\tilde d_u - \tilde d_d)$.

Molecule	I_t^π	State	$\lvert W_M \rvert$ $10^{39}\,\mu\mathrm{Hz}/e\cdot\mathrm{cm}^2$	$\lvert W_M MS \rvert$ (μHz) $10^{25}d_p/e\cdot\mathrm{cm}$	$10^{10}\bar\theta$	$10^{27}(\tilde d_u - \tilde d_d)/\mathrm{cm}$
^{173}YbF	$\frac{5}{2}^-$	$^2\Sigma_{1/2}$	2.1[159]	37	96	53
^{177}HfF$^+$	$\frac{7}{2}^-$	$^3\Delta_1$	0.494[161]	21	68	37
^{179}HfF$^+$	$\frac{9}{2}^+$	$^3\Delta_1$	0.494[161]	25	81	44
^{181}TaN	$\frac{7}{2}^+$	$^3\Delta_1$	1.08[105]	51	159	87
^{181}TaO$^+$	$\frac{7}{2}^+$	$^3\Delta_1$	0.45[107]	21	66	36
^{229}ThO	$\frac{5}{2}^+$	$^3\Delta_1$	1.10[98]	35	102	56
^{229}ThF$^+$	$\frac{5}{2}^+$	$^3\Delta_1$	0.88[103]	28	81	45

molecules induced by MQM in terms of $CP-$ violating parameters $\bar\theta$, d_p and $(\tilde d_u - \tilde d_d)$ in Table 5.2.

The MQM molecular energy shifts for HfF$^+$, TaN, TaO$^+$ and ThO were calculated in Refs. [93], [105], [107] and [98] respectively. They used the MQM calculated in the spherical basis method outlined in [77] and represent the shifts in fundamental T-,P- odd parameters as in Table 5.2. Using the Nilsson model, the MQM energy shifts are larger for TaN, TaO$^+$ and ThO molecules by a factor of 2 however for ^{177}HfF$^+$ the values of the two models are similar. Using the currents limits on the CP-violating parameters [162] $|d_p| < 8.6 \times 10^{-25}$ $e\cdot$cm, $\bar\theta < 2.4 \times 10^{10}$ and $\tilde d_u - \tilde d_d < 6 \times 10^{-27}$ cm the respective MQM energy shifts ($|W_M MS|$) in ^{229}ThO are < 300 μHz, < 250 μHz and 340 μHz. The ^{232}ThO molecule has recently been used to set new limits on the electron EDM with a factor of 12 improvement in accuracy of 80 μHz[163, 164]. As ^{232}Th has an even number of nucleons there is no spectroscopic nuclear MQM. Therefore in principle, if a similar experiment is possible with ^{229}ThO future measurements should improve constraints on nuclear CP- violating interactions. It is interesting to find the minimal SM prediction for the energy shifts which comes solely from the CKM matrix. Using eqs. (5.8) and (5.9), the lower limit on the CKM nucleon EDM $d_p^{\mathrm{CKM}} = -d_n^{\mathrm{CKM}} \approx 1 \times 10^{-32}$ $e\cdot$cm[165] and the strengths of the $CP-$odd pion nucleon couplings in the CKM model

$g\bar{g}_0 \approx -1.6 \times 10^{-16}$, $g\bar{g}_1 \approx -1.8 \times 10^{-16}$ and $g\bar{g}_2 \approx 4.7 \times 10^{-20}$ [166] we find $|M_p^{0,\text{CKM}}| \approx |M_n^{0,\text{CKM}}| \approx 4.5 \times 10^{-44}$ $e\cdot\text{cm}^2$. This corresponds to an energy shift of $|W_M MS| \approx 1$ nHz in ^{229}ThO due to the MQM which is 4 orders of magnitude lower than the current accuracy. Results for other molecules in Table 5.2 are similar.

Chapter Six

Conclusion

We presented a versatile semi-empirical method to calculate several second order tensor properties of nuclei which are enhanced in deformed nuclei including the weak quadrupole moment. Though we present values for only a few deformed nuclei the method can be applied to many nuclei of interest. In particular the highly deformed ^{181}Ta, ^{167}Er, ^{163}Dy and ^{153}Eu have large enhancement of tensor properties and are particularly promising candidates for further study. The theoretical results presented should facilitate experimentalists in probing the nuclear structure and fundamental physics, specifically the previously unstudied quadrupole distribution of neutrons and the violations of Lorentz symmetry. Currently such systems are of high interest as they allow the study of physics beyond the standard model with low energy systems.

This enhancement in deformed nuclei can also be applied for other second order tensor observables of interest such as the time-reversal and parity violating magnetic quadrupole moment. Further study of these tensor properties in deformed nuclei could lead to further understanding of fundamental physics.

In this work we present a novel method for calculating the nuclear MQM for any nuclei that satisfy the angular momentum condition $I_t \geq 3/2$. In heavy nuclei with large quadrupole deformations there is an enhancement of the nuclear MQM due to the collective effect of partially filled nucleon shells and therefore these nuclei present an opportunity for detecting and measuring T-,P- violating effects in the hadronic sector. The molecular systems which have been used to study the electron EDM with promising results are also excellent candidates for measuring the nuclear MQM [161, 98]. With increasing experimental capabilities in paramagnetic molecular systems the possibility of measure these T-,P- violating effects is attractive. The nuclear MQM's and MQM molecular energy shifts presented in this work may allow experimentalists either detect or

constrain the limits of fundamental T-,P- violating nucleon EDM (d_p), strong CP parameter ($\bar{\theta}$) and chromo-EDMs ($\tilde{d}_u - ed_d$).

Part II

Theoretical calculations of Super Heavy Element properties

Chapter Seven

Introduction

Since the beginning of the 10th century the discovery of elements history the discovery and study of new elements has been a constant theme in the scientific discipline. While early discoveries relied on the extracting naturally occurring elements from ores the discovery of transuranium elements (which are not naturally occurring on earth) requires significant investments in facilities. Currently, all elements up to $Z = 118$ (oganesson) have been synthesized and officially recognized by IUPAC. In particular the region of the periodic table for $Z > 100$ are known as super heavy elements (SHEs). While these elements can be synthesized at a rate of a few atoms an hour, they are unstable. The short lifetimes and production rates present a significant problem when attempting to study the physical and chemical properties of the elements.

The sparse theoretical results for elements $Z = 105 - 111$ is due to the open $6d-$shell where current methods are not viable. For more than four valence electrons previous many-body methods become too computationally expensive due to the large diagonalisation problem. The computational cost is reduced by using a combination of the configuration interaction (CI) and perturbation theory (PT). In this section we will give a brief discussion of our implementation of the CIPT method. For an in depth discussion please refer to Ref. [167].

The study of super heavy elements (SHE), $Z > 100$, has been an important field in atomic and nuclear physics for the past century [168, 169]. These exotic elements, which are not found in nature, are interesting particularly in relation to the existence of the 'island of stability' where stable SHE isotopes are expected to be found as predicted by theoretical nuclear shell models [170, 169, 171, 172]. The theoretical study of SHE by means of atomic physics provides an opportunity to study the interplay between correlation and relativistic effects in extreme conditions of heavy many-electron system.

Experimental knowledge of SHEs is still limited due to difficulties caused by

short lifetimes and low production rate. While elements up to Z=118 have been synthesized, the heaviest elements for which experimental spectroscopic data are available are No ($Z = 102$) and Lr ($Z = 103$). The $^1S_0 \rightarrow\, ^1P_1^o$ excitation energy of No ($Z = 102$) [173] and ionisation potentials (IP) of No [173] and Lr ($Z = 103$) [174] have been recently measured. The development and refinement of laser spectroscopy techniques make future measurements in the SHE region promising [175, 176, 177]. The theoretical results presented here will facilitate future experiments.

There has been significant theoretical study of SHEs with a small number of electrons (holes) above (below) closed shells. These calculations have been performed using well-established many-body techniques such as couple-cluster methods [178, 179], CI+MBPT [180], correlation potential (CP) methods [181] and Multiconfigurational Dirac-Fock (MCDF) [182] etc. For SHEs $Z = 102, 103, 104$ which have 2, 3, and 4 valence electrons above the closed $5f$ shell, their spectra, ionisation potentials and static polarisabilities have been calculated [183, 184, 185, 186, 187, 188, 189, 190, 191, 192, 193]. Similarly atomic properties of SHEs $Z = 112 - 118$ using coupled-cluster methods [194, 195, 196, 197, 198, 199, 200, 201, 202], CI+MBPT methods [203, 180] and MCDF methods [204, 205] have been calculated. Elements Mc to Og ($Z = 115 - 118$) have more than three external electrons and theoretical study is limited to calculation of IPs, polarizabilities, electron affinities, etc. but not energy levels (see, e.g. [198]). Atomic properties of elements with $Z = 119 - 122$, which also have simple electron structure, having from one to four valence electrons, have also been theoretically studied [206, 207, **?**, 208, 209, 210, 211, 212, 213, 192]. A review of SHE atomic calculations can be found e.g. in Refs. [192, 214].

Theoretical study of electron structure of superheavy elements (SHE, nuclear charge $Z > 103$) is an important area of research closing the gaps in relevant experimental data. While all SHE up to oganesson (Og, $Z = 118$) have been synthesized and named [215, 169, 170], experimental data on their spectra are absent.

The heaviest elements for which experimental spectroscopic data are available are nobelium (No, $Z = 102$) [173, 216] and lawrencium (Lr, $Z = 103$) [174]. Ionization potential (IP) has been measured for both atoms and the frequency of the strong $7s^2\, ^1S_0 \rightarrow 7s7p\, ^1P_1^o$ electric dipole transition is measured for No. For heavier SHE the data come only from theory. There are many accurate calculations for atoms with relatively simple electronic structure, which includes atoms and ions with few electrons above closed shells (usually not more that four, see, e.g. Refs. [**?**, 217, 218, 219, 220, 221, 222, 223, 224, 225, 226]). This constitutes less then a half of the SHE in the range $104 \le Z \le 118$. Most of the SHE have an open $6d$ or $7p$ shell with more than four electrons. Till recently,

the only available tool to perform calculations for such systems was the multi-configuration Dirac-Fock method (MCDF, see, e.g. review [227]). Some of the MCDF results we discuss in section 10.3. There are some model calculations of the basic parameters of the atoms, such as IP [228] and polarizabilities [62]. Accurate *ab initio* calculations of the spectra are practically absent. This is an unfortunate situation since from the study of relatively simple SHE we know that strong relativistic effects often bring significant difference in properties of SHE compared to their lighter analogs. Similar effects are expected for all SHE, including those with open shells. To address the problem, we have developed efficient versions of the configuration interaction (CI) approach, which allows study of atoms with any number of valence electrons. This includes the so-called CIPT method (configuration interaction with perturbation theory, [167]) and its fast version, the FCI method (fast configuration interaction [229]). Both methods are based on the idea that off-diagonal matrix elements between highly excited states can be neglected in the CI matrix. This allows one to reduce the problem to a much smaller matrix with modified matrix elements. The methods were tested on such open-shell systems as Yb and No (including states with excitations from the $4f$ and $5f$ subshells) [167, 229], Ta [1], W and I [167], and superheavy elements Db [1] and Og [230]. Db is the first SHE with an open $6d$ shell that has been studied using the CIPT method [167, 231]. Its ground-state configuration is $[\text{Rn}]5f^{14}7s^25d^3$, i.e. it has five valence electrons above closed shells, which makes it difficult to use other methods. Lighter neighbours of Db, Rf (four valence electrons) and Lr (three valence electrons) were studied with the use of the powerful CI+all-order method [232, 233]. The use of the latter approach for Db is very problematic and is practically impossible for heavier elements. Following the successful use of the CIPT for Db, we apply it in the present work to heavier elements Sg, Bh, Hs and Mt ($106 \leq Z \leq 109$).

While established numerical methods have been used for SHEs with relatively simple atomic structure, difficulties arise for more than four valences electrons in the open subshells in many-electron atoms ($Z = 105 - 111$) due to the extremely large CI basis which leads to the CI matrix of unmanageable size. This has limited the calculations mostly to ionisation potentials and electric polarizabilites [234, 62, 235, 236]. A recently developed method combining configuration interaction with perturbation theory (the CIPT method [167]) overcomes these limitations, allowing calculation of spectra for the rest of SHE. In this work we calculate the atomic spectra of homologues Ta I and Db I which both have five valence electrons above a closed f shell. The calculation of Ta I is performed to demonstrate the accuracy of the CIPT calculations by comparing with available experimental data.

The wave function for valence electrons has the form of an expansion over

single-determinant basis states. It is assumed that the summation in the expansion can be divided in two parts,

$$\Psi(r_1, \ldots, r_{N_e}) = \tag{7.1}$$
$$\sum_{i=1}^{N_{\text{eff}}} c_i \Phi_i(r_1, \ldots, r_{N_e}) + \sum_{i=N_{\text{eff}}+1}^{N_{\text{total}}} c_i \Phi_i(r_1, \ldots, r_{N_e}).$$

First summation goes over small number of terms which lie low on the energy scale and represent good approximation for the wave function. Second summation goes over large number of high-energy terms, however it represents only small correction to the wave function. In this case the off-diagonal matrix elements of the CI Hamiltonian between terms from second summation in (7.1) can be neglected and the problem of finding the wave function and corresponding energy is reduced to the matrix eigenvalue problem of the size N_{eff} with modified CI matrix

$$(H^{\text{CI}} - EI)X = 0, \tag{7.2}$$

where I is unit matrix, the vector $X = \{c_1, \ldots, c_{N_{\text{eff}}}\}$, and matrix elements of H^{CI} are modified to include contribution from high states (second summation in (7.1)):

$$\langle i|H^{\text{CI}}|j\rangle \rightarrow \langle i|H^{\text{CI}}|j\rangle + \sum_k \frac{\langle i|H^{\text{CI}}|k\rangle\langle k|H^{\text{CI}}|j\rangle}{E - E_k}. \tag{7.3}$$

Here $|i\rangle \equiv \Phi_i(r_1, \ldots, r_{N_e})$, $i, j \leq N_{\text{eff}}$, $N_{\text{eff}} < k \leq N_{\text{total}}$, $E_k = \langle k|H^{\text{CI}}|k\rangle$, and E is the energy of the state of interest. Since this energy is not known in advance, one has to perform iterations

$$\left(H^{\text{CI}}(E^{(i-1)}) - E^{(i)}I \right) X = 0, \tag{7.4}$$

where i is iteration number. To find initial approximation for the energy one can neglect the modification of the CI matrix (second term in (7.3)). When convergence is achieved, the solution of (7.2) is the exact solution of the full CI problem with off-diagonal matrix elements neglected between high states. In other words, neglecting these matrix elements is the only approximation assumed in the method.

For each level we calculate the Landé g-factor and compare it to the non-relativistic expression,

$$g = 1 + \frac{J(J+1) - L(L+1) + S(S+1)}{2J(J+1)}. \tag{7.5}$$

We treat angular momentum L and spin S as fitting parameters to fit the calculated values of the g-factors with the formula (8.1). This allows us to

use the LS notations for atomic states. Note however that the SHE states are highly relativistic and strongly mixed and the $LS-$ coupling scheme is very approximate.

The ionisation potential is obtained by calculating the energy of the ground state of the ion and taking the difference between ground states of the ion and the neutral atom. The same single-electron basis is used for the ion as for the neutral atom.

To calculate the spectra of oganesson we use a combination of the configuration interaction and perturbation theory (CIPT), introduced in ref. [167]. This technique has been used to calculate the spectra in open d-shell and open f-shell atoms with a large number of valence electrons where other many-body methods are unfeasible[167, 1, 237]. Calculations for W I, Ta I and Yb I are in good agreement with experiment. In this section we will give a brief overview of the CIPT method for Rn and Og. For an in depth discussion of the CIPT method refer to refs. [167].

We generate the set of complete orthogonal single-electron states for both Rn I and Og I by using the V^{N-1} approximation [238, 239] (where N is the total number of electrons). The Hartree-Fock (HF) calculations for atomic core are done for the open-shell configurations $6s^2 6p^5$ and $7s^2 7p^5$ for the Rn I and Og I respectively. The single-electron basis sets are calculated in the field of the frozen core using a B-spline technique with 40 B-spline states of order 9 in a box with radius 40 a_B (where a_B is the Bohr radius) with partial waves up to $l_{\max} = 4$ included [240].

The many-electron wavefunctions $|i\rangle = \Phi_i(r_1, \ldots, r_{N_e})$ are formed through single and double excitations from low-lying reference configurations. The many-electron wavefunctions are ordered by energy and divided into two sets. The first set represents a small number of low energy states which contribute greatly to the total CI valence wavefunction ($i < N_{\text{eff}}$, where N_{eff} is the number of included low energy states) and the remaining wavefunctions represent a large number of high energy terms which are small corrections to the valence wavefunction ($N_{\text{eff}} < i \leq N_{\text{total}}$). The valence wavefunction can be written as

$$|\Psi\rangle = \sum_{i=1}^{N_{\text{eff}}} c_i |i\rangle + \sum_{i=N_{\text{eff}}+1}^{N_{\text{total}}} c_i |i\rangle. \tag{7.6}$$

The off-diagonal matrix elements between the higher order states are neglected ($\langle i|H^{\text{CI}}|j\rangle = 0$ for $N_{\text{eff}} < i, j \leq N_{\text{total}}$) which greatly decreases the computation

time for a small sacrifice in accuracy. [1]

The matrix elements between high energy and low energy states are included pertubatively by modifying the low energy matrix elements,

$$\langle i|H^{\mathrm{CI}}|j\rangle \rightarrow \langle i|H^{\mathrm{CI}}|j\rangle + \sum_k \frac{\langle i|H^{\mathrm{CI}}|k\rangle\langle k|H^{\mathrm{CI}}|j\rangle}{E - E_k}, \qquad (7.7)$$

where $i, j \leq N_{\mathrm{eff}}$, $N_{\mathrm{eff}} < k \leq N_{\mathrm{total}}$, $E_k = \langle k|H^{\mathrm{CI}}|k\rangle$, and E is the energy of the state of interest. This results in a modified CI matrix and the energies are found through solving the standard eigenvalue problem,

$$(H^{\mathrm{CI}} - EI)X = 0, \qquad (7.8)$$

where I is unit matrix, the vector $X = \{c_1, \ldots, c_{N_{\mathrm{eff}}}\}$. The CI equations (7.8) are iterated in the CIPT method. For a detailed discussion of the CIPT precedure see Refs. [167, 1].

We included both Breit interaction[241, 242, 194] and QED radiative corrections in our calculation of the Og spectra. The Breit interaction V_B accounts for the magnetic interaction between two electrons and retardation. The QED corrections V_R accounts for the Ueling potential and electric and magnetic formfactors[243].

For the calculation of the even parity states of Og the low energy reference states in the effective matrix were $7s^2 7p^6$ and $7s^2 7p^5 8p$ while for the odd states $7s^2 7p^5 8s$ and $7s^2 7p^5 7d$. For the calculation of the ionisation potential and electron affinity we remove or add one electron from the states in the effective matrices respectively.

Each level is presented with an LS notation. These are selected by comparing calculated g-factors to the non-relativistic expression,

$$g_{NR} = 1 + \frac{J(J+1) - L(L+1) + S(S+1)}{2J(J+1)}. \qquad (7.9)$$

and using the L and S values as fitting parameters. We stress that the presented LS notations are approximations as the states of Og are highly relativistic and strongly mixed.

---

[1]It immediately follows from the perturbation theory that contributions of CI matrix elements between high states to low state energy are suppressed by a second power of large energy denominators while the contribution of matrix elements between high and low states are only suppressed by the first power in the denominator.

Chapter Eight

The CIPT method

8.1 CIPT Method

As mentioned above, an open $6d-$shell with more than three valence electrons makes established many-body methods too computationally expensive to be viable. This computational cost is reduced using a combination of configuration interaction (CI) and perturbation theory (PT) which was first introduced in [167] and used in [1, 230] for calculating the spectra of SHE Db ($Z = 105$) and Og ($Z = 118$). In this work we give a brief outline of the CIPT method and its implementation for the elements we calculate. For an in-depth discussion please refer to [167]. A fast version of this method has beed developed in [229].

To generate the single-electron wavefunctions for all the elements, we use the $V^{N_e - 1}$ approximation (where N_e is the total number of electrons) [238, 239] where the Hartree-Fock calculations are performed for the singly-charged open-shell atom with a $6d^n 7s$ configuration, where $n = 4, 5, 6$ and 7 for Sg, Bh, Hs and Mt respectively. The single-electron basis states are calculated in the field of the frozen atomic core. The basis sets are generated using a B-spline technique [240] with 40 B-spline states in each partial wave of order 9 in a box with radius 40 a_B (where a_B is the Bohr radius) with partial waves up to $l_{max} = 4$ (where l is orbital angular momentum) and the many-electron basis states $|i\rangle = \Phi_i(r_1, \ldots, r_{N_e})$ (where r_j is the radial position of the jth electron) for the CI calculations are formed by making all possible single and double excitations from reference low-lying non-relativistic configurations of the atom. This set of many-body electron wavefunctions is ordered from lowest to highest energy and divided into two sets,

Both the Breit interaction (magnetic interaction and retardation)[241, 242] and quantum electrodynamic (QED) radiative corrections (Ueling potential and

electric and magnetic form factors) [243] are included in the calculations as described in our earlier works (see, e.g. [225]). As both the Breit and QED radiative corrections scale with atomic charge, Z faster than the first power [225], their contribution to the energy levels of SHE is non-negligible. It was shown in [1] that the magnitude of the combined correction to the energy levels of Db is at most 200 cm^{-1}. A similar correction is expected for the SHE in this work.

For each level we calculate the Landé g-factor and compare it to the non-relativistic expression,

$$g_{\text{NR}} = 1 + \frac{J(J+1) - L(L+1) + S(S+1)}{2J(J+1)}. \tag{8.1}$$

Where possible, for each level we use g_{NR} to find an analogous state in the lighter element to obtain an approximate label in the LS coupling scheme. In fact, LS notations do not make sense for the highly relativistic SHE states due to very large spin-orbit interaction (so the eigenvectors will look strongly mixed in LS notation), we only use LS notations for comparison with lighter elements. Otherwise, we label the nth sequential state of total angular momentum J and parity by n_J^{parity}.

As discussed in the previous chapter, the development of more efficient methods to calculate the atomic properties of atoms with partially filled shells are needed. In this chapter I discuss the recently developed method which combines the configuration interaction method and perturbation theory (written as CIPT method). In Section **??** I outline the method used to calculate the single-electron atomic basis states using self-consistent Hartree-Fock method

8.2 Hartree-Fock Calculation of Basis States

All atomic calculations are performed *ab initio*. The Hamiltonian for a many-body electron atom is given by,

$$H(\mathbf{r}_1, \mathbf{r}_2, \mathbf{r}_3, \dots \mathbf{r}_N) = \sum_{i=1}^{N} h_0(\mathbf{r}_i) + \frac{1}{2} \sum_{i \neq j} \frac{1}{r_{ij}}. \tag{8.2}$$

The first term is the sum of single-electron relativistic Dirac Hamiltonians,

$$h_0(\mathbf{r}) = c\boldsymbol{\alpha} \cdot \mathbf{p} + \beta c^2 - \frac{Z}{r}.$$

To generate the single electron wavefunctions for both Ta I and Db I we use the V^{N-1} approximation (N is the total number of electrons) [238, 239]. The

Hartree-Fock (HF) calculations are performed for an open-shell atom with a valence s electron removed ($5d^36s$ and $6d^37s$ for Ta and Db respectively) where single-electron basis states are calculated in the field of the frozen core. We use a B-spline technique [240] with 40 B-spline states of order 9 in each partial wave in a box with radius 40 a_B with partial waves up to $l_{max} = 4$. Many-electron basis states for the CI calculations are formed by making all possible single and double excitations from reference low-lying configurations.

Finally we have the single-determinant many-electron basis states $|i\rangle = \Phi(r_1, r_2, ..., rN_e)$, where r_j is the radial position of the jth electron.

8.3   Configuration Interaction + Perturbation Theory

Having generated the many-electron basis states we can now establish the CI matrix and calculate the energy levels of the atom of interest. We construct a different matrix for states of differing parity and definite angular momentum J^π where $\pi = \pm$ (in this thesis we will refer to states having either even (+) or odd parity (−)). We populate each CI matrix with single and double excitations from designated low lying non-relativistic reference valence states ordered from smaller to largest energy. For example, to calculate the even parity states in Ta we use reference states $5d^36s^2$, $5d^46s^1$ and $5d^5$. This set of wavefunctions is then dived into two distinct sets, $\mathcal{P}$ and $\mathcal{Q}$. These two sets are,

- $\mathcal{P}$: A small set of low energy wavefunctions ($i \leq N_{\text{Eff}}$, where N_{Eff} is the number of wavefunctions in the low energy set) that give dominant contributions to the CI wavefunction.

- $\mathcal{Q}$: A large set of high energy wavefunctions ($N_{\text{Eff}} < i \leq N_{\text{total}}$) that are corrections to the wavefunctions from P.

Here N_{Eff} is the number of states in the effective CI matrix. Therefore, the total valence wavefunction is written as an expansion over single-determinant many-electron states $|i\rangle$,

$$|\Psi\rangle = \sum_{i=1}^{N_{\text{Eff}}} c_i |i\rangle + \sum_{i=N_{\text{Eff}}+1}^{N_{\text{total}}} c_i |i\rangle.$$

where c_i are coefficients of expansion. The CI matrix is then divided according to the matrix elements between the two sets as seen in Figure 8.1. The CI Hamiltonian is truncated by neglecting the off-diagonal matrix elements of the CI Hamiltonian between terms in $\mathcal{Q}$ ($\langle i|H^{\text{CI}}|j\rangle = 0$ for $|i\rangle, |j\rangle \in Q$), which
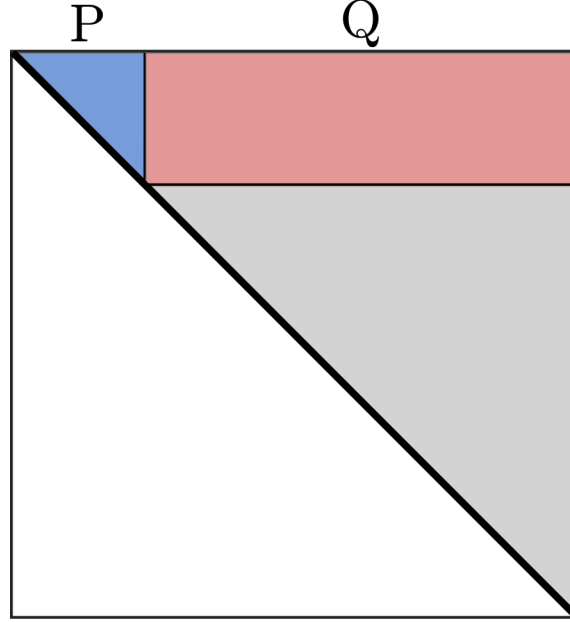
Figure 8.1: (First published in Ref. [?]). CIPT matrix structure which is both real and symmetric. The matrix is divided up into three sections for the CIPT calculation. The upper left corner (blue) represents the effective matrix consisting of matrix elements for between states only in set P. The upper middle and right section (red) consists of the matrix elements between states in sets P and Q to be treated perturbatively. The remaining off-diagonal grey matrix elements between states only in set Q are discarded.

reduces the problem of finding the wave function and corresponding energy to a matrix eigenvalue problem of the size N_{Eff} with modified CI matrix

$$(H^{\text{CI}} - EI)X = 0, \tag{8.3}$$

where I is unit matrix, the vector $X = \{c_1, \ldots, c_{N_{\text{eff}}}\}$ and the low energy matrix elements of H^{CI} are modified to include perturbative contributions between states in P and Q.

$$\langle i|H^{\text{CI}}|j\rangle \rightarrow \langle i|H^{\text{CI}}|j\rangle + \sum_k \frac{\langle i|H^{\text{CI}}|k\rangle\langle k|H^{\text{CI}}|j\rangle}{E - E_k}. \tag{8.4}$$

where $|i\rangle, |j\rangle \in \mathcal{P}$, $|k\rangle \in \mathcal{Q}$, $E_k = \langle k|H^{\text{CI}}|k\rangle$, and E is the energy of the state of interest.

8.4 Relativistic and Radiative effects

In this work we include the effects of both the Breit interaction [241, 242] and quantum electrodynamic (QED) radiative corrections (self-energy and vacuum polarisation corrections) [243] for completeness. The Breit interaction which accounts for the magnetic interaction and retardation is included in the zero momentum transfer approximation,

$$\hat{H}^B = -\frac{\boldsymbol{\alpha}_1 \cdot \boldsymbol{\alpha}_2 + (\boldsymbol{\alpha}_1 \cdot \mathbf{n})(\boldsymbol{\alpha}_2 \cdot \mathbf{n})}{2r} \tag{8.5}$$

where $\boldsymbol{\alpha}$ is the Dirac matrix, $\mathbf{r} = r\mathbf{n}$ and r is the distance between electrons denoted by subscripts 1 and 2. Similar to Coulomb interaction, Breit interaction (8.5) leads to Breit potential V_B which is added to the HF potential and included into the HF iterations.

The QED radiative corrections due to the Uehling potential V_U, and electric and magnetic form-factors V_E and V_g are included via a radiative potential V_R [243],

$$V_R(r) = V_U(r) + V_g(r) + V_E(r). \tag{8.6}$$

It is also included into the HF procedure. Note that iterating HF equations with Breit and QED potentials V_B and V_R formally lead to inclusion of non-linear contributions V_B^2, V_R^2, etc. which have no physical meaning. We have checks that corresponding contributions are small and cause no problem. On the other hand, iterating the HF equations with V_B and V_R takes into account an important relaxation effect [194] which is first order in V_B or V_R but all-order in Coulomb interaction. This relaxation effect reduces the size of the Breit or QED correction to the energy up to two times [194]. Both, Breit and QED corrections grow with Z faster than first power of Z, therefore it is important to check whether they give significant contributions to the energies of SHE. See section **??** for more discussion.

8.5 Estimation of the accuracy

Theoretical uncertainty is dominated by incomplete treatment of inter-electron correlations. These correlations can be further separated into core-valence and valence-valence correlations. We will discuss each of these separately. For the SHE calculations, the core includes all states in closed shells from $1s$ to $5f$ containing one hundred electrons occupying one hundred states. All other states, including states of the $6d$ and $7s$ shells are treated as valence states. Only

valence states are used in calculation of the CI matrix. This means that we neglect core-valence correlations. To estimate the corresponding uncertainties, we perform calculations of the energy levels of gold and roentgenium (Rg, $Z=111$). Both these elements have one external electron above a closed $5d$ or $6d$ shell. We perform the calculations using the correlation potential method [244, 245]. In this method, core-valence correlation corrections are obtained using the electron self-energy operator (correlation potential) Σ[1] calculated by summation of the diagrams in the many-body perturbation theory. The operator Σ is defined by the correlation correction to the energy of the valence electron on the orbital n, $\delta E_n = \langle n|\Sigma|n\rangle$. For the Au and Rg calculations, the upper complete d-shell ($5d$ or $6d$) is attributed to the core, and the correlation interaction of the external electron with the core is described by a correlation potential Σ.

Calculation of Σ involves a summation over all core states from $1s$ to $5d$ for Au or $6d$ for Rg. This summation is strongly dominated by the upper d-shell. E.g., the $5d$ shell gives about 90% of the correlation correction to the energies of the $6s$ and $6p$ valence states of Au, and more than 80% of the correlation correction to the energies of the $7s$ and $7p$ valence states of Rg (see Table 8.1). This is because of the small energy interval between the energies of the $5d$ (or $6d$) state and the energies of lowest valence states. Since correlation correction to the energy of the s and p valence states is about 20%, the effect of neglecting inner-core contributions to the core-valence correlations is about 1 to 2% of the energy of valence states.

It is interesting to note that in the second order of many-body perturbation theory, the correlation potentialΣ always overestimates the value of the correlation correction. This is because it does not include the effect of screening of inter-electron interaction by other atomic electrons. This effect appears in higher orders of perturbation theory. Its proper inclusion leads to very accurate results (see, e.g. [244, 248]).

Since in the present work we do not go beyond the second order, we have the fortunate situation where neglecting inner-core contributions to Σ has a similar affect on its value as the screening would do. In other words, the effect of neglecting the higher-order perturbative contributions on the calculated energies partially compensates the effect of neglecting screening of interelectron interactions. The data in Table 8.1 show that this is the case at least for the $6s$ state of Au (and probably for the $7s$ state of Rg) where the correlation correction is the largest in value. Therefore, it is reasonable to assume that the theoretical

---

[1]Do not confuse this with the QED self-energy operator which we included using the radiative potential method [243]. This is the many-body self-energy operator, which for example, has been defined in the textbook [246]. We calculate this operator using a Feynman diagram technique with relativistic Hartree-Fock Green's functions [244].

Table 8.1: Removal energies (cm^{-1}) for states of external electron of Au and Rg calculated in different approximations. RHF is relativistic Hartree-Fock, $\Sigma(nd)$ are Brueckner orbital energies calculated with correlation potential Σ, in which summation over core states is limited to $5d$ or $6d$ shell only. Σ(all) are the energies calculated with full summation over core states.

| | | Au | | |
	RHF	$\Sigma(5d)$	Σ(all)	Expt [247]
$6s_{1/2}$	60 179	75 539	77 878	74 409
$6p_{1/2}$	29 303	36 508	37 322	37 051
$6p_{3/2}$	26 664	32 314	32 785	33 324
$6d_{3/2}$	11 929	12 423	12 439	12 457
$6d_{5/2}$	11 875	12 344	12 357	12 376

| | | Rg | | |
	RHF	$\Sigma(6d)$	Σ(all)	
$7s_{1/2}$	83 436	101 901	106 780	
$7p_{1/2}$	38 006	49 996	52 269	
$7p_{3/2}$	26 550	33 659	34 685	
$7d_{3/2}$	11 859	12 594	12 656	
$7d_{5/2}$	11 738	12 383	12 428	

uncertainty is dominated by valence-valence correlations. The main source for it is the perturbative treatment of the excited configurations. The best way of estimating the uncertainty is to compare the theoretical and experimental energies for lighter elements. We did this in detail for W [167], which is the lighter analog of Sg, and for pairs Ta and Db [1], and Rn and Og [3]. As follows from this comparison and from the analysis in Sections 10.2.1, 10.2.2, the theoretical uncertainty for the energies is on the level of ~ 1000 cm^{-1}, sometimes a little higher (e.g. ~ 2000 cm^{-1} for odd states of Bh). The uncertainty for ionization potentials is on the level of a few percent (see section 10.3).

8.6 Comparison of CIPT calculations with experimental results in Ta

To demonstrate the accuracy of the CIPT method we compare the theoretical and experimental spectra of Ta I. As Ta lies in the same group but one period lower, we believe theoretical accuracy of the CIPT Ta spectrum would indicate the accuracy we can expect for Db. Electron states of neutral Ta have an open $5d$ shell, its ground state configuration is [Xe]$4f^{14}5d^36s^2$. As the $6s$ electrons are easily excited, we should treat the atom as a system with five external electrons. Note that a slightly more complicated atom, tungsten, which has

Table 8.2: Comparison of experimental (from ref.[247]) and CIPT spectra and ionisation potential of Ta I. The experimental excitation energies (E_E) and Landé g-factors (g_E) are compared to respective CIPT excitation energies (E_T) and Landé g-factors (g_T). The final column is the difference between experimental and theoretical excitation energies $\Delta = E_E - E_T$.

| | Configuration | State | J | Experimental | | CIPT | | |
				E_E (cm^{-1})	g_E	E_T (cm^{-1})	g_T	Δ (cm^{-1})
	Even states							
(1)	$5d^36s^2$	^{4}F	3/2	0.00	0.447	0.00	0.4373	
(2)	$5d^36s^2$	^{4}F	5/2	2 010	1.031	1 652	1.0336	358
(3)	$5d^36s^2$	^{4}F	7/2	3 964	1.218	3 175	1.2265	789
(4)	$5d^36s^2$	^{4}F	9/2	5 621	1.272	4 679	1.3066	942
(5)	$5d^36s^2$	^{4}P	1/2	6 049	2.454	6 017	2.4022	32
	Odd states							
(6)	$5d^36s6p$	^{6}G°	3/2	17 385		17 599	0.1719	-214
(7)	$5d^36s6p$	^{2}F°	5/2	17 994	0.732	18 225	0.7955	-231
(8)	$5d^26s^26p$	^{4}D°	1/2	18 505	0.172	18 629	0.0716	-124
(9)	$5d^36s6p$	^{6}G°	5/2	19 178	0.851	19 393	0.8551	-123
(10)	$5d^26s^26p$	^{4}D°	3/2	19 658	1.018	19 724	0.9389	-66
(11)	$5d^26s^26p$	^{2}S°	1/2	20 340	1.956	20 574	2.0278	-233
(12)	$5d^36s6p$	^{6}G°	7/2	20 560	1.194	20 463	1.1394	-97
(13)	$5d^26s^26p$	^{2}D°	3/2	20 772	0.812	20 796	0.8124	-24
(14)	$5d^26s^26p$	^{4}D°	5/2	21 168		21 358	1.2117	-190
(15)	$5d^36s6p$	^{4}F°	3/2	21 855	0.666	22 132	0.6773	-277
(16)	$5d^26s^26p$	^{2}D°	5/2	22 047	1.179	21 875	1.0838	172
(17)	$5d^26s^26p$	^{4}G°	7/2	22 381	1.060	22 276	1.0377	105
(18)	$5d^36s6p$	^{6}G°	9/2	22 682	1.231	22 285	1.2677	397
(19)	$5d^36s6p$	^{6}F°	1/2	23 355	-0.320	23 680	-0.2689	-325
(20)	$5d^36s6p$	^{4}F°	5/2	23 363	1.078	23 381	1.0766	-18
(21)	$5d^26s^26p$	^{4}D°	7/2	23 927	1.326	23572	1.3256	355
(22)	$5d^36s6p$	^{6}F°	3/2	24 243	1.126	24 463	1.1018	-220
(23)	$5d^36s6p$	^{6}D°	1/2	24 517	2.888	24 907	2.9261	-390
(24)	$5d^36s6p$	^{6}D°	3/2	24 739	1.620	25 143	1.6808	-404
(25)	$5d^36s6p$	^{4}F°	7/2	24 982	1.235	24 922	1.2590	60
(26)	$5d^36s6p$	^{6}G°	11/2	25 009	1.302	24 528	1.3366	481
(27)	$5d^36s6p$	^{6}F°	5/2	25 181	1.239	25 267	1.2573	-86
(28)	$5d^36s6p$	^{6}G°	9/2	25 186		24 733	1.2540	453
(29)	$5d^36s6p$	^{4}D°	1/2	25 513	0.028	25 697	0.0319	-184
(30)	$5d^36s6p$	^{4}F°	9/2	25 926	1.292	25 509	1.2970	417
(31)	$5d^26s^26p$	^{4}P°	5/2	26 220	1.338	26 298	1.2923	-78
(32)	$5d^36s6p$	^{4}D°	3/2	26 364	1.393	26 678	1.2676	-314
(33)	$5d^36s6p$	^{6}F°	7/2	26 586	1.356	26 299	1.315	287
(34)	$5d^26s^26p$	^{4}P°	3/2	26 590	1.576	26 759	1.6833	-169
(35)	$5d^36s6p$	^{6}D°	5/2	26 795	1.416	26 815	1.4086	-20
(36)	$5d^26s^26p$	^{4}P°	1/2	26 866	2.650	27 094	2.6189	-228
(37)	$5d^36s6p$	^{4}F°	7/2	26 960	1.223	26 787	1.2390	173
(38)	$5d^36s6p$	^{6}F°	9/2	27 733	1.390	27 279	1.3590	454
(39)	$5d^36s6p$	4D°	7/2	27 781	1.374	27 643	1.4658	138
(40)	$5d^36s6p$	^{6}G°	11/2	27 783	1.351	27 376	1.350	407
(41)	$5d^36s6p$	^{4}D°	5/2	28 134	1.394	28 337	1.3665	-203
(42)	$5d^36s6p$	^{4}G°	7/2	28 183	1.115	27 970	1.0421	213
(43)	$5d^36s6p$	^{2}P°	3/2	28 689	1.356	28 693	1.3052	-4
(44)	$5d^36s6p$	^{6}D°	9/2	28 767	1.337	28 414	1.4106	353
(45)	$5d^36s6p$	^{6}F°	5/2	28 862	1.247	28 868	1.2678	-6
(46)	$5d^36s6p$	^{6}D°	1/2	29 902	2.994	30 323	2.9971	-421

one more external electron, was already successfully studied using the CIPT method [167]. Therefore, we expect similar or better accuracy for Ta. For low lying even parity states of Ta we used the basis states of the $5d^36s^2$, $5d^46s$ and $5d^5$ configurations in the effective CI matrix. All other configurations, which were obtained by exciting one or two electrons from these configurations, were included perturbatively. Similarly for the odd parity states we used the states of the $5d^36s6p$, $5d^26s^26p$ configurations in the effective CI matrix, while other configurations are included perturbatively.

In Table 8.2 we present the comparison between experimental excitation energies and g-factors and those calculated by the CIPT method. We present a significant number of odd parity states to demonstrate the accuracy these states particularly towards the end of the optical region. This is because the most promising measurements are strong optical electric dipole (E1) transitions between the ground state and excited states of different parity. It is important to include as many of these transitions as possible. To identify the correct states for comparison with experiment we use the experimental and theoretical Landé g-factors. When experimental g-factors were not available we used the next sequential state in the theoretical calculations. There was excellent agreement between the experimental and CIPT g-factors with maximum difference between theory and experiment $\Delta g \approx 0.1$. This is sufficient accuracy for identification of the states.

There is good agreement between the experimental and theoretical excitation energies particularly for the low-lying odd parity states which are important for measuring the electric dipole transitions (see Section 9.2). For the odd parity states the largest discrepancy in energy was $\Delta = 453$ cm^{-1} with most states having $|\Delta| \approx 100 - 400$ cm^{-1}. The main source of the difference between theory and experiment is incomplete treatment of the correlations, which mostly comes from two factors. We neglect core valence correlations and off-diagonal matrix elements between highly excited states. This is the price we have to pay to be able to perform the calculations for a complicated system with five external electrons. There are some smaller factors, like cutting basis at $l_{max} = 4$, ignoring triple excitations, etc. For the CIPT calculations of the Db I spectrum we expect a similar accuracy as seen in Ta I due to the similar electronic structure.

Chapter Nine

Atomic structure study of superheavy element Db

The results of this chapter were published in Ref. [1]

Dubnium was first synthesized in 1968 and the current longest living isotope is ^{268}Db with a halflife of ≈ 30 hrs [249, 250]. This long lifetime relative to other SHEs makes future experiments promising. There is limited experimental and theoretical data for Db with the majority being chemical properties [249, 251]. An estimation of the ionisation potential has been performed for Db in [62] using a relativistic Hartree-Fock method with semi-empirical corrections introduced to simulate the effect of correlations.

9.1 Calculation of Excitation spectrum

For the CIPT calculations of Db I we use the same parameters as for the Ta I calculations in Section **??**. In the V^{N-1} approximation discussed in Section 11.1 we remove a $7s$ electron in the initial Hartree-Fock calculations and in the calculation of the single-electron basis states. The Db I ground state is [Rn]$5f^{14}6d^37s^2$ which is similar to Ta I with different principle quantum numbers. For calculation of the even parity states we populated the effective CI matrix with the states of the $6d^37s^2$, $6d^47s$ and $6d^5$ configurations. All higher states are obtained through single and double excitations of these states and are included perturbatively. Similarly for the states of odd parity the effective matrix contains states of the $6d^37s7p$, $6d^27s^27p$ and $6d^47p$ configurations. Other configurations are included perturbatively. For the ion we use the states of the $6d^37s$, $6d^27s^2$ and $6d^4$ configurations. Both Breit and radiative corrections are expected to be larger in SHE compared to lighter elements and therefore are in-
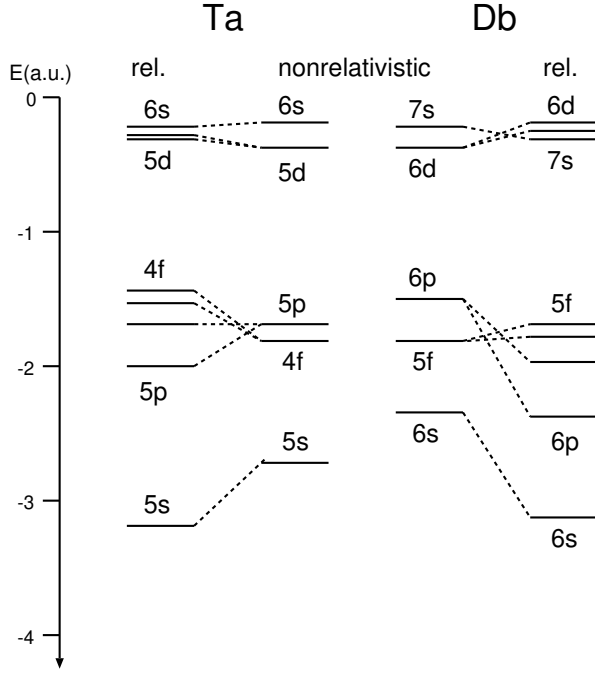
Figure 9.1: Hartree-Fock energies of upper core states of Ta and Db calculated in non-relativistic and relativistic approximations.

cluded in Table 9.1. In Table 9.1 we present the excitation energies of Db using the CIPT method. To demonstrate the affect of Breit and QED corrections we performed four separate calculations, first with no Breit or QED corrections, second with only Breit correction included, then with QED included but no Breit, and finally, with both corrections included (see Table 9.1).

Comparing the Db I spectrum in Table 9.1 to the Ta I spectrum in Table 8.2 we see there are some notable differences. While the order of even parity states has remained the same relative to each other, the order of the odd states has been significantly altered with the first $2F_{5/2}^{\circ}$ state being significantly lowered in the spectrum. Another thing to note is that the odd parity excitations are typically $6d \rightarrow 7p$ as opposed to the Ta excitation $6s \rightarrow 6p$. This can be explained by relativistic effects where the $7s$ electrons are more tightly bound than the $6d$ electrons in contrast to the $5d$ and $6s$ electrons in Ta [214]. These relativistic effects also cause the $6d$ electron to be ionised in Db instead of the $7s$ electron. This may result in significantly different chemical properties in Db compared to Ta.

To understand the difference between the atoms it is instructive to look at the Hartree-Fock energies and electron densities calculated in non-relativistic and

Table 9.1: Spectrum for the low lying energy levels of Db I and Db II using the CIPT method. Here E_{NC} are the excitation energies when neither Breit nor radiative corrections are included in the calculations, Δ_B and Δ_R are the changes in energy from E_{NC} when Breit and radiative corrections are included respectively. The final energy E is the excitation spectrum when both Breit and radiative corrections are included *ab initio*. The accuracy of these levels is expected to be similar to Ta I presented in Table 8.2. (Originally published in [1]).

| | Major Configuration | State | J | Excitation energy | | | | Landé g-factor |
				CIPT with no Breit or QED E_{NC} (cm^{-1})	Breit correction Δ_B (cm^{-1})	QED corrections Δ_R (cm^{-1})	Total E (cm^{-1})	
	Even States							
(1)	$6d^37s^2$	^{4}F	3/2	0	0	0	0	0.55
(2)	$6d^37s^2$	^{4}F	5/2	4 072	-77	21	4 016	1.04
(3)	$6d^37s^2$	^{2}F	7/2	6 595	-100	31	6 527	1.17
(4)	$6d^37s^2$	^{2}S	1/2	7 691	-73	16	7 634	2.05
(5)	$6d^37s^2$	^{4}G	9/2	8 076	-92	33	8 017	1.19
	Odd States							
(6)	$6d^27s^27p$	^{2}F°	5/2	6 255	213	123	6 591	0.73
(7)	$6d^27s^27p$	^{2}D°	3/2	11 240	156	87	11 483	0.63
(8)	$6d^27s^27p$	^{2}P°	1/2	12 642	140	84	12 869	1.30
(9)	$6d^27s^27p$	^{4}G°	7/2	13 645	116	147	13 909	1.02
(10)	$6d^27s^27p$	^{4}F°	5/2	13 873	113	132	14 117	1.06
(11)	$6d^27s^27p$	^{2}P°	1/2	14 516	96	88	14 705	0.99
(12)	$6d^27s^27p$	^{6}F°	3/2	14 572	105	96	14 772	1.11
(13)	$6d^27s^27p$	^{4}F°	5/2	17 493	78	76	17 647	1.11
(14)	$6d^27s^27p$	^{4}G°	9/2	18 596	80	144	18 820	1.14
(15)	$6d^37s7p$	^{2}D°	3/2	19 379	62	-3	19 438	0.70
(16)	$6d^27s^27p$	^{4}F°	7/2	20 462	53	134	20 649	1.20
(17)	$6d^27s^27p$	^{6}F°	3/2	21 706	56	50	21 811	1.07
(18)	$6d^27s^27p$	^{4}D°	1/2	22 123	72	93	22 284	0.07
(19)	$6d^27s^27p$	^{4}F°	5/2	22 204	35	54	22 292	1.11
(20)	$6d^27s^27p$	^{2}D°	3/2	23 003	39	22	23 067	0.69
(21)	$6d^27s^27p$	^{2}F°	7/2	23 221	37	133	23 390	1.10
(22)	$6d^37s7p$	^{4}F°	5/2	23 910	4	-2	23 913	0.94
(23)	$6d^27s^27p$	^{2}P°	3/2	24 622	2	119	24 743	1.37
(24)	$6d^27s^27p$	^{2}G°	9/2	24 915	27	133	25 074	1.11
(25)	$6d^37s7p$	^{2}F°	7/2	25 458	9	17	25 480	1.15
(26)	$6d^27s^27p$	^{4}F°	5/2	25 510	5	73	25 589	1.03
(27)	$6d^27s^27p$	^{2}F°	7/2	26 538	-4	78	26 612	1.17
(28)	$6d^27s^27p$	^{2}S°	1/2	27 435	-10	49	27 479	1.66
(29)	$6d^27s^27p$	^{2}F°	7/2	27 662	-23	24	27 666	1.12
(30)	$6d^27s^27p$	^{4}D°	3/2	27 589	-5	114	27 697	1.14
(31)	$6d^27s^27p$	^{4}G°	9/2	27 885	-13	118	27 990	1.17
(32)	$6d^27s^27p$	^{2}D°	5/2	28 162	-25	75	28 211	1.13
(33)	$6d^27s^27p$	^{4}P°	3/2	29 183	1	74	29 259	1.65
(34)	$6d^27s^27p$	^{4}G°	11/2	29 669	-45	103	29 669	1.25
(35)	$6d^37s7p$	^{6}G°	9/2	29 946	-75	-87	29 784	1.25
(36)	$6d^27s^27p$	^{6}F°	5/2	29 734	-25	174	29 821	1.34
(37)	$6d^37s7p$	^{4}D°	1/2	29 886	-24	-33	29 832	0.22
(38)	$6d^27s^27p$	^{2}F°	7/2	30 474	-29	97	30 541	1.16
	Db II states							
(39)	$6d^27s^2$	^{3}F	2	56 546	48	139	56 733	0.73
(40)	$6d^27s^2$	^{3}S	0	62 673	-13	119	62 778	0.00
(41)	$6d^27s^2$	^{3}F	3	62 952	-45	176	63 083	1.08
(42)	$6d^27s^2$	^{3}D	2	65 122	-62	120	65 179	1.25
(43)	$6d^27s^2$	^{3}P	1	65 587	-79	113	65 620	1.46

60

relativistic approximations. Fig. 9.1 shows energies of the upper core states of Ta and Db. The spectra are very similar. Relativistic energy shifts are larger for Db as expected and the most noticeable difference cause by this shift is the change of the order of the $6d$ and $7s$ states which leads to the change of the dominant configurations in low odd states of Db as discussed above. However, the absolute shift of the energies is small. It changes the order of the states because they are very close in the non-relativistic calculations. This change in the Hartree-Fock spectra caused by relativistic effects suggests that the differences in the spectra of neutral Ta and Db are mostly due to relativistic effects while correlation corrections are similar. This means that the accuracy of the calculations should also be similar for Ta and Db. This can be further illustrated by comparing the electron densities of the atoms calculated in non-relativistic and relativistic approximations (see Fig. 9.2). Examining the densities one can see the following: (a) There are four peaks for Ta and five for Db. They correspond to shells with principal quantum numbers from 1 to 4 for Ta and 1 to 5 for Db. Electrons in higher shells are distributed over larger distances and their density does not form a peak. (b) Relativistic effects pull inner electrons towards the nucleus but have little effect on outer electrons. (c) The densities at large distances $(r > a_B)$, where external electrons are located, are very similar. This is another indication that correlations are likely to be similar. To check this we performed another test. We compared the contribution of high energy states (second term in (7.3)) to the energies of Ta and Db. It turns out that the corrections to the energies of even states of Ta and Db differ by 2% only while corrections to the energies of odd states of Db about 30% larger than those of Ta. This means the uncertainty in the calculations for these states might also be larger for Db. Therefore, it seems to be reasonable to increase estimated uncertainty from ~ 400 cm^{-1} for Ta to ~ 500 cm^{-1} for Db.

From Table 9.1 we see that the effect of both the Breit interaction (Δ_B) and radiative corrections (Δ_R) is small and lies within the accuracy of our CIPT method. As it was discussed in previous section the main source of the uncertainty of the calculations comes from incomplete treatment of the correlations and it is < 500 cm^{-1} for Ta. It is expected to be similar for Db. On the other hand, the maximum value of the sum of Breit and QED corrections for Db is ~ 300 cm^{-1} while for most of the states it is < 200 cm^{-1} (see Table 9.1). It is interesting that the Breit and QED effects do not correlate with each other. This can be seen by summing the two corrections and the calculated energy with no corrections included (E_{NC}). This energy is very close to states in the spectrum which include both corrections simultaneously,

$$E \approx E_{NC} + \Delta_B + \Delta_R.$$

61
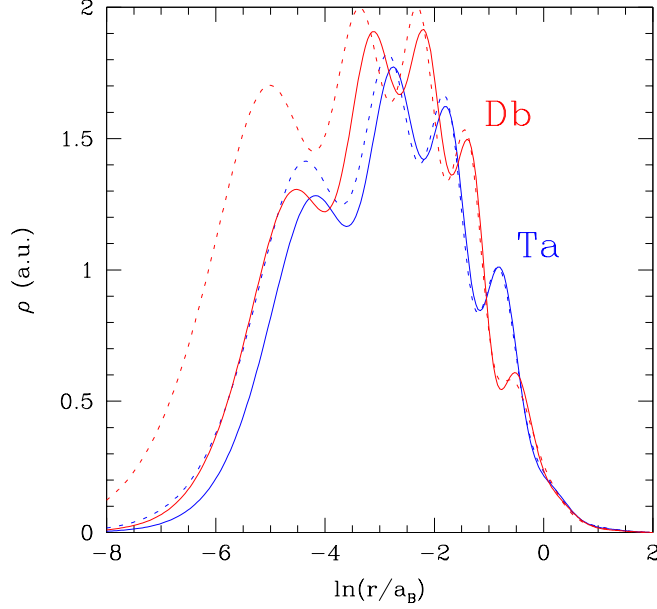
Figure 9.2: Electron density normalized to one ($\int \rho dV = 1$) of Db and Ta calculated in non-relativistic (solid line) and relativistic (dotted line) approximations.

Including both Breit and QED effects simultaneously will introduce new terms which are second order in perturbations of the interactions. Since both corrections are small these new terms will be negligible. To test the consistency of our method we calculated the spectrum of Db I using the V^{N-1} approach removing a $6d$ electron for the frozen core potential. In these calculations we obtained a similar spectrum within the accuracy of our calculations.

During completion of our work another paper on calculation of the Db spectrum appeared [252]. The calculations are done with a different implementation of a very similar method. The difference between the results of two papers seems to be larger than the uncertainty of our calculations. However, if we accept the difference between theory and experiment for Ta in [252] as an estimation of the uncertainty of their calculations, the results are consistent.

We are not aware of any other calculations of the Db spectrum apart from the calculations of IP. Our value 56744 cm^{-1} is in good agreement with the Hartree-Fock number 55000(7000) cm^{-1} [62] and coupled cluster number 55590 cm^{-1} [253]. Note that the IP of Db is significantly smaller than the IP of Ta (IP(Ta)=60891 cm^{-1}, see previous section) which is another indication of possible different chemical properties.

9.2   Electric dipole transitions and isotope shift

Due to the current low production rate of dubnium and other SHEs, broad spectroscopic scans are unfeasible for current experimental methods. Therefore experimental searches need to be assisted with theoretical predictions of the strongest lines specifically for optical electric dipole (E1) transitions. In this work we calculate and present the E1 transition amplitudes for the major optical transitions between the ground state and the lowest lying odd parity states for each Ta I and Db I. It should be noted that there is no published data for the E1 transitions for either Ta I or Db I and therefore we present the E1 transition amplitudes (A_{E1}) and transition probabilities (T_{E1}) for both atoms.

To calculate the E1 transition amplitudes A_{E1} we use the self-consistent random-phase approximation (RPA) to simulate the atom in an external electromagnetic field. This results in an effective electric dipole field for the electrons. The E1 transition amplitude for a transition between states a and b is given by $A_{E1} = \left\langle b||\hat{D} + \delta V||a \right\rangle$ where $|a>$ and $|b>$ are the many electron wavefunctions calculated in the CIPT method above, $\hat{D}$ is the electric dipole operator acting on external electrons, δV is the correction to the self-consistent Hartree-Fock potential of atomic core caused by photon electric field. For a more in depth discussion on this method refer to ref. [237].

The E1 transition rates are calculated using (in atomic units),

$$T_{E1} = \frac{4}{3} \left(\alpha\omega\right)^3 \frac{A_{E1}^2}{2J+1}$$

where J is the angular momentum of the odd parity state, α is the fine structure constant and ω is the frequency of the transitions in atomic units. All calculations obey the selection rules for E1 transitions, a change in parity and change in angular momenta $|\Delta J| \leq 1$. We present the E1 transitions for Ta I and Db I in Table 9.3.

For Db from Table 9.3 we see that the transition between the ground state and the odd parity state $^4\text{F}_{3/2} \rightarrow {}^4\text{D}^\circ_{1/2}$ with has the largest transition rate $T_{E1} = 59.7 \times 10^6 \text{ s}^{-1}$ with an energy difference 29 886 cm^{-1}. The rate of this transition is an order of magnitude lower than the recently measured transition in No [173] and calculated in [188, 202, 183] however the level is at a similar energy which may be promising for future experiments on Db. Other promising transitions from the ground state are to states (7), (17), (20), (22), (33) although the rate of these transition are an order of magnitude lower. Large E1 amplitudes can

Table 9.2: Allowed electric dipole transitions between the ground states of Ta I ($^4F_{3/2}$) and its low lying odd parity states. The numbers next to the states correspond to the numbered spectra in Tables 8.2. The transition amplitudes D_{E1} are in atomic units. (Originally published in [1])

	State	D_{E1} (a.u)	A_{E1} ($\times 10^6$ s^{-1})
		Ta I	
(6)	$^6G^\circ_{3/2}$	-0.270	0.194
(7)	$^2F^\circ_{5/2}$	0.214	0.090
(8)	$^4D^\circ_{1/2}$	-0.641	2.64
(9)	$^6G^\circ_{5/2}$	-0.434	0.449
(10)	$^4D^\circ_{3/2}$	0.149	0.0856
(11)	$^2S^\circ_{1/2}$	-0.107	0.0973
(13)	$^2D^\circ_{3/2}$	0.495	1.12
(14)	$^4D^\circ_{5/2}$	-0.200	0.128
(15)	$^4F^\circ_{3/2}$	-0.360	0.688
(16)	$^2D^\circ_{5/2}$	0.069	0.0160
(19)	$^6F^\circ_{1/2}$	0.019	0.00446
(20)	$^4F^\circ_{5/2}$	-0.094	0.0381
(22)	$^6F^\circ_{3/2}$	0.007	0.000412
(23)	$^6D^\circ_{1/2}$	-0.073	0.0795
(24)	$^6D^\circ_{3/2}$	-0.249	0.477
(27)	$^6F^\circ_{5/2}$	-0.356	0.683
(29)	$^4D^\circ_{1/2}$	0.282	1.34
(31)	$^4P^\circ_{5/2}$	0.202	0.248
(32)	$^4D^\circ_{3/2}$	0.405	1.53
(34)	$^4P^\circ_{3/2}$	-0.063	0.0377
(35)	$^6D^\circ_{5/2}$	0.338	0.741
(36)	$^4P^\circ_{1/2}$	-0.066	0.0859
(41)	$^6D^\circ_{5/2}$	-0.278	0.583
(43)	$^2P^\circ_{1/2}$	-0.295	1.04

probably found when configuration mixing allows for significant contribution of the $7p \to 7s$ transition as opposed to the $7p \to 6d$ transition. This is especially clear for the $^4F_{3/2} \to {}^4D^\circ_{1/2}$ transition considered above.

Finally, we calculate isotope shift for Db. Isotope shift is important since it helps to obtain information about nuclei of SHE when frequencies of the transitions are measured for several isotopes. It can also be used to predict the spectra of other isotopes, in particular the spectrum of the hypothetically stable neutron-rich isotopes with "magic" number of neutrons $N = 184$. This may help in search for such isotopes.

Table 9.3: Allowed electric dipole transitions and associated isotope shift parameters a and F between the ground state of Db I ($^4F_{3/2}$) and its low lying odd parity states. The numbers next to the states correspond to the numbered spectra in Table 9.1. The transition amplitudes D_{E1} are in atomic units. The isotope shift calculation was performed for ^{268}Db ($\langle r^2 \rangle_{268} = 36.770$ fm^2) and ^{289}Db ($\langle r^2 \rangle_{289} = 38.470$ fm^2). (Originally published in [1])

	State	D_{E1} (a.u)	A_{E1} ($\times 10^6$ s^{-1})	a (cm^{-1})	F (cm^{-1}/fm^2)	$\tilde{F}$ (cm^{-1})
(6)	$^2F^\circ_{5/2}$	0.631	0.0385	32.16	3.11	23.78
(7)	$^2D^\circ_{3/2}$	1.53	1.80	18.70	1.81	13.83
(8)	$^2P^\circ_{1/2}$	0.558	14.05	1.43	10.98	
(10)	$^4F^\circ_{5/2}$	-0.531	0.268	27.33	2.64	20.21
(11)	$^2P^\circ_{1/2}$	0.384	0.476	15.78	1.52	11.67
(12)	$^6F^\circ_{3/2}$	0.180	0.0527	14.93	1.44	11.04
(13)	$^4F^\circ_{5/2}$	-0.339	0.213	8.39	0.81	6.21
(15)	$^2D^\circ_{3/2}$	-0.343	0.437	-18.84	-1.82	-13.93
(17)	$^6F^\circ_{3/2}$	1.22	7.85	-0.33	-0.03	-0.24
(18)	$^4D^\circ_{1/2}$	0.0968	0.105	13.58	1.31	10.04
(19)	$^4F^\circ_{5/2}$	-0.163	0.0996	-1.54	-0.51	-1.14
(20)	$^2D^\circ_{3/2}$	0.784	3.83	-4.88	-0.47	-3.61
(22)	$^4F^\circ_{5/2}$	-1.01	4.70	-19.24	-1.86	-14.23
(23)	$^2P^\circ_{3/2}$	-0.150	0.173	16.75	1.62	12.38
(26)	$^4F^\circ_{5/2}$	-0.890	4.49	6.22	0.60	4.60
(28)	$^2S^\circ_{1/2}$	-0.570	6.83	-4.42	-0.43	-3.27
(30)	$^4D^\circ_{3/2}$	-0.114	0.139	16.04	1.55	11.86
(32)	$^2D^\circ_{5/2}$	0.228	0.393	3.31	0.32	2.45
(33)	$^4P^\circ_{3/2}$	-0.388	2.01	6.68	0.64	4.94
(36)	$^6F^\circ_{5/2}$	-0.0174	0.00270	14.86	1.44	10.99
(37)	$^4D^\circ_{1/2}$	1.49	59.7	-28.14	-2.72	-20.81

Isotope shift of SHE elements is strongly dominated by volume shift (also known as "field shift" in literature). We calculate it by varying nuclear radius in computer codes. We present results in two different forms. First is given by [254]

$$\delta \nu = E_2 - E_1 = a \left(A_2^{1/3} - A_1^{1/3} \right),$$

where A_1 and A_2 are atomic numbers for two isotopes ($A_2 > A_1$) and a is the parameter which comes from the calculations. This form is convenient for prediction of the spectra of heavier isotopes. It is motivated by the relativistic

dependence of the volume shift on the nuclear radius, R_N, which is proportional to $R_N^{2\gamma}$ where $\gamma = \sqrt{1-(Z\alpha)^2}$. For Db $R_N^{2\gamma} \approx R_N^{1.28}$ and using the large scale trend for nuclear radii $R_N \propto A^{1/3}$ the volume shift can be approximated by $\propto A^{1/3}$. This nuclear radius approximation is valid for large scale trends in A where nuclear shell fluctuations are suppressed [255, 254], this is applicable for our Db I calculations as A_1 and A_2 are not neighboring isotopes.

Another form for the isotope shift is the standard formula related the change of atomic frequency to the change of nuclear radius

$$\delta\nu = F\delta\left\langle r^2 \right\rangle.$$

This formula is convenient for extraction of the nuclear radius change from the isotope shift measurements. The values of the a and F parameters for strong electric dipole transitions of Db are presented in Table 9.3.

9.3 Discussion

Chapter Ten

Atomic Structure of super heavy elements Sg, Bh, Hs and Mt

The results of this chapter were published in Ref. [?] In this work we present the low-lying odd and even states of SHE $Z = 106\text{-}109$ including the allowed E1 transition amplitudes and rates from the ground state to odd parity states. We also calculate the ionization potential and isotope shift parameters for these elements.

The paper progresses as follows; in Section 11.1 we give a brief overview of the CIPT technique and how we implement it for the SHE. In Section 8.5 we discuss the accuracy of the calculations. In Section 10.1 we give a brief discussion on the calculation of E1 transitions and corresponding isotope shift parameters between synthesized and predicted meta-stable SHE. In sections 10.2.1, 10.2.2, 10.2.3 and 10.2.4 we discuss the results of the CIPT on Sg I, Bh I, Hs I and Mt I atoms respectively. For reference we present the low-lying spectrum for Sg I and Bh I in Table **??** and Hs I and Mt I in Table **??** and the E1 transitions and isotope shift parameters in Table **??**. In Section 10.3 we present the ionization potentials of the four elements and compare them with other calculations.

10.1 Electric dipole transitions and isotope shifts

In the spectroscopic measurements, the frequencies of strong electric dipole (E1) optical transitions ($\omega < 40000$ cm^{-1}) are likely to be measured first as it has been done for the $^1S_0 \rightarrow {}^1P_1^o$ transition in No ($Z = 102$) [173]. Broad spectrum scans for strong lines are unfeasible and therefore *a priori* estimates of both a transition frequency and its strength from theoretical calculations will

aid the experiments on SHE. Calculation of frequencies will be considered in section 10.2. In this work we also calculate the E1 transition amplitudes and rates for the major optical transitions between the ground state and the lowest states of opposite parity (odd states) for each of the four SHE of interest. To calculate the E1 transition amplitude D_{E1} between two states $|a\rangle$ and $|b\rangle$, we use a self-consistent random-phase approximation (RPA) to simulate the atom in an external electromagnetic field. This results in an effective dipole field for the electrons that includes direct and exchange core polarization. An in-depth discussion of this method can be found in Ref. [256, 237]. The results in the RPA approximation are gauge-invariant [256]. However, when you calculate correlation corrections beyond RPA, the length form of the E1 operator usually gives better results for low-frequency transitions. Indeed, the calculation of the correlation corrections can be made explicitly gauge-invariant in the case of one electron above closed shells [245, 257]. However, in the velocity form some correlation corrections are proportional to $1/\omega$ and become very large for small frequencies ω [245, 257]. This is the reason why we prefer to perform all calculations using the length form of the E1 operator.

Note that comparison of results in different gauges is not always a good test of accuracy. For example, in the RPA approximation and in the correlation potential approach described in Ref. [245, 257], velocity and length forms give exactly the same results though the error is still finite. Therefore, to estimate the accuracy of the calculations we use comparison with available experimental data (see Table 11.3).

The E1 transition rates, A_{E1}, are calculated using (in atomic units),

$$A_{E1} = \frac{4}{3} (\alpha\omega)^3 \frac{D_{E1}^2}{2J + 1} \qquad (10.1)$$

where J is the angular momentum of the upper state, α is the fine structure constant and ω is the frequency of the transitions in atomic units. All calculated amplitudes, D_{E1}, obey the selection rules for E1 transitions. The accuracy of these calculations cannot be tested directly due to the lack of experimental data on SHE and therefore we must rely on comparisons in lighter elements. Using the above method we calculated the E1 transition amplitudes and transition rates for the lighter analogs and compared them to available experimental data in Table 11.3. The accuracy for the E1 amplitudes is $\sim 50\%$ which is sufficient to identify the strongest transitions. The calculated rates are *ab initio* using the amplitudes and energies calculated in the CIPT method.

Table 10.1: Comparison of E1 transition amplitudes and rates between experimental and CIPT values for the lighter analogs of SHE, W I, Re I, Os I, and Ir I. Here D_{E1}, A_{E1} and gf are the transition amplitude, rate and oscillator strength respectively. The experimental E1 amplitudes were calculated using the experimental energies, transition rates from experimental sources and Eq. (10.1). To calculate oscillator strengths for comparison with Re I transitions from Ref. [258], we use the formula $gf = 3.062 \times 10^{-6} \omega D_{E1}^2$ where ω is in cm^{-1} and D_{E1} is in (a.u.).

State	Expt.			CIPT		
	E^a (cm^{-1})	D_{E1} (a.u.)	A_{E1} ($\times 10^6$ s^{-1})	E (cm^{-1})	D_{E1} (a.u.)	A_{E1} ($\times 10^6$ s^{-1})
			W I			
13°_1	39 183.19	2.09(9)	178(15)[b]	39 606	3.07	400
			Os I			
4°_4	32 684.61	2.00(7)	31.53(221)[c]	32 576	2.36	43
3°_4	30 591.45	0.96	5.8[d]	30 359	1.37	12
2°_5	30 279.95	1.40(5)	10.05(70) [c]	31 904	2.15	28
			Ir I			
$3^\circ_{11/2}$	39 940.37	1.72(22)	32(8)[e]	41 083	1.49	26
$^4F^\circ_{9/2}$	37 871.69	2.07(26)	47(12)[e]	39 227	1.52	28
$^4D^\circ_{7/2}$	37 515.32	1.73(22)	40(10)[e]	40 106	1.55	39
$^6G^\circ_{9/2}$	35 080.70	1.59(20)	22(6)[e]	36 703	2.72	74
$^6G^\circ_{11/2}$	34 180.46	1.45(7)	14.2(14)[e]	36 358	1.51	18
State	E^a (cm^{-1})	D_{E1} (a.u.)	gf	E (cm^{-1})	D_{E1} (a.u.)	gf
			Re I			
$^6P^\circ_{3/2}$	28 961.55	1.22(17)	0.132(36)[f]	29 303	1.80	0.29
$^6P^\circ_{7/2}$	28 889.72	2.26(27)	0.45(11)[f]	29 247	3.32	0.98
$^6P^\circ_{5/2}$	28 854.18	1.70(19)	0.254(56)[f]	29 505	2.51	0.57

[a] Ref. [247], [b] Ref. [259], [c] Ref. [260], [d] Ref. [261], [e] Ref. [262], [f] Ref. [258]

Along with the excitation spectrum and E1 transitions we also calculate the isotope shift (IS) for each transition.

The IS is the difference in the transition frequency between two different isotopes. The IS is important for at least two reasons. First, it can be used to find the difference in nuclear radius between two isotopes. Second, it can be used to predict the spectra of heavier, meta-stable neutron rich isotopes from the spectra of short-lived, neutron deficient isotopes created and measured in the laboratory. These predictions can be compared to astronomical data [254, 263, 264, 265] and could lead to the discovery of isotopes in the "island of stability" where it is expected that meta-stable, neutron-rich isotopes are created in cosmological events[266, 267, 268, 269]. The IS of SHE is strongly dominated by the volume shift (also known as "field shift" in literature [270]), while the mass shift is negligible. Using CIPT, we calculate the excitation spectrum of the each isotope by varying the nuclear radius in the HF procedure described in the previous section. In the zero approximation only $s_{1/2}$ and $p_{1/2}$ electron waves penetrate the nucleus and for these the dependence of IS on the nuclear radius R_N is $R_N^{2\gamma}$ where $\gamma = \sqrt{1 - (Z\alpha)^2}$ - see details in Ref. [271]. Higher waves undergo isotopic shifts due to change of the $s_{1/2}$ and $p_{1/2}$ wave functions and corresponding changes in the atomic Hartree-Fock potential - the core relaxation effect. Therefore, the dependence of the field IS on the nuclear radius in any atomic transition in multi-electron atoms is always $R_N^{2\gamma}$. Using the large-scale trend for nuclear radii $R_N \propto A^{1/3}$ the isotopic volume shift can be also approximated by $\delta\nu \propto A^{2\gamma/3}$ [254, 271] as nuclear shell fluctuations are suppressed [255]. The first form of the IS we present is given by

$$\delta\nu = E_2 - E_1 = a \left(A_2^{2\gamma/3} - A_1^{2\gamma/3} \right), \tag{10.2}$$

where A_1 and A_2 are atomic numbers for two isotopes $(A_2 > A_1)$, E_1 and E_2 are the excitation energy for A_1 and A_2 respectively and a is a parameter which should be calculated for each transition. This form of the IS is convenient for non-neighbouring isotopes and predicting the spectra of meta-stable isotopes because there is a significant difference in the values of A for isotopes synthesized in laboratory and hypothetical meta-stable isotopes $(\Delta A \sim 10)$. The $R_N \propto A^{1/3}$ trend is based on the constant nuclear density approximation due to finite range nuclear interactions. Variation of the nuclear shape and charge density may lead to significant deviations. Specific theoretical information about expected density distributions in SHE is presented in [272].

A more common form of isotope shift is the standard formula relating the

change of atomic frequency to the change of nuclear charge radius

$$\delta\nu = F\delta\left\langle r^2 \right\rangle,$$ (10.3)

where the square of the nuclear charge radius is calculated using the Fermi distribution for the nuclear density. This formula (neglecting the mass shift) is convenient for extraction of the nuclear charge radius change from isotope shift measurements of nearby isotopes. Lastly, we introduce a new form of the IS which should be valid for all isotopes. Using the RMS (root mean squared) nuclear radius, $R_{rms} = \sqrt{\langle r^2 \rangle}$, and $\delta\nu \propto \delta R_{rms}^{2\gamma}$ [271] we can write the equation,

$$\delta\nu = \tilde{F}\frac{R_{rms,A_2}^{2\gamma} - R_{rms,A_1}^{2\gamma}}{\text{fm}^{2\gamma}}$$ (10.4)

where $\tilde{F}$ is an IS parameter to be calculated for each transition.

10.2 Calculation of energy levels, E1 transition rates and isotope shift
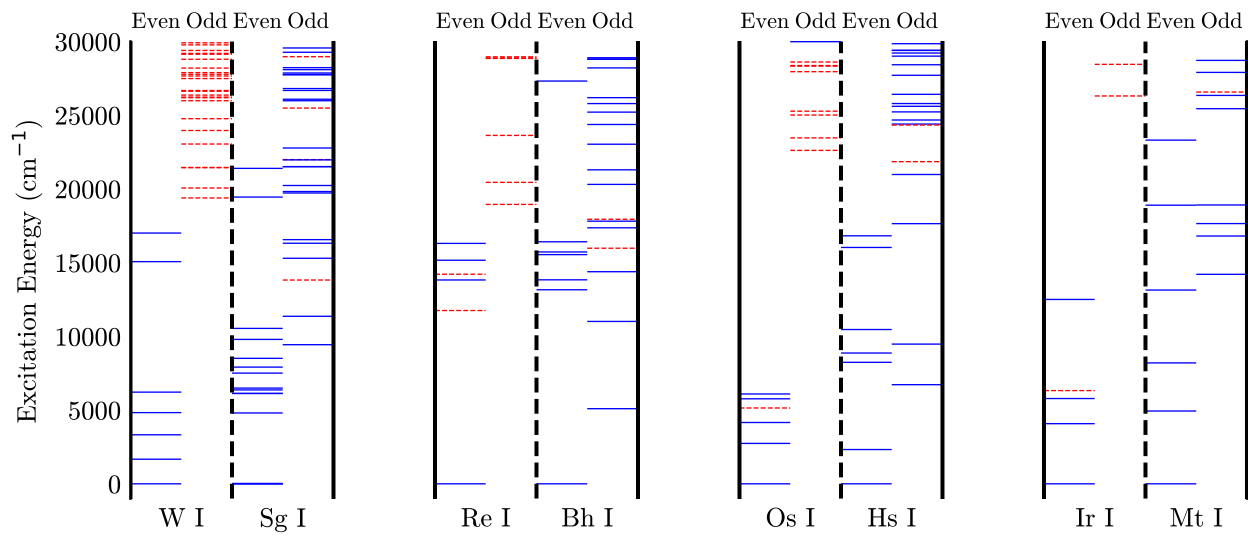
Figure 10.1: Comparison of low-energy excitations of SHE and their respective lighter analogs. For each element, the states are split between odd and even parities. The solid (blue) lines represent states with $6s^2$ or $7s^2$ in the electronic configuration for the lighter elements and SHE respectively. The dashed (red) lines are all other states where an s electron has been excited from the filled $6s$ or $7s$ shell. Experimental energies were used for W I, Bh I, Hs I and Ir I. [247]

Energy levels of SHE are calculated by solving the matrix eigenvalue problem (8.3) separately for states of given value of the total angular momentum J and parity. The specific details for each considered SHE are presented below. Most previous theoretical works on these SHE present the calculation of the first ionization potential, which we discuss in Section 10.3. Fig. 10.1 compares calculated spectra of low-lying states of SHE with experimental data on their lighter analogs. One can see a significant difference in the spectra of SHE and their lighter analogs, which is common for all considered atoms. Almost all low-lying odd states of lighter atoms correspond to the $6s - 6p$ excitation from the ground state. In contrast to that, in SHE the $7s$ state is significantly lower on the energy scale than the $6d$ state due to relativistic effects. Therefore, dominant excitations occur from the $6d$ state, i.e. low-lying odd states correspond to the $6d - 7p$ excitations from the ground state. Since the $6d - 7p$ energy interval is smaller than the $6s - 6p$ one, the density of odd states is higher for the SHE.

10.2.1 The Seaborgium Atom

Seaborgium was first experimentally detected in 1974 [273]. Since the initial discovery there has been continued interest and study into its physical and chemical properties including the discovery of isotopes with longer lifetimes. There exist some experimental results for Sg I in the field of chemistry [249]. However, there are no spectroscopic results available. The ground state configuration of Sg I is expected to be $[\mathrm{Rn}]5f^{14}6d^47s^2$, similar to the ground state of its lighter homologue (W I, ground configuration: $[\mathrm{Xe}]4f^{14}5d^46s^2$).

We calculated the first 6 even parity states and the ground state was found to be the $[\mathrm{Rn}]5f^{14}6d^47s^2\ ^5\mathrm{D}_0$ state. To calculate the even states we use three reference configurations, $6d^47s^2$, $6d^57s$ and $6d^6$ to make states in the effective CI matrix (first terms in the expansion (??) and in the CI effective Hamiltonian (8.4)). All other states, which are treated as corrections to the states from reference configurations (second terms in the expansion (??) and in the CI Hamiltonian (8.4)) are obtained by exciting one or two electrons from the reference configurations. Similarly, for odd parity states we use the reference states from the $6d^47s7p$, $6d^37s^27p$ and $6d^57p$ configurations. All calculated even and odd energy levels are presented in Table ??. Similar calculations were performed for W I using analogous reference states and the same parameters. Comparing these results to the experimental spectrum [247] we found a maximum discrepancy of $|\Delta| \approx 600$ cm^{-1} and expect a similar accuracy for our Sg I calculations. Note that this accuracy is slightly better than what was reported in Ref. [167] due to inclusion of a larger number of states into the effective CI matrix.

Comparing the spectrum of Sg I in Table **??** to the spectrum of W I [247], we can see the manifestation of relativistic effects. As discussed above, relativistic effects cause the $7s$ orbital in Sg I to be strongly contracted and more tightly bound in comparison to the $6s$ orbital in W I. The same effects also push out the $6d$ orbital of Sg I in comparison to the $5d$ orbital in W I. In the W I spectrum there are low-lying states corresponding to the $6s \rightarrow 5d$ excitation from the ground state (e.g., the $5d^5 6s$ $^7S_3$ state at 2 951.29 cm^{-1}). In contrast, in the Sg I spectrum, all low-lying even states belong to the $6d^4 7s^2$ configuration. The relativistic effects are more apparent in the low-lying odd parity states of Sg I. In W I all odd states correspond to the $6s \rightarrow 6p$ excitation from the ground state, while in Sg I most of the low-lying odd states correspond to the $6d \rightarrow 7p$ excitation. Only a few of the Sg I predicted in the optical region correspond to the $7s \rightarrow 7p$ excitation.

We calculate rates of electric dipole transitions from the ground state to excited states of the opposite parity using the approach described in Section 10.1. The results are presented in Table **??**. There are not many such transitions due to the zero value of the total angular momentum J in the ground state. Because of that, the transitions are only allowed to the odd states with $J = 1$. A few transitions are good candidates for the detection. The transition with the highest transition rate is $^5D_0 \rightarrow 9^\circ_1$ ($\omega = 40\ 073$ cm^{-1}).

We also present the isotopic shift parameters, F and a from equations (10.2) and (10.3), in Table **??** for each respective E1 transition. The two isotopes we use are ^{269}Sg and ^{290}Sg ($R_{rms,269} = 5.8814$ fm and $R_{rms,290} = 6.0145$ fm respectively), where ^{290}Sg is the theoretically metastable ($N = 184$) isotope of Sg.

10.2.2 The Bohrium Atom

Bohrium was first discovered in 1981 [274]. No atomic spectra have been measured or calculated for any Bh isotopes or ions. When calculating the energy spectrum of Bh I, we use a similar approach as with Sg I. For the low-lying even parity spectrum we use an effective CI matrix build from the states of the $6d^5 7s^2$, $6d^6 7s$ and $6d^7$ reference configurations. For the odd parity spectrum we use the states from the $6d^5 7s 7p$, $6d^4 7s^2 7p$ and $7d^6 7p$ reference configurations. The lowest six even parity states and low-lying odd parity states are presented in Table **??**. For an estimate of accuracy we calculated the low-lying spectrum of Re I (the lighter analogue of Bh) with similar parameters. Comparing the CIPT calculated spectrum to the experimental spectrum [247], the energy discrepancy (with respect to the ground state) was $\Delta \approx 900$ cm^{-1} for the even parity states, while for the odd parity states $\Delta \approx 2000$ cm^{-1}.

The calculated Bh I ground state is $6d^5 7s^2$ $^6S_{5/2}$. As with Sg I, we see the relativistic effect of the tightly bound $7s$ electron which results in the primary excitation of the $6d$ electron. Comparing the spectrum of Bh I with that of Re I in Fig. 10.1 we see that there are several low-lying states in Re I corresponding to $6s \to 5d$ excitations (the lowest is at 11754.52 cm^{-1}), while there are no similar low-lying states in Bh I. The density of low-energy odd-parity states is much larger in Bh I than in Re I. The Bh I low odd-parity states are completely dominated by the $6d \to 7p$ excitations in calculated spectrum and and there are no $7s \to 7p$ excitations. The odd-parity state comparison between Bh I and Re I is similar to that of Sg I and W I in Section 10.2.1. In the spectrum of Re I [247] there do exist states corresponding to $5d \to 6p$ transitions from the ground state; however, they occur much higher in the spectrum compared to Bh I where the $6d \to 7p$ excitations dominate. It should be noted that the number of low-lying odd-parity states is larger in Bh I than in Re I. The lowest odd state of Bh I occurs at 12792 cm^{-1}, whereas in Re I the lowest odd state is at 18950 cm^{-1}.

Bh I has a large number of allowed low-energy optical E1 transitions from the ground state, which are presented in Table **??**. The isotope shift parameters, a and F, are calculated using formulas (10.2) and (10.3) after calculating the atomic spectra for the theoretically meta-stable isotope of ^{270}Bh using the CIPT method. We use the values of RMS nuclear radii $R_{rms,270} = 5.8879$ fm for ^{291}Bh and $R_{rms,291} = 6.0207$ fm for ^{291}Bh.

10.2.3 The Hassium atom

Hassnium ($Z = 108$) was first synthesized in 1984 [275]. We present the low-lying levels and the first ionization energy of Hs I in Table **??**. For the low-lying even spectrum effective CI reference states belong to the $6d^5 7s^2$, $6d^6 7s$ and $6d^7$ configurations. For the odd spectrum we use reference states of the $6d^5 7s 7p$, $6d^4 7s^2 7p$ and $7d^6 7p$ configurations. Note that the half-filled $6d$ sub-shell makes computational methods particularly expensive. However, using the CIPT method the computation becomes tractable.

Once again it is interesting to compare the spectra of Hs I with the analogue Os I in the period above. In the even states of Os I there are states corresponding to the $6s \to 5d$ excitations from the ground state. In the Hs I spectrum all low-lying even states belong to the $6d^5 7s^2$ configuration. No states with the $7s \to 6d$ excitation were found. The odd states are similar to those of Sg and Bh, with the primary excitation $6d \to 7p$ in Hs I while there are no $5d \to 6s$ excitations

in low Os I spectrum. The odd states of Hs I also lie much lower than those in Os I. The lowest odd state of Hs I is 13 949 cm^{-1}, while the first odd state of Os I occurs at 22 615.69 cm^{-1} [247].

The allowed strong optical E1 transitions from the low-lying odd states to the ground state (^{5}D$_4$) are presented in Table **??**. As with Bh I there is a large number of strong optical transitions. The transition with the largest rate is 3°_5 $\rightarrow$ ^{5}D$_4$ ($\omega = 39\ 268$ cm^{-1}). Other possibly detectable transitions include $5^{\circ}_3 \rightarrow$ ^{5}D$_4$ ($\omega = 34\ 812$ cm^{-1}) and $2^{\circ}_5 \rightarrow$ ^{5}D$_4$ ($\omega = 34\ 739$ cm^{-1}).

We also present the isotopic shift parameters for the Hs E1 optical transitions in Table **??**. These were calculated from the theoretical spectra (calculated with the CIPT method) with isotopes ^{270}Hs and ^{292}Hs with RMS nuclear radii $R_{rms,270} = 5.8879$ fm for ^{292}Hs and $R_{rms,292} = 6.0207$ fm for ^{270}Hs.

10.2.4 The Meitnerium Atom

Meitnerium ($Z = 109$) was first synthesized in 1982 [276]. The ground state of Mt I is expected to follow that of the element in the above period (Ir) with [Rn]$5f^{14}6d^77s^2$ ^{4}F$_{9/2}$ which we confirm in the calculated spectrum presented in Table **??**.

We use the same method as for previous elements to calculate the low-lying spectrum of Mt I. We present the lowest six even states using the $6d^77s^2$, $6d^8$, $7s$ and $6d^9$ reference configurations. We also present the first 12 odd parity states for which the $6d^77s7p$, $6d^67s^27p$ and $6d^87p$ configurations were used. The results are in Table **??**. Comparison with lighter analog Ir I shows similar trend as for other SHE Sg, Bh and Hs.

We also present the allowed E1 transitions for Mt and the respective isotope shift parameters in Table **??**. The high energy of the odd states in Mt I result in a small number of allowed E1 transitions within optical region from the ground state compared to Bh and Hs. Promising transitions for future measurement include ^{6}F$^{\circ}_{11/2}$ $\rightarrow^4$F$_{9/2}$ ($\omega = 38\ 027$ cm^{-1}) and ^{6}D$^{\circ}_{9/2}$ $\rightarrow^4$F$_{9/2}$ ($\omega = 33\ 505$ cm^{-1}). All other rates are two or more orders of magnitude smaller. For the synthesized and metastable isotopes we use the RMS nuclear radii values, $R_{rms,276} = 5.9265$ fm and $R_{rms,293} = 6.0330$ fm.

10.3 Ionization potentials and comparison with other data.

As well as calculating the spectrum of neutral Sg, Bh, Hs and Mt we also calculated their first ionization potentials (IPs). To calculate the IP for each

atom we use the same single-electron basis set for a neutral atom and an ion. The ionization potential is found as a difference between ground state energies of the atom and its ion. The effective CI matrix was built from all states of the $6d^n 7s$, $6d^{n-1} 7s^2$ and $6d^{n+1}$ reference configurations ($n = 4 - 7$ for Sg through to Mt). States that were treated perturbatively were obtained by exciting one or two electrons from the reference configurations and generating all single-determinant states from these configurations. We start from calculating the IPs of lighter analogs of the SHE to compare them with experiment. The results are in Table 10.10. We also include in the table the results of the multi-configuration Dirac-Fock (MCDF) calculation [277, 278]. We do this because similar MCDF calculations have been used for the SHE (see Tables 10.11 and 10.12). The CIPT values of the IPs agree with experiment within few percent (error <1% for Ta, W, and Re, and $\sim 3\%$ for Os and Ir). We expect similar accuracy for the first IPs of SHE analogs presented in Table 10.12. For comparison, the difference between MCDF values of IPs of W, Re and Os and experimental IPs is larger than 10% (Table 10.10).

Table 10.11 shows some resonance (corresponding to strong electric dipole transitions from the ground state) excitation energies for SHE and their lighter analogs calculated in the present work and by the MCDF method [277, 278]. The energies for lighter elements are compared to experiment. Our values are taken from Tables **??** and **??**; for the MCDF energies we present all results which can be found in [277, 278]. There is a significant difference in the excitation energies of SHE, while for lighter atoms the difference is not so large. There is a $\sim 10\%$ difference from experiment in both calculations. There are too little data on the MCDF calculations to come to any conclusion about the reasons for the differences.

Finally, Table 10.12 shows IPs of SHE and their ions. We included the result of our previous work on Db [1] together with the relativistic Hartree-Fock (RHF) calculations which include semi empirical core-polarisation correction [62] and the MCDF results [277, 278]. There are two sets of MCDF results. One, in the column marked as MCDF, is what directly comes from the MCDF calculations. We also presented prediction of MCDF IPs corrected by extrapolation of the difference with experiment from lighter atoms (marked as "Extrap."). As one can see from Table 10.10 the MCDF method tends to underestimate IPs by about 10%. Therefore, multiplying the calculated IPs by a factor ~ 1.1 extrapolated from lighter elements leads to better prediction of the IPs for SHE. Indeed, the extrapolated values are in better agreement with our CIPT calculations. Note however that the extrapolation assumes similarities between involved elements. In fact, they are significantly different. Ionization of lighter elements goes via removal of the s electron ($6s$ electron for W, Re and Os). In contrast, ionization

of SHE goes via removal of the $6d$ electron. RHF calculations (see Ref. [62] and Table 10.12) used a different type of extrapolation. Instead of extrapolating a final number, a term in the Hamiltonian was extrapolated. A term, simulating the effect of core polarisation, was added to the RHF Hamiltonian in Ref. [62]. Its strength was chosen to fit IPs of lighter atoms. Then the same term was used for SHE.

Studying IPs of SHE with open $6d$-shell shows a significant difference in trends compared to their lighter analogs. These differences are convenient to discuss by looking at the diagram in Fig. 10.2. The diagram shows trends in IPs of SHE with open $6d$-shell from Db to Mt together with the trends for lighter atoms from Ta to Ir. IPs for doubly ionized ions of lighter elements are also shown because they do not have external s-electrons, and further ionization of these ions goes via removal of a d-electron similar to what takes place for SHE.

First, we note that the change of IPs from Ta to Ir is smooth and almost monotonic, apart from a small local minimum at Re atom. It shows increasing of IP towards the fully filled $5d$ shell. The ionization occurs via removal of a $6s$ electron. The $6s$ orbital is not very sensitive to the details of energy structure of other shells, which explains the smooth behaviour of the IP trend. In contrast, ionization of the SHE occurs via removal of a $6d$ electron. Strong relativistic effects manifest themselves in the trend of the IP change. A local maximum of the IP occurs for Sg atom that has four $6d$ electrons in the fully occupied $6d_{3/2}^4$ subshell. Removing an electron from a closed shell is difficult, therefore there is a local maximum. The next atom, Bh, has one more $6d$ electron, which has to occupy the $6d_{5/2}$ state. Due to large relativistic effects in SHE, there is a large fine structure interval between the $6d_{3/2}$ and $6d_{5/2}$ states and therefore a significantly smaller IP for Bh (see Fig. 10.2 and Table 10.12). A similar effect is known for an open p shell where it is more pronounced. E.g., the IP of Bi, which has three $6p$ electrons, is smaller than for Pb, which has two $6p$ electrons corresponding to the closed $6p_{1/2}^2$ subshell. The effect is much more pronounced for SHE with an open $7p$ shell [225]. The IP of Mc (Z=115), which has three $7p$ electrons, is about 1.5 times smaller than the IP of Fl (Z=114), which has two $7p$ electrons.

To see whether a similar effect can be found in lighter atoms, we studied IPs of doubly ionized ions with an open d-shell (from $3d$ to $5d$). The ions were chosen because they do not have external s-electrons, and further ionization goes via removal of a d-electron. The results are shown in Fig. 10.2. Most IP values are taken from the NIST database [247]. However, NIST data for ions from Ta III to Ir III have poor accuracy. Therefore, we recalculated the IPs using the CIPT method. IPs of these ions show a different trend compared to the SHE. The maximum binding energy and hence the maximum IP is for a half

filled d-shell in agreement with the non-relativistic Hund rule, which states that the maximum energy corresponds to the maximum possible value of the total spin. This holds even for the heaviest of the three groups of ions. Thus, the SHE elements with the open $6d$ shell represents the only known example of a strong manifestation of relativistic effects, making the energy difference between the $6d_{3/2}$ and $6d_{5/2}$ states more important than Hund's rule.

A similar manifestation of relativistic effects can be found in the trends of further ionization of the SHE ions (see Table 10.12). In many cases (e.g., the Bh and Hs ions) ionization from the $6d$ shell stops as soon as the fully filled $6d_{3/2}^4$ subshell is reached. Further ionization occurs from the $7s$ subshell.

10.4   Conclusion

Calculation of atomic spectra and optical E1 transitions for the elements in the superheavy region with open d-shells is novel. In spite of the extreme computational cost of existing methods, using perturbation theory we can calculate the low-lying energy states and relevant E1 transitions with a modest computational cost and with a small loss in accuracy [167]. In this work we presented the low-lying energy states for Sg I, Bh I, Hs I and Mt I including the optical transitions between the ground state and states of the opposite parity and their ionization potentials. For all SHEs we observed the relativistic effects, which contract the spectrum compared to their lighter analogs. This is advantageous as it results in a large number of states in the allowed E1 optical region and therefore enhances the likelihood of future measurements. These calculations will help to facilitate future experimental measurements of atomic spectra of these elements. We also presented the relevant isotopic field shift for optical E1 transitions for all four considered SHE. This may help the interpretation of future measurements and contribute to our understanding of the nuclear properties of elements in the superheavy region and potentially identify the existence of meta-stable superheavy isotopes in astronomical spectra.
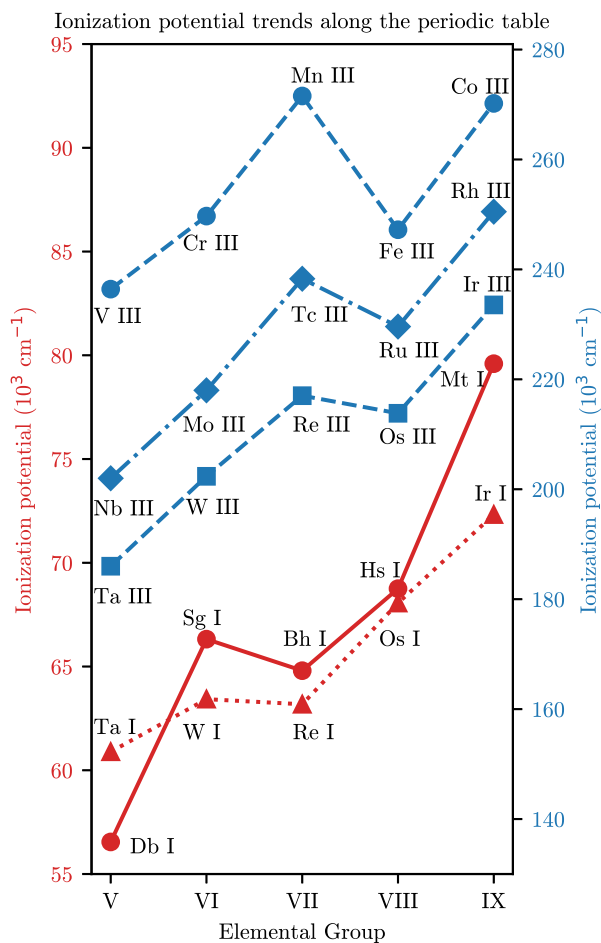
Figure 10.2: Plot of ionization trends for open *d*-shell elements. The IP trend lines for the doubly ionized elements (blue) use the scale on the right and the neutral IP trend lines (red) use the left. The IPs of neutral SHEs and the doubly ionized lighter homologues Ta III, W III, Re III, Os III and Ir III were calculated using the CIPT method. All other IPs are from Ref. [247].

Table 10.2: Low-energy spectrum of even- and odd-parity states in Bh I. We present the energy and Landé g-factor for each state J^{parity}. We present LS-notations only for comparison with lighter analogs. For SHE states where an analogous state cannot be found in the lighter analog the term is labeled according to the sequential number of the state (n) for the given J^{parity} group, n_J^{parity}.

	Bh I			
	Major Configuration	Term	Energy (cm^{-1})	Landé g-factor
	Even parity states			
(1)	$6d^57s^2$	$^6S_{5/2}$	0	1.78
(2)	$6d^57s^2$	$^4P_{3/2}$	13 062	1.32
(3)	$6d^57s^2$	$^4G_{7/2}$	13 828	1.15
(4)	$6d^57s^2$	$^4G_{11/2}$	14 981	1.19
(5)	$6d^57s^2$	$^4P_{1/2}$	15 659	1.90
(6)	$6d^57s^2$	$^4G_{9/2}$	16 447	1.17
	Odd parity states			
(7)	$6d^47s^27p$	$^2S^\circ_{1/2}$	12 792	0.72
(8)	$6d^47s^27p$	$^6D^\circ_{1/2}$	17 781	1.66
(9)	$6d^47s^27p$	$^6D^\circ_{3/2}$	19 483	1.09
(10)	$6d^57s7p$	$^8P^\circ_{5/2}$	22 228	2.08
(11)	$6d^47s^27p$	$^6P^\circ_{3/2}$	22 533	1.74
(12)	$6d^47s^27p$	$^6D^\circ_{5/2}$	22 930	1.26
(13)	$6d^57s7p$	$^8P^\circ_{7/2}$	24 020	1.67
(14)	$6d^47s^27p$	$^6D^\circ_{7/2}$	25 171	1.28
(15)	$6d^47s^27p$	$^6D^\circ_{9/2}$	26 587	1.21
(16)	$6d^47s^27p$	$^6F^\circ_{5/2}$	28 060	1.57
(17)	$6d^47s^27p$	$3^\circ_{1/2}$	29 823	0.44
(18)	$6d^47s^27p$	$3^\circ_{3/2}$	29 885	1.55
(19)	$6d^47s^27p$	$3^\circ_{7/2}$	31 078	1.24
(20)	$6d^47s^27p$	$4^\circ_{5/2}$	31 253	1.30
(21)	$6d^47s^27p$	$4^\circ_{7/2}$	32 814	1.37
(22)	$6d^47s^27p$	$4^\circ_{3/2}$	33 459	1.40
(23)	$6d^47s^27p$	$2^\circ_{9/2}$	33 575	1.06
(24)	$6d^47s^27p$	$5^\circ_{5/2}$	33 738	1.04
(25)	$6d^47s^27p$	$4^\circ_{1/2}$	35 408	2.22
(26)	$6d^47s^27p$	$5^\circ_{3/2}$	35 447	1.00
(27)	$6d^47s^27p$	$6^\circ_{5/2}$	35 774	1.34
(28)	$6d^47s^27p$	$5^\circ_{7/2}$	36 251	1.00
(29)	$6d^47s^27p$	$6^\circ_{3/2}$	36 333	1.02
(30)	$6d^47s^27p$	$7^\circ_{5/2}$	36 875	1.25
(31)	$6d^47s^27p$	$1^\circ_{11/2}$	37 542	1.10
(32)	$6d^47s^27p$	$6^\circ_{7/2}$	37 910	1.32
(33)	$6d^47s^27p$	$7^\circ_{3/2}$	37 954	1.05
(34)	$6d^57s7p$	$^8P^\circ_{9/2}$	37 972	1.62
(35)	$6d^47s^27p$	$4^\circ_{9/2}$	38 336	1.23
(36)	$6d^47s^27p$	$8^\circ_{5/2}$	39 454	1.19
(37)	$6d^47s^27p$	$7^\circ_{7/2}$	39 602	1.33
(38)	$6d^47s^27p$	$5^\circ_{1/2}$	40 273	1.76

Table 10.3: Low-energy spectrum of even- and odd-parity states in Sg I. We present the energy and Landé g-factor for each state J^{parity}. We present LS-notations only for comparison with lighter analogs. For SHE states where an analogous state cannot be found in the lighter analog the term is labeled according to the sequential number of the state (n) for the given J^{parity} group, n_J^{parity}.

	Major Configuration	Term	Energy (cm^{-1})	Landé g-factor
		Sg I		
		Even parity states		
(1)	$6d^4 7s^2$	$^5\mathrm{D}_0$	0	0.00
(2)	$6d^4 7s^2$	$^5\mathrm{D}_1$	4 834	1.50
(3)	$6d^4 7s^2$	$^5\mathrm{D}_2$	7 614	1.44
(4)	$6d^4 7s^2$	$^5\mathrm{D}_3$	9 607	1.39
(5)	$6d^4 7s^2$	$^5\mathrm{D}_4$	10 335	1.27
(6)	$6d^4 7s^2$	$^5 2\mathrm{P}_0$	13 592	0.00
		Odd parity states		
(7)	$6d^3 7s^2 7p$	1°_2	14 717	0.57
(8)	$6d^3 7s^2 7p$	1°_1	17 043	0.71
(9)	$6d^3 7s^2 7p$	2°_2	20 444	1.13
(10)	$6d^3 7s^2 7p$	1°_3	20 628	0.97
(11)	$6d^4 7s 7p$	$^7\mathrm{F}^\circ_0$	20 979	0.00
(12)	$6d^3 7s^2 7p$	2°_1	22 041	2.02
(13)	$6d^3 7s^2 7p$	1°_4	24 132	1.11
(14)	$6d^3 7s^2 7p$	3°_1	24 382	1.19
(15)	$6d^4 7s 7p$	$^1\mathrm{S}^\circ_0$	25 362	0.00
(16)	$6d^3 7s^2 7p$	2°_3	25 966	1.29
(17)	$6d^3 7s^2 7p$	1°_5	26 271	1.17
(18)	$6d^3 7s^2 7p$	3°_2	26 420	1.22
(19)	$6d^4 7s 7p$	$^7\mathrm{F}^\circ_1$	27 030	1.40
(20)	$6d^3 7s^2 7p$	4°_2	27 416	1.74
(21)	$6d^4 7s 7p$	$^7\mathrm{F}^\circ_2$	29 976	1.41
(22)	$6d^3 7s^2 7p$	3°_0	30 055	0.00
(23)	$6d^3 7s^2 7p$	2°_4	30 372	1.25
(24)	$6d^3 7s^2 7p$	3°_3	30 753	1.09
(25)	$6d^3 7s^2 7p$	5°_1	30 868	0.92
(26)	$6d^3 7s^2 7p$	4°_3	31 647	1.34
(27)	$6d^3 7s^2 7p$	6°_2	32 040	1.13
(28)	$6d^3 7s^2 7p$	3°_4	32 073	1.00
(29)	$6d^3 7s^2 7p$	4°_0	32 381	0.00
(30)	$6d^3 7s^2 7p$	6°_1	32 520	1.21
(31)	$6d^4 7s 7p$	$^5\mathrm{D}^\circ_3$	32 885	1.47
(32)	$6d^3 7s^2 7p$	4°_4	33 339	1.23
(33)	$6d^3 7s^2 7p$	7°_2	33 602	1.08
(34)	$6d^3 7s^2 7p$	8°_2	34 147	1.45
(35)	$6d^3 7s^2 7p$	2°_5	34 380	1.12
(36)	$6d^3 7s^2 7p$	6°_3	34 538	1.13
(37)	$6d^3 7s^2 7p$	7°_1	35 110	1.42
(38)	$6d^3 7s^2 7p$	7°_3	35 897	1.31
(39)	$6d^3 7s^2 7p$	5°_4	36 629	1.29
(40)	$6d^3 7s^2 7p$	9°_2	36 695	1.24
(41)	$6d^3 7s^2 7p$	8°_3	36 846	1.18
(42)	$6d^3 7s^2 7p$	8°_1	37 169	1.30
(43)	$6d^3 7s^2 7p$	6°_4	37 218	1.25
(44)	$6d^3 7s^2 7p$	3°_5	37 542	1.26
(45)	$6d^3 7s^2 7p$	5°_0	38 322	0.00
(46)	$6d^3 7s^2 7p$	9°_3	38 547	1.12
(47)	$6d^3 7s^2 7p$	10°_2	38 915	1.22

Table 10.4: Low-lying spectrum of even and odd states parity for Hs I . We present the energy and Landé g-factor for each state J^{parity}. We present LS-notations only for comparison with lighter analogs. For SHE states where an analogous state cannot be found in the lighter analog the term is labeled according to the sequential number of the state (n) for the given J^{parity} group, n_J^{parity}.

	Major Configuration	Term	Energy (cm^{-1})	Landé g-factor
		Hs I		
	Even parity states			
(1)	$6d^6 7s^2$	$^5D_4$	0	1.37
(2)	$6d^6 7s^2$	$^5D_2$	2 102	1.38
(3)	$6d^6 7s^2$	$^5D_0$	7 400	0.00
(4)	$6d^6 7s^2$	$^5D_3$	8 270	1.43
(5)	$6d^6 7s^2$	$^5D_1$	9 285	1.41
(6)	$6d^6 7s^2$	$^3H_5$	15 816	1.11
	Odd parity states			
(7)	$6d^5 7s^2 7p$	1_2°	13 093	1.98
(8)	$6d^5 7s^2 7p$	1_3°	15 600	1.58
(9)	$6d^5 7s^2 7p$	2_2°	23 708	1.30
(10)	$6d^5 7s^2 7p$	2_3°	26 492	1.16
(11)	$6d^6 7s 7p$	$^7D_4^\circ$	27 394	1.58
(12)	$6d^5 7s^2 7p$	1_1°	29 444	1.17
(13)	$6d^5 7s^2 7p$	3_2°	29 794	1.34
(14)	$6d^6 7s 7p$	$^7D_5^\circ$	30 863	1.37
(15)	$6d^5 7s^2 7p$	3_3°	30 908	1.32
(16)	$6d^5 7s^2 7p$	4_2°	31 165	1.33
(17)	$6d^5 7s^2 7p$	2_4°	31 295	1.40
(18)	$6d^5 7s^2 7p$	1_0°	31 552	0.00
(19)	$6d^5 7s^2 7p$	3_4°	32 522	1.26
(20)	$6d^5 7s^2 7p$	5_2°	33 694	1.44
(21)	$6d^5 7s^2 7p$	4_3°	33 920	1.03
(22)	$6d^5 7s^2 7p$	2_1°	34 076	1.52
(23)	$6d^5 7s^2 7p$	2_5°	34 739	1.20
(24)	$6d^5 7s^2 7p$	5_3°	34 812	1.41
(25)	$6d^5 7s^2 7p$	4_4°	35 689	1.23
(26)	$6d^6 7s 7p$	$^7D_3^\circ$	35 705	1.56
(27)	$6d^5 7s^2 7p$	3_1°	35 990	1.81
(28)	$6d^6 7s 7p$	$^7D_2^\circ$	37 036	1.40
(29)	$6d^6 7s 7p$	$^7P_3^\circ$	37 237	1.33
(30)	$6d^5 7s^2 7p$	5_4°	37 443	1.18
(31)	$6d^5 7s^2 7p$	7_2°	38 519	1.34
(32)	$6d^6 7s 7p$	$^7P_4^\circ$	39 025	1.29
(33)	$6d^5 7s^2 7p$	3_5°	39 268	1.27
(34)	$6d^6 7s 7p$	$^7D_1^\circ$	39 512	2.11
(35)	$6d^5 7s^2 7p$	8_3°	39 652	1.38
(36)	$6d^5 7s^2 7p$	9_3°	40 783	1.19

Table 10.5: Low-lying spectrum of even and odd states parity for Mt I. We present the energy and Landé g-factor for each state J^{parity}. We present *LS*-notations only for comparison with lighter analogs. For SHE states where an analogous state cannot be found in the lighter analog the term is labeled according to the sequential number of the state (n) for the given J^{parity} group, n_J^{parity}.

	Major Configuration	Term	Energy (cm^{-1})	Landé g-factor
		Mt I		
		Even parity states		
(1)	$6d^7 7s^2$	$^4\text{F}_{9/2}$	0	1.265
(2)	$6d^7 7s^2$	$^4\text{F}_{3/2}$	5 047	1.214
(3)	$6d^7 7s^2$	$^4\text{F}_{5/2}$	7 996	1.222
(4)	$6d^7 7s^2$	$^4\text{F}_{7/2}$	12 628	1.213
(5)	$6d^7 7s^2$	$^2\text{G}_{3/2}$	17 368	0.931
(6)	$6d^7 7s^2$	$^2\text{G}_{5/2}$	18 467	1.409
		Odd parity states		
(7)	$6d^6 7s^2 7p$	$1^\circ_{7/2}$	21 879	1.44
(8)	$6d^6 7s^2 7p$	$1^\circ_{9/2}$	24 388	1.33
(9)	$6d^6 7s^2 7p$	$1^\circ_{3/2}$	24 524	1.51
(10)	$6d^6 7s^2 7p$	$1^\circ_{5/2}$	25 990	1.25
(11)	$6d^6 7s^2 7p$	$2^\circ_{5/2}$	31 975	1.54
(12)	$6d^6 7s^2 7p$	$1^\circ_{1/2}$	32 851	0.81
(13)	$6d^7 7s 7p$	$^6\text{D}^\circ_{9/2}$	33 505	1.40
(14)	$6d^6 7s^2 7p$	$2^\circ_{1/2}$	34 665	1.51
(15)	$6d^6 7s^2 7p$	$2^\circ_{7/2}$	35 117	1.29
(16)	$6d^6 7s^2 7p$	$2^\circ_{3/2}$	36 159	1.13
(17)	$6d^7 7s 7p$	$^6\text{F}^\circ_{11/2}$	38 027	1.31
(18)	$6d^6 7s^2 7p$	$3^\circ_{7/2}$	38 450	1.17
(19)	$6d^6 7s^2 7p$	$3^\circ_{9/2}$	39 296	1.13
(20)	$6d^6 7s^2 7p$	$2^\circ_{11/2}$	41 310	1.33

Table 10.6: Strong electric dipole transitions and isotopic shift parameters for Sg I. Only direct optical transitions to the ground state satisfying the E1 transition selection rules are shown. Here D_{E1} is the transition amplitude in a.u., A_{E1} is the transition rate, a, F, and $\tilde{F}$ are calculated isotopic shift parameters for the charge radius. The numbers in parentheses correspond to the numbered states in Table 10.3.

State		D_{E1} (a.u)	A_{E1} ($\times 10^6$ s^{-1})	a (cm^{-1})	F ($\frac{\mathrm{cm}^{-1}}{\mathrm{fm}^2}$)	$\tilde{F}$ (cm^{-1})
Sg I (Ground state: $^5\mathrm{D}_0$)						
(8)	1_1°	0.639	1.36	9.41	2.04	11.9
(12)	2_1°	-0.160	0.192	-2.95	-0.639	-3.73
(14)	3_1°	1.17	13.4	4.90	1.06	6.18
(19)	$^3\mathrm{P}_1^\circ$	-0.163	0.353	-19.7	-4.25	-24.8
(25)	5_1°	0.592	6.97	6.58	1.42	8.30
(30)	6_1°	-0.412	3.95	7.01	1.52	8.85
(37)	7_1°	-0.302	2.67	1.66	0.36	2.10
(42)	8_1°	0.148	0.761	3.55	0.768	4.48
(51)	9_1°	0.524	11.9	-4.77	-1.03	-6.01

Table 10.7: Strong electric dipole transitions and isotopic shift parameters for Bh I. Only direct optical transitions to the ground state satisfying the E1 transition selection rules are shown. Here D_{E1} is the transition amplitude in a.u., A_{E1} is the transition rate, a, F, and $\tilde{F}$ are calculated isotopic shift parameters for the charge radius. The numbers in parentheses correspond to the numbered states in Table 10.2.

State	D_{E1} (a.u)	A_{E1} ($\times 10^6\,\mathrm{s}^{-1}$)	a (cm^{-1})	F ($\frac{\mathrm{cm}^{-1}}{\mathrm{fm}^2}$)	$\tilde{F}$ (cm^{-1})
Bh I (Ground State: $^6\mathrm{S}_{5/2}$)					
(9) $^6\mathrm{D}^\circ_{3/2}$	-0.172	0.107	18.1	3.74	22.8
(10) $^8\mathrm{P}^\circ_{5/2}$	-0.474	0.812	83.4	17.2	105
(11) $^6\mathrm{P}^\circ_{3/2}$	-0.494	1.38	-101	-20.7	-127
(12) $^6\mathrm{D}^\circ_{5/2}$	-0.0391	0.00611	-120	-24.6	-151
(13) $^8\mathrm{P}^\circ_{7/2}$	0.500	0.858	84.5	17.4	107
(14) $^6\mathrm{D}^\circ_{7/2}$	0.345	0.471	-63.3	-13.0	-79.7
(16) $^6\mathrm{F}^\circ_{5/2}$	1.51	16.6	-160	-33.0	-202
(18) $3^\circ_{3/2}$	1.50	30.0	-64.9	-13.4	-81.7
(19) $3^\circ_{7/2}$	1.75	23.3	44.0	9.06	55.4
(20) $4^\circ_{5/2}$	-0.433	1.90	-101	-20.7	-127
(21) $4^\circ_{7/2}$	1.88	31.2	-380	-78.4	-479
(22) $4^\circ_{3/2}$	-0.998	18.6	-41.3	-8.51	-52
(24) $5^\circ_{5/2}$	-0.101	0.131	-105	-21.6	-132
(26) $5^\circ_{3/2}$	0.438	4.27	-135	-27.9	-170
(27) $6^\circ_{5/2}$	-1.06	17.1	-364	-74.9	-458
(28) $5^\circ_{7/2}$	0.0665	0.0361	-34.7	-7.15	-43.7
(29) $6^\circ_{3/2}$	0.160	0.615	-70.6	-14.5	-88.9
(30) $7^\circ_{5/2}$	-0.539	4.86	-335	-69.0	-422
(33) $6^\circ_{7/2}$	-0.674	6.18	-129	-26.6	-163
(34) $7^\circ_{3/2}$	0.387	4.09	-513	-106	-647
(37) $8^\circ_{5/2}$	0.232	1.10	-561	-116	-707
(38) $7^\circ_{7/2}$	0.516	4.13	-364	-75.1	-459

Table 10.8: Strong electric dipole transitions and isotopic shift parameters for Hs I. Only direct optical transitions to the ground state satisfying the E1 transition selection rules are shown. Here D_{E1} is the transition amplitude in a.u., A_{E1} is the transition rate, a, F, and $\tilde{F}$ are calculated isotopic shift parameters for the charge radius. The numbers in parentheses correspond to the numbered states in Table 10.4.

State	D_{E1} (a.u)	A_{E1} ($\times 10^6$ s^{-1})	a (cm^{-1})	F ($\frac{\text{cm}^{-1}}{\text{fm}^2}$)	$\tilde{F}$ (cm^{-1})
Hs I (Ground State: $^5D_4$)					
(8) 1°_3	0.501	0.276	22.7	4.45	28.9
(10) 2°_3	0.224	0.269	22.9	4.49	28.8
(11) $^7D^\circ_4$	-1.11	5.66	-29.1	-5.70	-36.6
(14) $^7D^\circ_5$	0.999	5.41	-26.2	-5.15	
(15) 3°_3	0.208	0.370	16.2	3.18	20.4
(17) 2°_4	0.0934	0.0603	5.54	1.09	6.98
(19) 3°_4	0.120	0.112	18.5	3.62	23.2
(21) 4°_3	-0.150	0.253	20.7	4.05	26.0
(23) 2°_5	-1.13	9.88	12.3	2.42	15.5
(24) 5°_3	1.70	35.5	12.3	2.41	15.5
(25) 4°_4	0.798	6.52	7.84	1.54	9.87
(26) $^7D^\circ_3$	-0.493	3.20	-33.3	-6.53	-41.9
(29) $^7P^\circ_3$	-0.511	3.91	-15.8	-3.11	-19.9
(30) 5°_4	-0.297	1.04	1.95	0.382	2.45
(32) $^7P^\circ_4$	0.425	2.41	-9.56	-1.87	-12.0
(33) 3°_5	2.64	77.5	5.16	1.01	6.49
(35) 7°_3	2.10	80.0	-2.30	-0.451	-2.89

Table 10.9: Strong electric dipole transitions and isotopic shift parameters for Mt I. Only direct optical transitions to the ground state satisfying the E1 transition selection rules are shown. Here D_{E1} is the transition amplitude in a.u., A_{E1} is the transition rate, a, F, and $\tilde{F}$ are calculated isotopic shift parameters for the charge radius. The numbers in parentheses correspond to the numbered states in Table 10.5.

State	D_{E1} (a.u)	A_{E1} ($\times 10^6\,\mathrm{s}^{-1}$)	a (cm^{-1})	F ($\frac{\mathrm{cm}^{-1}}{\mathrm{fm}^2}$)	$\tilde{F}$ (cm^{-1})
		Mt I (Ground State: $^4\mathrm{F}_{9/2}$)			
(7) $1^\circ_{7/2}$	0.0537	0.00765	27.5	5.10	34.5
(8) $1^\circ_{9/2}$	0.432	0.550	27.6	5.13	34.7
(13) $^6\mathrm{D}^\circ_{9/2}$	1.27	12.3	-51.7	-9.60	-64.9
(15) $2^\circ_{7/2}$	-0.294	0.946	33.3	6.18	41.8
(17) $^6\mathrm{F}^\circ_{11/2}$	-1.89	33.3	-47.9	-8.89	-60.1
(19) $3^\circ_{9/2}$	0.0954	0.112	19.0	3.53	23.9
(20) $2^\circ_{11/2}$	0.170	0.344	25.7	4.78	32.3

Table 10.10: Theoretical and experimental ionization potentials of open $5d$-shell elements. The CIPT energies are the results of the present work.

Atom	Ionic State	J	IP (eV) Expt. [247]	CIPT	MCDF
Ta	$5d^3 6s$	1	7.549	7.57	
W	$5d^4 6s$	1/2	7.864	7.90	6.97 [277]
Re	$5d^5 6s$	3	7.833	7.85	6.84 [278]
Os	$5d^6 6s$	9/2	8.438	8.69	7.45 [278]
Ir	$5d^7 6s$	5	8.967	9.27	

Table 10.11: Some excitation energies (cm^{-1}) in open $6d$-shell SHE and their lighter analogs. The CIPT energies are the results of the present work.

Atom	State		Expt. [247]	CIPT	MCDF [277, 278]
W	$5d^4 6s^2$	$^5\mathrm{D}_1$	1670	1502	1162
		$^5\mathrm{D}_2$	3325	2664	2581
Re	$5d^5 6s6p$	$^8\mathrm{P}^\circ_{5/2}$	18950		14000
Os	$5d^6 6s6p$	$^7\mathrm{D}^\circ_5$	23463	26000	20500
Sg	$6d^4 7s^2$	$^5\mathrm{D}_1$		4834	4186
		$^5\mathrm{D}_2$		7614	7211
Bh	$6d^5 7s7p$	$^8\mathrm{P}^\circ_{5/2}$		2220	15100
Hs	$6d^5 7s^2 7p$	$^5\mathrm{S}^\circ_2$		13100	5100
		$^5\mathrm{D}^\circ_3$		15600	8600

Table 10.12: Ionization potentials of open $6d$-shell SHE, including ions. The CIPT energies are the results of the present work.

Atom or ion	Ground State	J	IP (eV) CIPT	RHF[1]	MCDF [277, 278]	Extrap. [277, 278]
Db I	$6d^3 7s^2$	2	7.01	6.75		
Sg I	$6d^4 7s^2$	0	8.22	7.70	7.03	7.85
Sg II	$6d^3 7s^2$	3/2	18.0		15.85	17.06
Sg III	$6d^2 7s^2$	2	24.8		24.61	25.74
Bh I	$6d^5 7s^2$	5/2	8.03	8.63	6.82	7.7
Bh II	$6d^4 7s^2$	0	19.0		16.55	17.5
Bh III	$6d^4 7s$	1/2	26.2		25.64	26.6
Bh IV	$6d^4$	0	36.8		36.33	37.3
Hs I	$6d^6 7s^2$	4	8.52	9.52	6.69	7.6
Hs II	$6d^5 7s^2$	5/2	19.7		16.62	18.2
Hs III	$6d^4 7s^2$	3	27.7		27.12	29.3
Hs IV	$6d^4 7s$	1/2	40.5		36.59	37.7
Hs V	$6d^4$	0	50.6		50.37	51.2
Mt I	$6d^7 7s^2$	9/2	9.86	10.4		
Mt II	$6d^6 7s^2$	4	20.7			
Mt III	$6d^5 7s^2$	5/2	28.4			
Mt IV	$6d^5 7s$	3	43.3			
Mt V	$6d^5$	5/2	50.3			

Chapter Eleven

Oganesson

The results of this chapter were published in Ref. [3] The super heavy element (SHE) oganesson ($Z = 118$) was first synthesized in 2006 at Dubna [279] and has recently been officially named and recognized [215]. It is also the first SHE and not naturally occuring element in the group of noble elements (Group 18) where the ground state has completely filled electron np shells. Like other SHEs ($Z > 100$) it is of great experimental and theoretical interest due to the high relativistic nature which may result in exotic and anomalous chemical and physical properties [280, 214]. In general, experimental study of SHEs is difficult due to the short lifetimes and low production rates. Og is no exception, where the only confirmed isotope (^{294}Og) has a halflife of 0.7 ms [279]. The study of Og and other SHEs is of great interest due to their exotic characteristics such as the large dependence on relativistic effects and the possible existence of long-lived isotopes of heavy nuclei in the "island of stability".

The existence of long lived SHEs is predicted to occur when the ratio of neutrons to protons (N/Z) is large enough for the neutron-proton attraction to overcome the Coulombic repulsion between protons (which scales as Z^2). Therefore the number of neutrons must increase faster than the number of protons requiring extremely neutron-rich isotopes to be long-living[170, 169]. Early nuclear shell models predict the nuclear shells stabilize for the "magic" numbers $Z = 114$ and $N = 184$[170, 169]. Synthesizing these neutron-rich isotopes is an extremely difficult challenge as the collision of two nuclei with a smaller N/Z will always result in a neutron poor element. However an alternate route to identify these long lived SHEs may be through analysing astrophysical data. Such avenues have already been explored with astrophysical data of Przybylski's star suggesting that elements up to $Z = 99$ have probably been identified[263, 264, 265].

They may be decay products of long lived nuclei (see e.g. [254] and references therein). It is suspected that neutron rich isotopes may be created in cosmic events where rapid neutron capture ("r-process") can occur due to large neutron fluxes during supernovae explosions, neutron star - (black hole and neutron star) mergers [266, 267, 268, 269]. To predict atomic transition frequencies for the neutron-reach isotopes the calculated isotopic shifts should be added to the atomic transition frequencies measured in laboratories for the neutron-poor isotopes [254]. Search for these SHE in astrophysical data requires the strong electric dipole (E1) transitions which we calculate in this work. There has been a large amount of theoretical work on the chemical and physical properties of Og with calculations of solid state and molecular properties [281, 282, 283, 196, 284], electron affinities[285, 286, 287, 288, 289], and ionisation potentials and polarisibilities [287, 290, 196, 291]. While some odd parity states and electric dipole (E1) transitions in the Og spectrum have been calculated in [202] we present a more complete spectrum with both odd and even states to compare against similar states in the Rn spectrum.

There has been considerable work on both relativistic and quantum electrodynamic (QED) effects [292, 291, 289, 192, 202, 293] in Og. In this work we included both the Breit interaction and QED radiative effects. To aid in the experimental study of Og we use theoretical methods to further study its physical properties.

11.1 CIPT calculation of

In Table ?? we present the results of our CIPT calculations for Rn I and Og I. We compare the Rn I CIPT calculations to the experimental results. The lack of experimental g-factors for Rn I make it difficult to confirm the correct identification of the states and therefore we must rely solely on the order of the energy levels. We find that there is good agreement between the experimental and theoretical states with an agreement with $\Delta \approx -900$ cm^{-1} with the largest discrepancy $\Delta \approx -1239$ cm^{-1}. We expect a similar accuracy for our Og I calculations (also presented in Table ??).

Comparing the spectrum of Rn to Og we see that despite the similar electronic structure (with differing principal quantum numbers) there are significant differences. The Og spectrum is much more dense than Rn with the first excitation lying more than 20 000 cm^{-1} below the equivalent excitation in Rn. This results in an odd parity state which lies in the optical region. This makes the state a good candidate for initial experimental measurement. In the final column of Table ?? we present the states calculated in ref. [202]. This work

Table 11.1: CIPT calculations of excitation spectrum, ionisation potential and electron affinity for Rn I with experimental results for comparison. Here E_E and E_T are experimental and theoretical CIPT excitation energies respectively with $\Delta = E_E - E_T$. We also present the calculated Landé g-factors and the energy difference between the experimental and theoretical excitation energies. (Originally published in [3])

	State	J	Rn I E_E[247] (cm^{-1})	E_T (cm^{-1})	g_T	Δ (cm^{-1})
$6s^26p^6$	^{1}S	0	0	0	0	
$6s^26p^57s$	^{3}P°	2	54 620	55 323	1.50	-703
$6s^26p^57s$	^{1}P°	1	55 989	56 607	1.18	-618
$6s^26p^57p$	^{3}S	1	66 245	67 171	1.76	-926
$6s^26p^57p$	^{3}D	2	66 708	67 658	1.13	-950
$6s^26p^56d$	^{1}S°	0	67 906	69 145	0	
$6s^26p^57p$	^{3}D	3	68 039	68 891	1.33	-852
$6s^26p^57p$	^{1}P	1	68 332	69 313	1.09	-981
$6s^26p^57p$	^{3}P	2	68 790	69 749	1.37	-959
$6s^26p^56d$	^{3}P°	1	68 891	70 002	1.36	-1 111
$6s^26p^57p$	^{1}S	0	69 744	70 800	0	-1 056
$6s^26p^56d$	^{3}F°	4	69 798	70 742	1.25	-944
$6s^26p^56d$	^{3}D°	2	70 223	71 188	1.32	-965
$6s^26p^56d$	^{3}F°	3	70 440	71 334	1.06	-894
			Ionisation potential			
$6s^26p^5$	^{2}P°	3/2	86 693	87 721	1.33	-1 028
			Electron Affinity			
$6s^26p^67s$	^{2}S	1/2		1 868	2.00	

also did not present g-factors which made comparing states uncertain, therefore we compared them by ordering energies. For 4 of the states there was good agreement with our results lying within 1000 cm^{-1} however for the other states there was a large discrepancy of > 4000 cm^{-1}.

Our calculated value of the ionisation potential of Og in Table **??** is in excellent agreement with the value calculated in Ref. [291] ($E_{IP} =$71 320 cm^{-1}) where a CCSD(T) method was used.

It has been shown that Og has a positive electron affinity which is an anomaly in the group of noble gases [286, 289, 192]. This is another consequence of the stabilized $8s$ orbital due to the large relativistic effects. Our calculation presented in Table **??** confirms this with an electron affinity of 773 cm^{-1} (0.095 eV) which is in good agreement with the coupled cluster value presented in [289]. For comparison we also present the negative ion calculation for Rn I which is known to be unstable. All other negative ionic states of Og were found to be

Table 11.2: CIPT calculations of excitation spectrum, ionisation potential and electron affinity for Og I. Here E_T and g_T are the theoretical CIPT excitation energies and Landé g-factors respectively. (Originally published in [3])

	State	J	E_T (cm^{-1})	g_T	Ref. [202] (cm^{-1})
			Og I		
$7s^27p^6$	^{1}S	0	0	0	0
$7s^27p^58s$	^{3}P°	2	33 884	1.50	34 682
$7s^27p^58s$	^{1}P°	1	36 689	1.17	38 150
$7s^27p^58p$	^{3}P	1	49 186	1.60	
$7s^27p^58p$	^{3}D	2	49 451	1.15	
$7s^27p^58p$	^{3}D	3	53 777	1.33	
$7s^27p^58p$	^{3}P	1	53 881	1.24	
$7s^27p^57d$	^{1}S°	0	54 155	0	53 556
$7s^27p^58p$	^{3}P	2	54 446	1.35	
$7s^27p^57d$	^{1}S°	1	54 725	1.33	54 927
$7s^27p^57d$	^{3}F°	4	54 938	1.25	48 474
$7s^27p^57d$	^{3}D°	2	55 416	1.30	49 039
$7s^27p^57d$	^{3}F°	3	55 622	1.06	49 603
$7s^27p^58p$	^{1}S	0	55 729	0	
$7s^27p^57d$	^{1}D°	2	56 317	0.98	50 410
$7s^27p^57d$	^{5}F°	3	56 343	1.25	50 168
$7s^27p^57d$	^{1}P°	1	57 855	0.84	58 072
	Ionisation potential				
$7s^27p^5$	^{2}P°	3/2	71 508	1.33	71 320[291]
	Electron Affinity				
$7s^27p^68s$	^{2}S	1/2	-773[a]	2.00	-516 [289]

[a] Negative value indicates the state is bound.

unstable.

11.2 Electric dipole transitions of

While Og follows the expected trend for elements in noble group where each consecutive element has both a smaller IP and first excitation energy. However Og has some properties which can be considered exotic even amongst the Group 18 elements. According to the calculated spectrum in Table ?? it is the only noble element which has an allowed optical electric dipole (E1) transition ($\omega <$40 000 cm^{-1}) from the ground state, unlike Rn where the first odd state lies at 57 334 cm^{-1}.

The E1 transition amplitudes, A_{E1}, between states which satisfy the con-

ditions of opposite parity and $\Delta J \leq 1$ are calculated using the many-electron wavefunctions created in the CIPT method and the self-consistent random-phase approximation which includes polarization of the atomic electron core by an external electromagnetic field. The details of the method are presented in Ref. [237].

The E1 transition rate is calculated using (in atomic units),

$$T_{E1} = \frac{4}{3} (\alpha\omega)^3 \frac{A_{E1}^2}{2J+1} \tag{11.1}$$

where J is the angular momentum of the upper state, α is the fine structure constant and ω is the frequency of the transition in atomic units. The transition amplitudes and transition rates for the allowed E1 transitions in Og are presented in Table 11.4. In ref. [202] the major E1 transition rates were also calculated with a MCDF approach, these are included for comparison Table 11.4.

We calculated the rates of the $(n+1)s \rightarrow np$ transitions in lighter neutral noble elements Kr and Xe and compared them to experimental values, these are presented in Table 11.3. The experimental uncertainties are approximately 2% for Xe I transitions [294] and 10-25% for Kr I transitions[295]. Comparing our calculated values to the experimental values in Table 11.3 we see the accuracy for these transitions is from 0.6% to 17.7%. We used the experimental energies to calculate the transitions rates of Kr I and Xe I using (11.1) and since the uncertainty in the experimental energies are negligible the uncertainty in our calculations compared to experimental results in Table 11.3 is equivalent to the uncertainty in the square of the calculated transition amplitude A_{E1}^2. For our calculation of the Og I transition rates we needed to take into account the non-negligible uncertainty in the energies of our CIPT calculations. Therefore assuming an accuracy of 18% for A_{E1}^2 and an uncertainty of 3% in the CIPT energy ($|\Delta| \approx 1000$ cm^{-1}) we expect a transition rate accuracy of 20% for the $8s \rightarrow 7p$ optical transition ($\omega = 36\,689$ cm^{-1}) of Og I in Table 11.4.

Only the first transition in Table 11.4 lies in the optical region and therefore it has the highest likelihood of being measured first. The large rate of the transition $^1S_0 \rightarrow {}^1P_1^\circ$ is also promising for experimental measurement.

11.3 Electron density of

The electron density of SHE gives insight into the effectiveness of the codes.

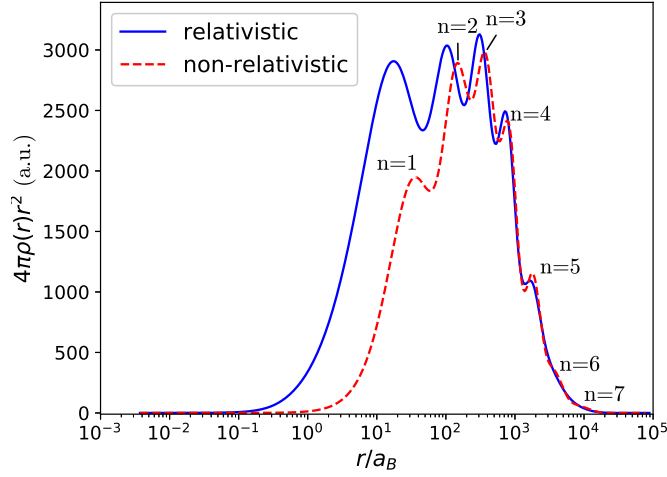It has been shown in Ref. [291] using fermion localization that the electron

Figure 11.1: Radial electron density, $4\pi\rho(r)r^2$ plot for Og I in both relativistic and non-relativistic approximations. The solid blue line and the dashed red line are non-relativistic and relativistic approximations respectively. The principle quantum peaks have been labeled for the non-relativic plot. (Originally published in [3])
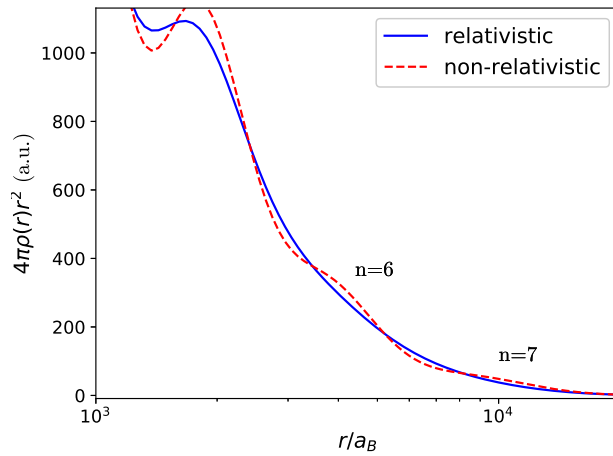

Figure 11.2: Lower right section of Figure 11.1.

Table 11.3: Comparison of E1 transition rates between experimental and CIPT values for Kr I and Xe I. Here A_{E1} is the transition amplitude in atomic units and T_{E1} is the transition rate.

State	E_{Exp} (cm^{-1})	A_{E1} (a.u.)	$T_{\text{E1, CIPT}}$ ($\times 10^6$ s^{-1})	$T_{\text{E1,Exp}}$ ($\times 10^6$ s^{-1})
		Kr I		
$^1\text{P}^\circ_1$	80 916	0.94	314	312[295]
$^3\text{P}^\circ_1$	85 846	0.87	320	316[295]
		Xe I		
$^1\text{P}^\circ_1$	68 045	1.18	295	273 [294]
$^3\text{P}^\circ_1$	77 185	0.98	298	253 [294]

Table 11.4: Electric dipole transition amplitudes of Og I from the ground state $^1\text{S}_0$ to the excited states of odd parity and angular momenta $J = 1$. Here A_{E1} is the transition amplitude in atomic units and T_{E1} is the transition rate. We include results of MCDF calculations from ref. [202] for comparision. There is significant disagreement for the third transition however there is another transition in [202] which has a rate (986×10^6 s^{-1}) close to our calculated value. So, the disagreement may be the result of a misprint in [202]. (Originally published in [3]).

State	E_{CIPT} (cm^{-1})	A_{E1} (a.u.)	$T_{\text{E1, CIPT}}$ ($\times 10^6$ s^{-1})	$T_{\text{E1,MCDF}}$ [202] ($\times 10^6$ s^{-1})
$^1\text{P}^\circ_1$	36 689	2.09	145	204
$^1\text{S}^\circ_1$	54 725	0.727	58.4	55.3
$^1\text{P}^\circ_1$	57 855	-2.67	936	9.9, 986*

density of Og is smoother than other group 18 analogues which have distinct atomic shells . The cause of this is the large relativistic effects in SHE which effectively smear out the shells into a smoother electron density (the same was shown for the nucleon density). The relativistic effects can also be seen by looking at the radial electron densities with relativistic and non-relativistic approximations. The Hartree-Fock radial electron density for Og is plotted on a logarithmic scale in Figure 11.1 in both the relativistic and non-relativistic approximations. There are a total of 7 peaks in the radial densities corresponding to the principle quantum numbers n where lower shells have distinct peaks in both the relativistic and non-relativistic approximations. As expected, in the relativistic approximation the inner shells ($n = 1, 2, 3$) shift closer to the nucleus however higher shells are relatively unaffected ($n \geq 4$). This results in a similar density profile for the electrons a large distance away from the nucleus.

In Figure 11.2 we plot the tail of the density function in Figure 11.1. Here

we see that, while spread out, the principle shell peaks still exist in the non-relativistic approximation. However in the relativistic approximation the density has been smoothed out to such a degree that there are no discernible peaks. This supports the results in ref. [291] where they calculated the electron shell structure of Og I and found that it disappears for external shells due to the high relativistic effects. This can be explained as the large spin-orbit splitting doubles the number of sub-shells which overlap making the overall distribution smooth.

Chapter Twelve

Conclusion

We have calculated low lying energy levels, electric dipole transition amplitudes and isotope shift for superheavy element dubnium. Similar CIPT calculations for its lighter analog Ta indicate that the uncertainty of the results for the energies of Db is unlikely to exceed 500 cm^{-1}. Db is the first SHE with open $6d$ shell which is studied with the recently developed CIPT method.

In this work we calculated the spectrum and E1 transitions for Og I including the ionisation potential. We demonstrated the accuracy of the calculations by comparing similar calculations of Rn I to experimental data and expect an uncertainty of no more than $|\Delta| \approx 1000$ cm^{-1}. We found the spectrum of Og I is dense compared to other elements in group 18 with significantly lower ionisation potential and excited states which follows the periodic trend. This compact spectrum introduces an allowed optical E1 transition which does not exist in other group 18 elements which presents a possibility for future experimental measurements. Our work also supports recent findings[291] which suggest the electron shell structure of Og I is less prominent than lighter elements due to large relativistic effects which results in the outer electron density to becoming smooth.

Appendix One

Nilsson Orbitals

In Chapter 3 I discussed the Nilsson model for deformed nuclei. In this Appendix I present the Nilsson values for each nucleons and the open shell configurations for the nuclei of interest.

Table A.1: This table presents the collective Nilsson values $\sum 2n_z + 1$ and $\sum N - n_z + 1$ for major shells N. This is identical for both protons and neutrons.

Filled N Shell	$\sum 2n_z + 1 = \sum N - n_z + 1$
0	2
1	10
2	28
3	60
4	110
5	182

(a) $50 < Z < 82$

(b) $Z > 82$

(c) $82 < N < 126$

(d) $N > 126$

Figure A.1: Nilsson energy diagrams for both protons and neutrons for prolate deformed nuclei. Here δ_{osc} is a degree of deformation. The numbers in circles represent the magic numbers in the spherical limit. These figures have been taken from A. Bohr B. R. Mottelson, Nuclear Structure Vol. 2 [126].

100
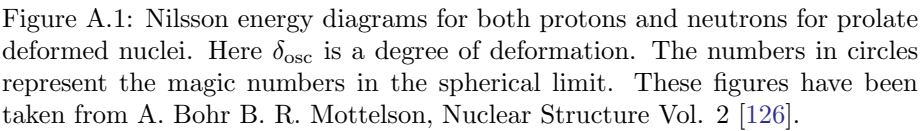
Table A.2: Nilsson values, $2n_z + 1$, $N - n_z + 1$ and $\Sigma\Lambda$ for individual nucleons.

l_m	$\Omega[Nn_z\Lambda]$	$2n_z + 1$	$N - n_z + 1$	$\Sigma\Lambda$
		$N = 0$		
$1s_{1/2}$	1/2[000]	1	1	0
		$N = 1$		
$1p_{3/2}$	1/2[110]	3	1	0
$1p_{3/2}$	3/2[101]	1	2	1/2
$1p_{1/2}$	1/2[101]	1	2	-1/2
		$N = 2$		
$1d_{5/2}$	1/2[220]	5	1	0
$1d_{5/2}$	3/2[211]	3	2	1/2
$1d_{5/2}$	5/2[202]	1	3	1
$2s_{1/2}$	1/2[211]	3	2	-1/2
$1d_{3/2}$	1/2[200]	1	3	0
$1d_{3/2}$	3/2[202]	1	3	-1
		$N = 3$		
$1f_{7/2}$	1/2[330]	7	1	0
$1f_{7/2}$	3/2[321]	5	2	1/2
$1f_{7/2}$	5/2[312]	3	3	1
$1f_{7/2}$	7/2[303]	1	4	3/2
$2p_{3/2}$	1/2[321]	5	2	-1/2
$2p_{3/2}$	3/2[312]	3	3	-1
$1f_{5/2}$	1/2[310]	3	3	0
$1f_{5/2}$	3/2[301]	1	4	1/2
$1f_{5/2}$	5/2[303]	1	4	-3/2
$2p_{1/2}$	1/2[301]	1	4	-1/2
		$N = 4$		
$1g_{9/2}$	1/2[440]	9	1	0
$1g_{9/2}$	3/2[431]	7	2	1/2
$1g_{9/2}$	5/2[422]	5	3	1
$1g_{9/2}$	7/2[413]	3	4	3/2
$1g_{9/2}$	9/2[404]	1	5	2
$1g_{7/2}$	1/2[431]	7	2	-1/2
$1g_{7/2}$	3/2[422]	5	3	-1
$1g_{7/2}$	5/2[413]	3	4	-3/2
$1g_{7/2}$	7/2[404]	1	5	-2
$2d_{5/2}$	1/2[420]	5	3	0
$2d_{5/2}$	3/2[411]	3	4	1/2
$2d_{5/2}$	5/2[402]	1	5	1
$2d_{3/2}$	1/2[411]	3	4	-1/2
$2d_{3/2}$	3/2[402]	1	5	-1
$3s_{1/2}$	1/2[400]	1	5	1/2

l_m	$\Omega[Nn_z\Lambda]$	$2n_z + 1$	$N - n_z + 1$	$\Sigma\Lambda$
		$N = 5$		
$1h_{11/2}$	1/2[550]	11	1	0
$1h_{11/2}$	3/2[541]	9	2	1/2
$1h_{11/2}$	5/2[532]	7	3	1
$1h_{11/2}$	7/2[523]	5	4	3/2
$1h_{11/2}$	9/2[514]	3	5	2
$1h_{11/2}$	11/2[505]	1	6	5/2
$1h_{9/2}$	1/2[541]	9	2	-1/2
$1h_{9/2}$	3/2[532]	7	3	-1
$1h_{9/2}$	5/2[523]	5	4	-3/2
$1h_{9/2}$	7/2[514]	3	5	-2
$1h_{9/2}$	9/2[505]	1	6	-5/2
$2f_{7/2}$	1/2[530]	7	3	0
$2f_{7/2}$	3/2[521]	5	4	1/2
$2f_{7/2}$	5/2[512]	3	5	1
$2f_{7/2}$	7/2[503]	1	6	3/2
$3p_{3/2}$	1/2[521]	5	4	-1/2
$3p_{3/2}$	3/2[512]	3	5	-1
$2f_{5/2}$	1/2[510]	3	5	0
$2f_{5/2}$	3/2[501]	1	6	1/2
$2f_{5/2}$	5/2[503]	1	6	-3/2
$3p_{1/2}$	1/2[501]	1	6	-1/2
		$N = 6$		
$1i_{13/2}$	1/2[660]	13	1	0
$1i_{13/2}$	3/2[651]	11	2	1/2
$1i_{13/2}$	5/2[642]	9	3	2
$1i_{13/2}$	7/2[633]	7	4	3/2
$1i_{13/2}$	9/2[624]	5	5	2
$1i_{13/2}$	11/2[615]	3	6	5/2
$1i_{13/2}$	13/2[606]	1	7	3
$2g_{9/2}$	1/2[651]	11	2	-1/2
$2g_{9/2}$	3/2[642]	9	3	-1
$2g_{9/2}$	5/2[633]	7	4	-3/2
$2g_{9/2}$	7/2[624]	5	5	-2
$2g_{9/2}$	9/2[615]	3	6	-5/2
$1i_{11/2}$	1/2[640]	9	3	0
$1i_{11/2}$	3/2[631]	7	4	1/2
$1i_{11/2}$	5/2[622]	5	5	1
$1i_{11/2}$	7/2[613]	3	6	3/2
$1i_{11/2}$	9/2[604]	1	7	2
$1i_{11/2}$	11/2[606]*	1	7	-3
$\vdots$	$\vdots$	$\vdots$	$\vdots$	$\vdots$

l_m	$\Omega[Nn_z\Lambda]$	$2n_z+1$	$N-n_z+1$	$\Sigma\Lambda$
		$N=7$		
$1j_{15/2}$	$1/2[770]$	15	1	0
$1j_{15/2}$	$3/2[761]$	13	2	$1/2$
$1j_{15/2}$	$5/2[752]$	11	3	1
$1j_{15/2}$	$7/2[743]$	9	4	$3/2$
$1j_{15/2}$	$9/2[734]$	7	5	2
$1j_{15/2}$	$11/2[725]$	5	6	$5/2$
$1j_{15/2}$	$13/2[716]$	3	7	3
$1j_{15/2}$	$15/2[707]$	1	8	$7/2$
$\vdots$	$\vdots$	$\vdots$	$\vdots$	$\vdots$

A.1   Filled and Unfilled shells of Nuclei

Below is a table of the filled and unfilled N shells of the deformed nuclei of interest. For Eu isotopes there are two applicable deformations, large or small. Due to the relative electric quadrupole moment of the two isotopes we assumed a large deformation for ^{153}Eu and small deformation for ^{151}Eu.

Nuclei	Deformation (δ)	Protons	Neutrons
^{9}Be		Filled Shells: N/A $1s_{1/2}$: $\pm 1/2$ $1p_{3/2}$: $\pm 1/2$	Filled Shells: N/A $1s_{1/2}$: $\pm 1/2$ $1p_{3/2}$: $\pm 1/2$, 3/2
^{21}Ne		Filled Shells: N/A $1s_{1/2}$: $\pm 1/2$ $1p_{3/2}$: $\pm 1/2$, $\pm 3/2$ $1p_{1/2}$: $\pm 1/2$ $1d_{5/2}$: $\pm 1/2$	Filled Shells: N/A $1s_{1/2}$: $\pm 1/2$ $1p_{3/2}$: $\pm 1/2$, $\pm 3/2$ $1p_{1/2}$: $\pm 1/2$ $1d_{5/2}$: $\pm 1/2$ 3/2
^{27}Al		Filled Shells: N/A $1s_{1/2}$: $\pm 1/2$ $1p_{3/2}$: $\pm 1/2$, $\pm 3/2$ $1p_{1/2}$: $\pm 1/2$ $1d_{5/2}$: $\pm 1/2$, $\pm 3/2$, 5/2	Filled Shells: N/A $1s_{1/2}$: $\pm 1/2$ $1p_{3/2}$: $\pm 1/2$, $\pm 3/2$ $1p_{1/2}$: $\pm 1/2$ $1d_{5/2}$: $\pm 1/2$, $\pm 3/2$, $\pm 5/2$
^{163}Dy	≈ 0.2	Filled Shells: N = 0, 1, 2, 3 $1g_{9/2}$: Full Shell $1g_{7/2}$: $\pm 1/2$, $\pm 3/2$, $\pm 5/2$ $2d_{5/2}$: $\pm 1/2$, $\pm 3/2$ $1h_{11/2}$:$\pm 1/2$, $\pm 3/2$, $\pm 5/2$	Filled Shells: N = 0, 1, 2, 3, 4 $1h_{11/2}$: Full Shell $2f_{7/2}$: $\pm 1/2$, $\pm 3/2$, 5/2 $1h_{9/2}$: $\pm 1/2$, $\pm 3/2$ $1i_{13/2}$: $\pm 1/2$, $\pm 3/2$
^{173}Yb	≈ 0.3	Filled Shells: N = 0, 1, 2, 3 $1g_{9/2}$: Full Shell $1g_{7/2}$: $\pm 1/2$, $\pm 3/2$, $\pm 5/2$ $2d_{5/2}$: $\pm 1/2$, $\pm 3/2$ $1h_{11/2}$:$\pm 1/2$, $\pm 3/2$, $\pm 5/2$, $\pm 7/2$ $2d_{3/2}$: $\pm 1/2$	Filled Shells: N = 0, 1, 2, 3, 4 $1h_{11/2}$: Full Shell $2f_{7/2}$: $\pm 1/2$, $\pm 3/2$, $\pm 5/2$ $1h_{9/2}$: $\pm 1/2$, $\pm 3/2$, 5/2 $1i_{13/2}$:$\pm 1/2$, $\pm 3/2$, $\pm 5/2$, $\pm 7/2$ $3p_{3/2}$: $\pm 1/2$
^{177}Hf		Filled Shells: N = 0, 1, 2, 3 $1g_{9/2}$: Full Shell $1g_{7/2}$: Full Shell $2d_{5/2}$: $\pm 1/2$, $\pm 3/2$, $\pm 5/2$ $1h_{11/2}$:$\pm 1/2$, $\pm 3/2$, $\pm 5/2$, $\pm 7/2$	Filled Shells: N = 0, 1, 2, 3, 4 $1h_{11/2}$: Full Shell $2f_{7/2}$: Full Shell $1h_{9/2}$: $\pm 1/2$, $\pm 3/2$, 5/2 $1i_{13/2}$:$\pm 1/2$, $\pm 3/2$, $\pm 5/2$, $\pm 7/2$
^{179}Hf	≈ 0.1	Filled Shells: N = 0, 1, 2, 3 $1g_{9/2}$: Full Shell $1g_{7/2}$: Full Shell $2d_{5/2}$: $\pm 1/2$, $\pm 3/2$, $\pm 5/2$ $1h_{11/2}$:$\pm 1/2$, $\pm 3/2$, $\pm 5/2$, $\pm 7/2$	Filled Shells: N = 0, 1, 2, 3, 4 $1h_{11/2}$: Full Shell $2f_{7/2}$: Full Shell $1h_{9/2}$: $\pm 1/2$, $\pm 3/2$, $\pm 5/2$ $1i_{13/2}$:$\pm 1/2$, $\pm 3/2$, $\pm 5/2$, $\pm 7/2$, 9/2
^{181}Ta	≈ 0.3	Filled Shells: N = 0, 1, 2, 3 $1g_{9/2}$: Full Shell $1g_{7/2}$: $\pm 1/2$, $\pm 3/2$, $\pm 5/2$, 7/2 $2d_{5/2}$: $\pm 1/2$, $\pm 3/2$ $1h_{11/2}$:$\pm 1/2$, $\pm 3/2$, $\pm 5/2$, $\pm 7/2$ $2d_{3/2}$: $\pm 1/2$ $1h_{9/2}$: $\pm 1/2$	Filled Shells: N = 0, 1, 2, 3, 4 $1h_{11/2}$: Full Shell $2f_{7/2}$: Full Shell $1h_{9/2}$: $\pm 1/2$, $\pm 3/2$, $\pm 5/2$ $1i_{13/2}$:$\pm 1/2$, $\pm 3/2$, $\pm 5/2$, $\pm 7/2$ $1p_{3/2}$: $\pm 1/2$ $1g_{9/2}$: $\pm 1/2$

Nuclei	Deformation (δ)	Protons	Neutrons
^{201}Hg	≈ 0	Filled Shells: N = 0, 1, 2, 3 $1g_{9/2}$: Full Shell $1g_{7/2}$: Full Shell $2d_{5/2}$: Full Shell $1h_{11/2}$: Full Shell $2d_{3/2}$: Full Shell	Filled Shells: N = 0, 1, 2, 3, 4 $1h_{11/2}$: Full Shell $2f_{7/2}$: Full Shell $1h_{9/2}$: Full Shell $1i_{13/2}$: Full Shell $1p_{3/2}$: Full Shell $1f_{5/2}$: $\pm 1/2$, 3/2
^{229}Th	≈ 0.21	Filled Shells: N = 0, 1, 2, 3, 4 $1h_{11/2}$: Full Shell $1h_{9/2}$: $\pm 1/2$, $\pm 3/2$ $1i_{13/2}$: $\pm 1/2$, $\pm 3/2$	Filled Shells: N = 0, 1, 2, 3, 4, 5 $1i_{13/2}$: Full Shell $1g_{9/2}$: $\pm 1/2$, $\pm 3/2$, 5/2 $1i_{11/2}$: $\pm 1/2$, $\pm 3/2$ $1j_{15/2}$: $\pm 1/2$, $\pm 3/2$
^{151}Eu	≤ 0.05	Filled Shells: N = 0, 1, 2, 3 $1g_{9/2}$: Full Shell $1g_{7/2}$: Full Shell $2d_{5/2}$: $\pm 1/2$, $\pm 3/2$, 5/2	Filled Shells: N = 0, 1, 2, 3, 4 $1h_{11/2}$: Full Shell $2f_{7/2}$:$\pm 1/2$, $\pm 3/2$, $\pm 5/2$
^{153}Eu	> 0.25	Filled Shells: N = 0, 1, 2, 3 $1g_{9/2}$: Full Shell $1g_{7/2}$: $\pm 1/2$, $\pm 3/2$, 5/2 $2d_{5/2}$: $\pm 1/2$ $1h_{11/2}$:$\pm 1/2$, $\pm 3/2$, $\pm 5/2$	Filled Shells: N = 0, 1, 2, 3, 4 $1h_{11/2}$: Full Shell $2f_{7/2}$:$\pm 1/2$, $\pm 3/2$ $1h_{9/2}$: $\pm 1/2$ $1i_{13/2}$: $\pm 1/2$
^{167}Er	≈ 0.3	Filled Shells: N = 0, 1, 2, 3 $1g_{9/2}$: Full Shell $1g_{7/2}$: $\pm 1/2$, $\pm 3/2$, $\pm 5/2$ $2d_{5/2}$: $\pm 1/2$, $\pm 3/2$ $1h_{11/2}$:$\pm 1/2$, $\pm 3/2$, $\pm 5/2$, $\pm 7/2$	Filled Shells: N = 0, 1, 2, 3, 4 $1h_{11/2}$: Full Shell $2f_{7/2}$: $\pm 1/2$, $\pm 3/2$, $\pm 5/2$ $1h_{9/2}$: $\pm 1/2$, $\pm 3/2$ $1i_{13/2}$:$\pm 1/2$, $\pm 3/2$, $\pm 5/2$, 7/2
^{133}Cs ^{131}Xe	< 0 < 0		

List of Figures

List of Tables

Appendix One

Bibliography

[1] B. G. C. Lackenby, V. A. Dzuba, and V. V. Flambaum. *Phys. Rev. A* 98, 022518 (2018).

[2] B. G. C. Lackenby and V. V. Flambaum. *Journal of Physics G* 45, 075105 (2018).

[3] B. G. C. Lackenby, V. A. Dzuba, and V. V. Flambaum. *Phys. Rev. A* 98, 042512 (2018).

[4] B. G. C. Lackenby and V. V. Flambaum. *Phys. Rev. D* 98, 115019 (2018).

[5] B. G. C. Lackenby, V. A. Dzuba, and V. V. Flambaum. *Phys. Rev. A* 99, 042509 (2019).

[6] A. D. Sakharov. *JETP* 5, 24 (1967).

[7] M. Kobayashi and T. Maskawa. *Prog. Theo. Phys* 49, 2 (1973).

[8] G. R. Farrar and M. E. Shaposhnikov. *Phys. Rev. Lett.* 70, 2833 (1993).

[9] P. Huet and E. Sather. *Phys. Rev. D* 51, 379 (1995).

[10] M. Pospelov and A. Ritz. *Ann. Phys* 318, 119 (2005).

[11] L. Canetti, M. Drewes, and M. E. Shaposhnikov. *New J. Phys.* 14, 095012 (2012).

[12] V. V. Flambaum and E. Shuryak. *Phys. Rev. D* 82, 073019 (2010).

[13] S. J. B. J. J. B. R. B.-R. I. B. E. B. J. C. J. P. F. J. A. G. M. H. G. C. H. V. V. H. H. H. K. D. I. J. K. K. S. K. E. K. J. M. K. C. L. K. C. B. N. H. T. N. R. O. R. W. O. I. C. P. C. D. R. S. R. K. L. T. A. D. T. A. G. V. W. L. K. W. K. W. Y. Z. Ahmed, M. Amiri. Bicep3: a 95ghz refracting telescope for degree-scale cmb polarization (2014).

[14] P. Collaboration". *Astron. Astro.* 594 (2016).

[15] V. A. Kostelecký and R. Potting. *Phys. Rev. D* 51, 3923 (1995).

[16] P. Fayet. *Phys. Lett. B* 64, 159 (1976).

[17] P. Fayet. *Phys. Lett. B* 69, 489 (1977).

[18] M. Ramsey-Musolf and S. Su. *Phys. Rep.* 456, 1 (2008).

[19] S. Inoue, M. J. Ramsey-Musolf, and Y. Zhang. *Phys. Rev. D* 89, 115023 (2014).

[20] J. C. Pati and A. Salam. *Phys. Rev. D* 10, 275 (1974).

[21] T. D. Lee and C. N. Yang. *Phys. Rev.* 104, 254 (1956).

[22] C. S. Wu *et al. Phys. Rev.* 105, 1413 (1957).

[23] J. H. Christenson, J. W. Cronin, V. L. Fitch, and R. Turlay. *Phys. Rev. Lett* 13, 138 (1964).

[24] V. B. Berestetskii, E. M. Lifshitz, and L. P. Pitaevskii. *Quantum Mechanics (Non-Relativistic Theory)*, volume 4, (Pergamon Press Ltd.1982), 2 edition.

[25] I. B. Khriplovich and S. K. Lamoreaux. *CP Violation Without Strangeness*, (Berlin: Springer1997), 1 edition.

[26] M. Beyer and H. E. M. *CP Violation in Particle, Nuclear and Astrophysics*, (Springer, Berlin, Heidelberg2002), 1 edition.

[27] N. Cabibbo. *Phys. Rev. Lett.* 10, 531 (1963).

[28] K. Collaboration". *Phys. Rev. Lett.* 83, 22 (1999).

[29] N. Collaboration". *Phys. Lett. B* 465, 335 (1999).

[30] Abe, K. and et. al. Belle Collab. *Phys. Rev. Lett* 87, 091802 (2001).

[31] L. Collaboration. *Phys. Rev. Lett.* 110, 221601 (2013).

[32] B. Collaboration". *Phys. Rev. Lett.* 91, 201802 (2003).

[33] E. M. Purcell and N. F. Ramsey. *Phys. Rev.* 78, 807 (1950).

[34] L. Landau. *Nuclear Physics* 3, 127 (1957).

[35] J. H. Smith, E. M. Purcell, and N. F. Ramsey. *Phys. Rev.* 108, 120 (1957).

[36] G. Amelino-Camelia *et al. Nature* 393, 763 (1998).

[37] S. Coleman and S. L. Glashow. *Phys. Lett. B* 405, 249 (1997).

[38] S. Coleman and S. L. Glashow. *Phys. Rev. D* 59, 116008 (1999).

[39] A. Michelson and W. Morley. *American Journal of Science* 34, 203 (1887).

[40] R. J. Kennedy and E. M. Thorndike. *Phys. Rev.* 42, 400 (1932).

[41] H. E. Ives and G. R. Stilwell. *Opt. Soc. Am.* 28, 215 (1938).

[42] H. P. Robertson. *Rev. Mod. Phys.* 21, 378 (21).

[43] R. Mansouri and R. U. Sexl Gen. Rel. Grav., 8, 497 (1977), Gen. Rel. Grav., 8, 515 (1977), Gen. Rel. Grav., 8, 809 (1977).

[44] V. A. Kostelecký and S. Samuel. *Phys. Rev D* 39, 683 (1989).

[45] T. Damour arXiv:gr-qc/9711060 (1997).

[46] R. Gambini and J. Pullin. *Phys. Rev. D* 59, 124021 (1999).

[47] M. Pospelov and Y. Shang. *Phys. Rev. D* 85, 105001 (2012).

[48] N. E. Mavromatos. *Proceedings of Science* (2007).

[49] S. Liberati (2013).

[50] D. Colladay and V. A. Kostelecký. *Phys. Rev. D* 55, 6760 (1997).

[51] D. Colladay and V. A. Kostelecký. *Phys. Rev. D* 58, 116002 (1998).

[52] V. A. Kostelecký and C. D. Lane. *Phys. Rev. D* 60, 116010 (1999).

[53] V. A. Kostelecký and N. Russell (2017).

[54] H. Müller. *Phys. Rev. D* 71, 045004 (2005).

[55] H. Müller *et al. Phys. Rev. Lett.* 91, 020401 (2003).

[56] P. Wolf *et al. Phys. Rev. D* 70, 051902 (2004).

[57] C. Lane. *Phys. Rev. D* 72, 016005 (2005).

[58] G. Saathoff *et al. Phys. Rev. Lett.* 91, 190403 (2003).

[59] J. D. Prestage, J. J. Bollinger, W. M. Itano, and D. J. Wineland. *Phys. Rev. Lett.* 54, 22 (1985).

[60] T. E. Chupp *et al. Phys. Rev. Lett.* 63, 1541 (1989).

[61] M. A. Hohensee *et al. Phys. Rev. Lett.* 111, 050401 (2013).

[62] V. A. Dzuba. *Phys. Rev. A* 93, 032519 (2016).

[63] V. W. Hughes, H. G. Robinson, and V. Beltran-Lopez. *Phys. Rev. Lett.* 4, 342 (1960).

[64] R. W. P. Drever. *Philo. Mag.* 6, 683 (1961).

[65] S. K. Lamoreaux *et al. Phys. Rev. Lett.* 57, 3125 (1986).

[66] S. K. Lamoreaux *et al. Phys. Rev. A* 39, 1082 (1989).

[67] J. S. M. Ginges and V. V. Flambaum. *Phys. Rep.* 397, 63 (2004).

[68] I. B. Khriplovich. *Parity NonConservation In Atomic Phenomena*, (Gordon and Breach Science Publishers1981), 1 edition.

[69] O. P. Sushkov, V. V. Flambaum, and I. B. Khriplovich. *JETP* 60, 873 (1984).

[70] B. M. Roberts, V. A. Dzuba, and V. V. Flambaum. *Ann. Rev. Nucl. Part. Sci.* 65, 63 (2015).

[71] C.-P. Liu *et al. Phys. Lett. B* 713, 447 (2012).

[72] L. I. Schiff. *Phys. Rev.* 132, 2195 (1963).

[73] V. V. Flambaum, D. W. Murray, and S. R. Orton. *Phys. Rev. C* 56, 2820 (1997).

[74] V. V. Flambaum. *Phys. Lett. B* 320, 211 (1994).

[75] V. V. Flambaum, I. B. Khriplovich, and O. P. Sushkov. *Nucl. Phys. A* 449, 750 (1986).

[76] V. V. Flambaum and A. Kozlov. *Phys. Rev. C* 85, 068502 (2012).

[77] V. V. Flambaum, D. DeMille, and M. G. Kozlov. *Phys. Rev. Lett.* 113, 103003 (2014).

[78] J. J. Hudson *et al. Nature* 473, 493 (2011).

[79] N. S. Mosygain, M. G. Kozlov, and A. V. Titov. *J. Phys. B* 31, L763 (1998).

[80] H. M. Quiney, H. Skaane, and I. P. Grant. *J. Phys. B* 31, L85 (1998).

[81] F. A. Parpia. *J. Phys. B* 31, 1409 (1998).

[82] M. G. Kozlov and V. F. Ezhov. *Phys. Rev. A* 49, 4502 (1994).

[83] M. K. Nayak and R. K. Chaudhuri. *Pramana J. Phys.* 73, 581 (2009).

[84] T. C. Steimle, T. Ma, and C. Linton. *J. Chem. Phys.* 127, 234316 (2007).

[85] M. Abe *et al. Phys. Rev. A* 90, 022501 (2014).

[86] K. C. Cossel *et al. Chem. Phys. Lett.* 546, 1 (2012).

[87] H. Loh *et al. Science* 342 (2013).

[88] A. N. Petrov, N. S. Mosyagin, T. A. Isaev, and A. V. Titov. *Phys. Rev. A* 76, 030501(R) (2007).

[89] T. Fleig and M. K. Nayak. *Phys. Rev. A* 88, 032514 (2013).

[90] E. R. Meyer, J. L. Bohn, and M. P. Deskevich. *Phys. Rev. A* 73, 062108 (2006).

[91] L. V. Skripnikov, N. S. Mosyagin, A. N. Petrov, and A. V. Titov. *JETP Lett.* 88, 578 (2008).

[92] A. Le, T. C. Steimle, L. Skripnikov, and A. V. Titov. *J Chem. Phys.* 138, 124313 (2013).

[93] L. V. Skripnikov. *J. Chem. Phys.* 147, 021101 (2017).

[94] B. D. Cairncross, D. N. Gresh, M. Grau, and K. C. Cossel (2017).

[95] A. N. Petrov *et al. Phys. Rev. A* 89, 062505 (2014).

[96] E. R. Meyer and J. L. Bohn. *Phys. Rev. A* 78, 010502(R) (2008).

[97] L. V. Skripnikov, A. N. Petrov, and A. V. Titov. *J. Chem. Phys.* 139, 221103 (2013).

[98] L. V. Skripnikov, A. N. Petrov, A. V. Titov, and V. V. Flambaum. *Phys. Rev. Lett.* 113, 263006 (2014).

[99] L. V. Skripnikov and A. V. Titov. *J. Chem. Phys.* 142, 024301 (2015).

[100] T. Fleig and M. K. Nayak. *J. Mol. Sprectrosc.* 300, 16 (2014).

[101] M. Denis and T. Fleig. *J. Chem. Phys.* 145, 214307 (2016).

[102] J. Baron *et al. New J. Phys.* 19, 073029 (2017).

[103] L. V. Skripnikov and A. V. Titov. *Phys. Rev. A* 91, 042504 (2015).

[104] M. Denis *et al. New J. Phys.* 17, 043005 (2015).

[105] L. V. Skripnikov *et al. Phys. Rev. A* 92, 012521 (2015).

[106] T. Fleig, M. K. Nayak, and M. G. Kozlov. *Phys. Rev. A* 93, 012505 (2016).

[107] T. Fleig. *Phys. Rev. A* 95, 022504 (2017).

[108] J. S. M. Ginges and V. V. Flambaum. *Physics Reports* 397, 63 (2004).

[109] B. M. Roberts, V. A. Dzuba, and V. V. Flambaum. *Annual Review of Nuclear and Particle Science* 65, 63 (2015).

[110] O. P. Sushkov and V. V. Flambaum. *Soviet Physics JETP* 48, 608 (1978).

[111] I. B. Khriplovich and M. E. Pospelov. *Z. Phys. D* 22, 367 (1991).

[112] V. V. Flambaum. *Phys. Rev. Lett.* 117, 072501 (2016).

[113] D. Antypas *et al.* (2017).

[114] N. Leefer, L. Bougas, D. Antypas, and D. Budker (2014).

[115] T. Schmidt and H. Schuler. *Z. Physik* 94, 457 (1935).

[116] H. Schuler and T. Schmidt. *Z. Physik* 95, 265 (1935).

[117] H. B. G. Casimir. *Physica A* 2, 719 (1935).

[118] H. B. G. Casimir. *On the interaction between atomic nuclei and electrons*, (Springer Netherlands1936), 1 edition. ISBN 978-94-017-6067-6.

[119] A. Bohr and B. Mottelson. *Nuclear Structure, Volume I: Single-Particle Motion* (1998).

[120] N. J. Stone. *Atomic Data and Nuclear Data Tables* 90, 75 (2005).

[121] M. G. Mayer. *Phys. Rev.* 75, 1969 (1949).

[122] O. Haxel, J. H. D. Jensen, and H. E. Suess. *Phys. Rev.* 75, 1766 (1959).

[123] J. Rainwater. *Phys. Rev.* 79, 432 (1950).

[124] S. Nilsson. *Math.-Fys. Medd. Kgl. Danske Vid. Selsk.* 29 (1955).

[125] C. Gustafson, I. L. Lamm, B. Nilsson, and S. G. Nilsson. *Arkiv Fysik* 36, 613 (1967).

[126] A. Bohr and B. R. Mottelson. *Nuclear Structure: Volume II*, (W.A. Benjamin Inc.1975). ISBN 0-8053-1016-9.

[127] B. A. Brown *et al.* (2016).

[128] B. R. Mottelson and S. G. Nilsson. *Phys. Rev.* 99, 1615 (1955).

[129] B. A. Brown. *Phys. Rev. Lett.* 85, 5296 (2000).

[130] R. J. Furnstahl. *Nuclear Physics A* 706, 85 (2002).

[131] S. Typel and B. A. Brown. *Phys. Rev. C* 64, 027302 (2001).

[132] P.-G. Reinhard and W. Nazarewicz. *Phys. Rev. C* 81, 051303 (2010).

[133] B. C. Clark, L. J. Kerr, and S. Hama. *Phys. Rev. C - Nuclear Physics* 67, 13 (2003).

[134] A. Trzcińska *et al. Phys. Rev. Lett.* 87, 82501 (2001).

[135] H. Lenske. *Hyperfine Interactions* 194, 277 (2009).

[136] S. Abrahamyan, Z. Ahmed, and H. e. a. Albataineh. *Phys. Rev. Lett.* 108, 1 (2012).

[137] M. Smiciklas *et al. Phys. Rev. Lett.* 107, 171604 (2011).

[138] P. Wolf, F. Chapelet, S. Bize, and A. Clairon. *Phys. Rev. Lett.* 96, 060801 (2006).

[139] V. V. Flambaum and M. V. Romalis. *Phys. Rev. Lett.* 118, 142501 (2017).

[140] V. V. Flambaum, V. A. Dzuba, and C. Harabati. *Phys. Rev. A* 96, 012516 (2017).

[141] I. B. Khriplovich. *JETP* 44, 25 (1976).

[142] B. G. C. Lackenby and V. V. Flambaum. *J. Phys. G: Nucl. Part. Phys.* 45, 075105 (2018).

[143] N. Yoshinaga, K. Higashiyama, and R. Arai. *Prog. Theor. Phys.* 124, 1115 (2010).

[144] N. Yoshinaga, K. Higashiyama, R. Arai, and E. Teruya. *Phys. Rev. C* 89, 045501 (2014).

[145] N. Yamanaka *et al. Eur. Phys. J. A* 53, 54 (2017).

[146] V. F. Dmitriev, I. B. Khriplovich, and V. B. Telitsin. *Phys. Rev. C* 50, 2358 (1994).

[147] V. V. Flambaum and O. K. Vorov. *Phys. Rev. C* 51, 1521 (1995).

[148] R. J. Crewther, P. Di Vecchia, G. Veneziano, and E. Witten. *Phys. Lett. B* 88, 123 (1979).

[149] M. Pospelov and A. Ritz. *Phys. Rev. Lett.* 83, 2526 (1999).

[150] C. Alexandrou *et al. Phys. Rev. D* 95, 114514 (2017).

[151] JLQCD Collab. *Phys. Rev. D* 98, 054516 (2018).

[152] PNDME Collab. ArXiv:1808.07597 [hep-lat] (2018).

[153] R. D. Peccei and H. R. Quinn. *Phys. Rev. Lett.* 38, 1440 (1977).

[154] J. de Vries, E. Mereghetti, and A. Walker-Loud. *Phys. Rev. C* 92, 045201 (2015).

[155] J. Engel, M. J. Ramsey-Musolf, and U. van Kolck. *Prog. Part. Nucl. Phys.* 71, 21 (2013).

[156] T. Chupp, P. Fierlinger, M. Ramsey-Musolf, and J. Singh. ArXiv:1710.02504 [hep-ph] (2018).

[157] K. Fuyuto, J. Hisano, and N. Nagata. *Phys. Rev. D* 87, 054018 (2013).

[158] C. Y. Seng. ArXiv:1809.00307 [hep-ph] (2018).

[159] M. G. Kozlov and L. N. Labzovskii. *J. Phys. B* 28, 1933 (1995).

[160] M. S. Safronova *et al. Rev. Mod. Phys.* 90, 025008 (2018).

[161] L. V. Skripnikov, A. V. Titov, and V. V. Flambaum. *Phys. Rev. A* 95, 022512 (2017).

[162] M. D. Swallows *et al. Phys. Rev. A* 87, 012102 (2013).

[163] ACME Collab. *Science* 343, 269 (2014).

[164] ACME Collab. *Nature* 562, 355 (2018).

[165] C.-Y. Seng. *Phys. Rev. C* 91, 025502 (2015).

[166] N. Yamanaka and E. Hiyama. *JHEP* 2016, 67 (2016).

[167] V. A. Dzuba, J. C. Berengut, C. Harabati, and V. V. Flambaum. *Phys. Rev. A* 95, 012503 (2017).

[168] Y. Oganessian. *Eur. Phys. J. A* 42, 361 (2009).

[169] J. H. Hamilton, S. Hofmann, and Y. T. Oganessian. *Annu. Rev. Nucl. Part. Sci.* 63, 383 (2013).

[170] Y. T. Oganessian *et al. Nucl. Phys. A* 734, 109 (2004).

[171] M. Leino. *EPJ Web Conf.* 131, 01002 (2016).

[172] Y. Oganessian. *Acta Physica Polonica B* 43, 167 (2012).

[173] M. Laatiaoui *et al. Nature* 538, 495 (2016).

[174] T. K. Sato *et al. Nature* 520, 209 (2015).

[175] M. Laatiaoui *et al. Hyperfine Interactions* 227, 69 (2014).

[176] M. Laatiaoui. *EPJ Web of Conferences* 131, 05002 (2016).

[177] R. Ferrer *et al. Nature Comms.* 8 (2017).

[178] I. Lindgren and J. Morrison. *Atomic Many-Body Theory*, (Springer-Verlag Berlin Heidelberg1986), 2 edition.

[179] S. A. Blundell, W. R. Johnson, and J. Sapirstein. *Phys. Rev. A* 43, 3407 (1991).

[180] V. A. Dzuba, V. V. Flambaum, and M. G. Kozlov. *Phys. Lett. A* 54, 5 (1996).

[181] V. A. Dzuba, V. V. Flambaum, and O. P. Sushkov. *Phys. Lett. A* 140, 493 (1989).

[182] I. P. Grant and H. M. Quiney 23, 37 (1988).

[183] Y. Liu, R. Hutton, and Y. Zou. *Phys. Rev. A* 76, 062503 (2007).

[184] J. P. Desclaux and B. Fricke. *J. Physique* 41, 943 (1980).

[185] E. Eliav, U. Kaldor, and Y. Ishikawa. *Phys. Rev. Lett.* 74, 1079 (1995).

[186] S. Fritzsche, C. Z. Dong, F. Koike, and A. Uvarov. *Eur. Phys. J. D European Physical Journal D* 45, 107 (2007).

[187] Y. Zou and C. Froese Fischer. *Phys. Rev. Lett.* 88 (2002).

[188] A. Borschevsky *et al. Eur. Phys. J. D* 45, 042514 (2007).

[189] W. C. Martin and J. Sugar. *Phys. Rev. A* 53, 3 (1996).

[190] N. S. Mosyagin, I. I. Tupitsyn, and A. V. Titov. *Radiochemistry* 52, 394 (2010).

[191] V. A. Dzuba, M. S. Safronova, and U. I. Safronova. *Phys. Rev. A* 90, 012504 (2014).

[192] E. Eliav, S. Fritzsche, and U. Kaldor. *Nucl. Phys. A* 944, 518 (2015).

[193] A. Borschevsky *et al. Phys. Rev. A* 75, 042514 (2007).

[194] V. A. Dzuba and V. V. Flambaum. *Hyperfine Interactions* 237, 160 (2016).

[195] V. Pershina, A. Borschevsky, E. Eliav, and U. Kaldor. *J. of Chem. Phys.* 128, 024707 (2008).

[196] C. S. Nash. *J. Phys. Chem. A* 109, 3493 (2005).

[197] A. Landau, E. Eliav, Y. Ishikawa, and U. Kaldor. *J. of Chem. Phys.* 114, 2977 (2001).

[198] A. Borschevsky *et al. Phys. Rev. A* 91, 020501 (2015).

[199] C. Thierfelder *et al. Phys. Rev. A* 78, 052506 (2008).

[200] V. Pershina, A. Borschevsky, E. Eliav, and U. Kaldor. *J. Phys. Chem. A* 112, 13712 (2008).

[201] T. H. Dinh and V. A. Dzuba. *Phys. Rev. A* 94, 052501 (2016).

[202] P. Indelicato, J. P. Santos, S. Boucard, and J. P. Desclaux. *Euro. Phys. J. D* 45, 155 (2007).

[203] T. H. Dinh, V. A. Dzuba, and V. V. Flambaum. *Phys. Rev. A* 78, 062502 (2008).

[204] E. Eliav *et al. Phys. Rev. A* 53, 3926 (1996).

[205] Y. J. Yu, C. Z. Dong, J. G. Li, and B. Fricke. *Journal of Chemical Physics* 128, 124316 (2008).

[206] A. Landau, E. Eliav, Y. Ishikawa, and U. Kaldor. *J. Chem. Phys.* 115, 2389 (2001).

[207] I. S. Lim, P. Schwerdtfeger, B. Metz, and H. Stoll. *J. Chem. Phys.* 122, 104103 (2005).

[208] T. H. Dinh, V. A. Dzuba, V. V. Flambaum, and J. S. M. Ginges. *Phys. Rev. A* 78, 022507 (2008).

[209] G. Gaigalas *et al. Phys. Rev. A* 81, 022508 (2010).

[210] A. Borschevsky, V. Pershina, E. Eliav, and U. Kaldor. *Phys. Rev. A* 87, 022502 (2013).

[211] L. V. Skripnikov, N. S. Mosyagin, and A. V. Titov. *Chem. Phys. Lett.* 555 (2013).

[212] V. A. Dzuba. *Phys. Rev. A* 88, 042516 (2013).

[213] J. S. M. Ginges and V. A. Dzuba. *Phys. Rev. A* 91, 1 (2015).

[214] P. Schwerdtfeger, L. F. Pašteka, A. Punnett, and P. O. Bowman. *Nucl. Phys. A* 944, 551 (2015).

[215] P. J. Karol *et al. Pure App. Chem* 88, 155 (2016).

[216] P. Chhetri *et al. Phys. Rev. Lett* 120, 263003 (2018).

[217] V. Pershina. *Nucl. Phys. A* 944, 578 (2015).

[218] E. Eliav *et al. Phys. Rev. A* 53, 3926 (1996).

[219] V. Pershina, A. Borschevsky, E. Eliav, and U. Kaldor. *J. Phys. Chem. A* 112, 13712 (2008).

[220] Y. J. Yu, C. Z. Dong, J. G. Li, and B. Fricke. *J. Chem. Phys.* 128, 124316 (2008).

[221] A. V. Zaitsevskii, C. van Wüllen, and A. V. Titov. *Russ. Chem. Rev.* 78, 1173 (2009).

[222] C. Thierfelder *et al. Phys. Rev. A* 78, 052506 (2008).

[223] A. Landau, E. Eliav, Y. Ishikawa, and U. Kaldor. *J. Chem. Phys.* 114, 2977 (2001).

[224] A. Borschevsky *et al. Phys. Rev. A* 91, 020501(R) (2015).

[225] V. A. Dzuba and V. V. Flambaum. *Hyperfine Interactions* 237, 160 (2016).

[226] T. H. Dinh and V. A. Dzuba. *Phys. Rev. A* 94, 052501 (2016).

[227] C. Froese Fischer *et al. J. Phys. B* 49, 182004 (2016).

[228] A. Borschevsky *et al. Phys. Rev. A* 91, 020501(R) (2015).

[229] V. A. Dzuba, V. V. Flambaum, and M. G. Kozlov. *Phys. Rev. A* 99, 032501 (2019).

[230] B. G. C. Lackenby, V. A. Dzuba, and V. V. Flambaum. *Phys. Rev. A* 98, 042512 (2018).

[231] A. J. Geddes, D. A. Czapski, E. V. Kahl, and J. C. Berengut. *Phys. Rev. A* 98, 042508 (2018).

[232] V. A. Dzuba, M. S. Safronova, and U. I. Safronova. *Phys. Rev. A* 90, 012504 (2014).

[233] V. A. Dzuba, M. S. Safronova, U. I. Safronova, and A. Kramida. *Phys. Rev. A* 94, 042503 (2016).

[234] A. Türler and V. Pershina. *Chem. Rev.* 113, 1237 (2013).

[235] E. Johnson, V. Pershina, and B. Fricke. *J. Phys. Chem. A* 103, 8458 (1999).

[236] E. Johnson *et al. J. Chem. Phys* 116, 1862 (2002).

[237] V. A. Dzuba, V. V. Flambaum, and S. Schiller. *Phys. Rev. A* 98, 022501 (2018).

[238] H. P. Kelly. *Phys. Rev* 136, 3B (1964).

[239] V. A. Dzuba. *Phys. Rev. A* 71, 032512 (2005).

[240] W. R. Johnson, S. A. Blundell, and J. Sapirstein. *Phys. Rev. A* 37, 307 (1988).

[241] G. Breit. *Phys. Rev.* 34, 4 (1929).

[242] J. B. Mann and W. R. Johnson. *Phys. Rev. A* 4, 1 (1971).

[243] V. V. Flambaum and J. S. M. Ginges. *Phys. Rev. A* 72, 052115 (2005).

[244] V. A. Dzuba, V. V. Flambaum, P. G. Silverstrov, and O. P. Sushkov. *Phys. Lett. A* 131, 461 (1988).

[245] V. A. Dzuba, V. V. Flambaum, P. G. Silvestrov, and O. P. Sushkov. *J Phys. B* 20, 1399 (1987).

[246] E. M. Lifshitz and L. P. Pitaevskii. *Statistical Physics Part 2*, (Pergamon Press1980), 3 edition.

[247] A. Kramida, Yu. Ralchenko, J. Reader, and and NIST ASD Team. NIST Atomic Spectra Database (ver. 5.5.6), [Online]. Available: `https://physics.nist.gov/asd` [2018, September 25]. National Institute of Standards and Technology, Gaithersburg, MD. (2018).

[248] V. A. Dzuba and V. V. Flambaum. *Phys. Rev. A* 77, 012514 (2008).

[249] B. M. Schädel. *Chemistry of superheavy elements*, volume 604 (2012).

[250] *Phys. Rev. C* 72, 034611 (2005).

[251] B. Fricke. *Recent impact of physics on inorganic chemistry* 21 (1975).

[252] A. J. Geddes, D. A. Czapski, E. V. Kahl, and J. C. Berengut. *Phys. Rev. A* 2018, 042508 (98).

[253] A. Borschevsky. (Private Communication).

[254] V. A. Dzuba, V. V. Flambaum, and J. K. Webb. *Phys. Rev. A* 95, 062515 (2017).

[255] I. Angeli and K. P. Marinova. *Atom. Data Nucl. Data Tabl.* 99, 69 (2013).

[256] V. A. Dzuba, V. V. Flambaum, P. G. Silvestrov, and O. P. Sushkov. *Phys. Lett. A* 118, 177 (1986).

[257] V. A. Dzuba, V. V. Flambaum, P. G. Silvestrov, and O. P. Sushkov. *J. Phys. B* 20, 3297 (1987).

[258] M. Ortiz and R. Mayo-García. *J. Phys. B* 45, 055701 (2012).

[259] R. Kling and M. Kock. *J. Qaunt. Spec. Rad. Trans.* 62, 129 (1999).

[260] S. Ivarsson *et al. Astron. Astrophys.* 409, 1141 (2003).

[261] M. Kwiatkowski, P. Zimmermann, E. Biémont, and N. Grevesse. *Astron. Astrophys.* 135, 59 (1984).

[262] J. R. Fuhr and W. L. Wiese. *NIST Atomic Transition Probability Tables*, (CRC Press, Inc. Boca Raton, FL1996), 77 edition.

[263] N. G. Polukhina. *Phys.-Usp.* 55, 614 (2012).

[264] V. F. Gopka *et al. Kinematics Phys. Celestial Bodies* 24, 89 (2008).

[265] V. Fivet *et al. Mom. Not. R. Astron. Soc.* 380, 781 (2007).

[266] S. Goriely, A. Bauswein, and H.-T. Janka. *Astrophys. J. Lett.* 738, L32 (2017).

[267] G. M. Fuller, A. Kusenko, and V. Takhistov. *Phys. Rev. Lett.* 119, 061101 (2017).

[268] A. Frebel and T. C. Beers. *Phys. Today* 71, 30 (2018).

[269] B. Schuetrumpf *et al. Phys. Rev. C* 91, 025801 (2015).

[270] D. N. Stacey. *Rep. Prog. Phys.* 29, 171 (1966).

[271] V. V. Flambaum, A. J. Geddes, and A. V. Viatkina. *Phys. Rev. A* 97, 032510 (2018).

[272] W. Nazarewicz. *Nat. Phys.* 14, 537 (2018).

[273] A. Ghoirso *et al. Phys. Rev. Lett.* 33, 25 (1974).

[274] G. Münzenberg *et al. Z. Phys* A300, 107 (1981).

[275] G. Münzenberg *et al. Z. Phys* A317, 235 (1984).

[276] G. Münzenberg *et al. Z. Phys* A309, 89 (1982).

[277] E. Johnson, V. Pershina, and B. Fricke. *J. Phys. Chem. A* 103, 8458 (1999).

[278] E. Johnson *et al. J. Chem. Phys.* 116, 1862 (2002).

[279] Y. T. Oganessian *et al. Phys. Rev. C* 74, 044602 (2006).

[280] V. Pershina. *Russ. Chem. Rev.* 78, 1153 (2009).

[281] O. Kullie and T. Saue. *Chem. Phys* 395, 54 (2012).

[282] A. Shee, S. Knecht, and T. Saue. *PPhys. Chem. Chem. Phys.* 17 (2015).

[283] C. S. Nash and B. E. Bursten. *Angew. Chem.* 38, 115 (1999).

[284] P. Schwerdtfeger. *EPJ Web Conf.* 131, 1 (2016).

[285] K. S. Pitzer. *J. Chem. Phys* 63, 1032 (1975).

[286] E. Eliav, U. Kaldor, Y. Ishikawa, and P. Pyykkö. *Phys. Rev. Lett.* 77, 5350 (1996).

[287] V. Pershina, A. Borschevsky, E. Eliav, and U. Kaldor. *J. Chem. Phys* 129 (2008).

[288] T. Hangele *et al. J. Chem. Phys.* 136, 214105 (2012).

[289] I. Goidenko *et al. Phys. Rev. A* 67, 020102 (2003).

[290] J. P. Desclaux. *Atom. Data Nucl. Data Tab* 12, 311 (1973).

[291] P. Jerabek, B. Schuetrumpf, P. Schwerdtfeger, and W. Nazarewicz. *Phys. Rev. Lett.* 120, 053001 (2018).

[292] P. Pyykkö. *Chem. Rev.* 88, 563 (1988).

[293] C. Thierfelder and P. Schwerdtfeger. *Phys. Rev. A* 82, 062503 (2010).

[294] D. C. Morton. *Astrophys. J. Suppl. Ser.* 130, 403 (2000).

[295] J. R. Fuhr and W. L. Wiese. *NIST Atomic Transition Probability Tables*, (CRC Press, Inc. Boca Raton, FL1996), 77 edition.